CENTRO BRASILEIRO DE PESQUISAS FÍSICAS

MASTER'S THESIS

Spin-Wave Propagation Within Magnetic Néel Walls

Author
Danilo FROES BATISTA

Supervisor:
Dr. João Paulo SINNECKER

Rio de Janeiro, Brazil
August 6, 2018

"If we knew what it was we were doing, it would not be called research, would it?"

Albert Einstein

Abstract

Magnonics is an emerging research field that aims to use spin-waves to transmit and process information, which can be encoded either in the amplitude or the phase, and they have the advantage of not relying in charge transport, which might eliminate Joule losses. Spin-wave propagation is usually performed in geometrically patterned magnetic waveguides that require the continuous application of an external magnetic field, jeopardizing the energy efficiency of the system.

Magnetic domain walls are known for either reflecting or phase shifting incident spin-waves. Recently, it has been proposed that they can be used as propagation channels. As they exist in remanent magnetic states, they don't require an external field, and as boundary regions, domain walls act as potential wells, thus confining the spin-waves within its nano-sized width. We have studied the use of magnetic Néel walls as spin-waves channels for information transport through micromagnetic simulations, and the experimental achievement of these structures through magnetometry and magnetic domain imaging techniques.

The micromagnetic simulations of spin-wave transmission along a 180^o Néel wall, has shown that strongly confined waves are found within the wall width up to 3 GHz, with well-defined wave vectors and above that frequency, the wave starts to spread to the uniform domains. The dispersion relation for the confined waves resembles a magnetostatic-dominated Damon-Eschbach mode with positive dispersion with group velocites up to 1.8 km/s and propagation length up to 4 μm. The Néel wall is naturally found in Landau-domain configurations in nanostructures, which also contains a vortex separating the wall in two. We have shown that the vortex act as a barrier for spin-waves, except for very specific frequencies, thus, acting as a frequency filter.

Experimentally, the Landau structure is very hard to achieve as small fields are enough to irreversibly saturate the structure, as we have shown through hysteresis simulations, SQUID and MOKE magnetometry experiments. To overcome that, we have fabricated a 10 μm wide rectangular permalloy structure that gradually shrinks to a constant 5 μm end on the other side by electron-beam lithography and lift-off. An alternate exponentially decaying field is transversely applied to reproducibly obtain the Landau configuration, as confirmed by Kerr microscopy images.

As future steps, Lorentz microscopy, along with ferromagnetic resonance experiments will be performed in the samples, and also, the design of magnonic circuitry that includes the Néel wall as waveguide are to be conceptualized and experimentally achieved.

Resumo

Magnônica é uma área de pesquisa que busca utilizar ondas de spin para transmitir e processar informação, que pode ser codificada tanto na amplitude quanto na fase. Possuem a vantagem de não dependender de tansporte de carga, o que pode eliminar perdas por efeito Joule. A propagação de ondas de spin é geralmente feita em guias de onda litografadas que necessitam a aplicação de um campo magnético externo, o que prejudica a eficiência energética do sistema, além de limitar a flexibilidade do caminho de propagação das ondas.

Recentemente, foi proposto que paredes de domínio magnéticas podem ser usadas como guias de ondas de spin. Como existem em estados magnéticos remanentes, não requerem aplicação de campos externos, e como regiões de interface, agem como poços de potencial, confinando as ondas em sua largura nanométrica. Nesta dissertação, estudamos o uso de paredes de domínios de Néel como canais de propagação de ondas de spin através de simulações micromagnéticas, e a realização experimental dessas estruturas através de técnincas de magnetometria e imageamento de domínios magnéticos.

Simulações micromagnéticas da transmissão de ondas de spin em paredes de Néel, mostrou que as ondas são fortemente confinadas em frequências de até 3 GHz, com vetores de ondas bem definidos, e acima disso, as ondas perdem o caráter de confinamento. A relação de dispersão para as ondas confinadas são do tipo magnetostática, com dispersão positiva, velocidades de grupo de até 1.8 km/s e comprimentos de propagação de até 4 μm. A parede de Néel é naturalmente encontrada em nanoestruturas que possuem domínios de Landau, que também possuem um vórtice separando a parede em duas partes. Foi mostrado que o vórtice age impede a propagação das ondas de spin de um lado para o outro, exceto para frequências específicas, agindo assim como um filtro de frequência.

Experimentalmente, a estrutura de Landau é não é facilmente obtida, pois pequenos campos externos são suficiente para saturar irreversivelmente a estrutura, como mostramos através de simulações de histerese, e experimentos de magnetometria SQUID e MOKE. Estruturas retangulares de permalloy ou de CoFeB com uma largura de 10 μm de uma lado, que gradualmente diminui até uma largura de 5 μm do outro lado, foram fabricadas por litografia de feixe de elétrons e lift-off. A estrutura de Landau só é obtida reprodutivelmente através da aplicação de um campo desmagnetizante transversal, o que foi confirmado por imagens Kerr.

Como próximos passos, microscopia Lorentz e experimentos de ressonância ferromagnética serão realizados nas amostras, e também o desenho de circuitos magnônicos que incluam as paredes de Néel como guias de ondas devem ser idealizadas e obtidas experimentalmente.

Agradecimentos

Agradeço primeiramente ao meu orientador João Paulo Sinnecker, pelo apoio e suporte, pelas conversas, discussões científicas e todo o tempo gasto nos laboratórios. Não tenho dúvidas do quanto isso teve impacto na minha vida acadêmica e pessoal. Agradeço também à professora Elis Sinnecker, por ter me apresentado ao mundo do nanomagnetismo e à estrutura do CBPF, além das medidas de MFM. Ao professor Sampaio, pelo suporte e pelas medidas, que não teriam acontecido sem sua ajuda. Ao professor Antônio Domingues dos Santos, pelas imagens Kerr. Ao CNPQ e CAPES pela bolsa e pelos projetos de pesquisa.

Ao CBPF como um todo — professores, funcionários e infraestrutura —, por ter me recebido tão bem e viabilizado a produção desta tese. Ao LabNano e LabSurf, pelos equipamentos e materiais, sala limpa, e-line, sputtering, e tudo o mais de que eu precisei. Aos funcionários da limpeza, segurança, oficina mecânica. Ao Ricardo e à Bete, pelo carinho e pela eficiência.

A todos os colegas do CBPF, que tanto me ajudaram a conhecer e entender o mundo da física, e aos que me deram todos os treinamentos, em especial Lesslie, Roberta e Grécia, por toda a paciência. Às amizades que surgiram no CBPF e que levarei para a vida, em especial Pablo, Jade, Dani e mais um monte de gente.

Àquele que aturou todos os altos e baixos destes dois anos e me deu todo o suporte para que eu chegasse até o final, sempre com aquela calma e fome: obrigado, Pedro Belchior. Aos meus gordinhos, que em todos os churrascos viravam os olhos quando eu começava a falar de física: Guilherme, Júlia, Evelin, Fernanda, Jenifer, amo vocês. Às Thaises da minha vida: Oliveira e Rodrigues. Aos meus amigos do coração Ana Paula, Ju Frouche e Victor Aksenow. Tem mais um milhão de nomes que deveriam estar aqui, obrigado por tudo!

Finalmente, àqueles que permitiram que tudo isso acontecesse, que tanto investiram e apostaram em mim. Espero sempre fazer meu melhor para lhes retruibuir por tudo: meus pais, Celso e Maria José, e meu irmão, Matheus.

Contents

Abstract ii

Resumo iii

Acknowledgements iv

1 Introduction 1
- 1.1 Motivation . . . 1
- 1.2 Objectives . . . 2
- 1.3 This Thesis . . . 3

2 Theoretical Background 4
- 2.1 Magnetic Materials . . . 4
- 2.2 Ferromagnetism . . . 8
  - 2.2.1 Exchange Energy . . . 9
  - 2.2.2 Zeeman Energy . . . 9
  - 2.2.3 Magnetostatic Energy . . . 10
  - 2.2.4 Anisotropy Energy . . . 10
- 2.3 Magnetic Domains and Domain Walls . . . 11
- 2.4 Micromagnetic Equations . . . 14
  - 2.4.1 Energy Minimization . . . 14
  - 2.4.2 Magnetization Dynamics . . . 15
- 2.5 Magnetic Configurations in Permalloy Rectangles . . . 15
- 2.6 Spin Waves . . . 18
  - 2.6.1 Spin Waves in Thin Films . . . 20

3 Methods 23
- 3.1 Micromagnetic Simulations . . . 23
  - 3.1.1 Static Magnetization Methods . . . 25
    - 3.1.1.1 Magnetic Ground-State . . . 25
    - 3.1.1.2 Hysteresis Curves . . . 25
  - 3.1.2 Magnetization Dynamics Methods . . . 25
    - 3.1.2.1 Magnetic Eigenmodes . . . 25
    - 3.1.2.2 Dispersion Relation . . . 26
- 3.2 Fabrication of Samples . . . 26
  - 3.2.1 Optical Lithography: Positive Resist . . . 27

3.2.2 Electron-Beam Lithography: Positive Resist . . . 29
3.2.3 Magnetron Sputtering . . . 30
3.2.3.1 X-ray Reflectivity . . . 32
3.3 SQUID Magnetometry . . . 33
3.4 Magneto-Optic Kerr Effect (MOKE) . . . 33
3.4.1 MOKE Magnetometry . . . 34
3.4.2 Kerr Microscopy . . . 36
3.5 Magnetic Force Microscopy . . . 37

4 Results and Discussion **39**
4.1 Micromagnetic Simulations: Spin-Waves in Néel Walls . . . 39
4.2 Micromagnetic Simulations: Spin-Waves in Landau Domain States . . . 48
4.3 Micromagnetic Simulations: Magnetic Ground-State in Permalloy Rectangles . . . 55
4.4 Fabricated Structures . . . 58
4.5 Hysteresis Loop . . . 60
4.5.1 Micromagnetic Simulations . . . 60
4.5.2 Experimental Results . . . 62
4.6 Magnetic Domains Imaging: MFM and Kerr Microscopy . . . 65

5 Conclusions and Future Work **69**

Bibliography **71**

List of Figures

2.1 Classification of magnetic materials: (A) paramagnetic, (B) ferromagnetic, (C) antiferromagnetic and (D) ferrimagnetic. 4
2.2 (A) Typical magnetization curve for a diamagnet (red), a paramagnet (green) and a ferri- or ferromagnet (blue). (B) A complete magnetization curve for a ferromagnet. 6
2.3 Magnetic behavior as a function of temperature for a (A) paramagnet and for a (B) ferromagnet. 7
2.4 The division in domains lowers the magnetostatic energy of the sample. 11
2.5 The two main types of domain wall. 13
2.6 NIST Standard problem 1. 16
2.7 Magnetic configurations in thin-film permalloy rectangles. Images obtained from a 2 μm x 1 μm x 5 nm permalloy rectangle simulation from the micromagnetic simulation software Mumax3[35]. 17
2.8 Pictorial representation of a spin wave. 18
2.9 Different geometries for spin waves propagating in a thin film. (A) Magnetostatic Forward Volume Modes (MSFVM). (B) Magnetostatic Backward Volume Modes (MSBVM). (C) Magnetostatic Surface Modes (MSSM). 20
2.10 Typical dispersion relation for the lowest-order magnetostatic mode for each geometry. 21

3.1 Sinc-Function 24
3.2 Additive lithography with positive-resist steps. 27
3.3 An example of an electron-beam lithography dose test with doses varying between 70 and 300 $\mu C/cm^2$. 29
3.4 Schematic representation of plasma formation in magnetron sputtering. The ionized argon atoms hit the surface of the target metal, ejecting atoms that are accelerated towards the sample, that coats it. 31
3.5 The AJA International magnetron sputtering used in this thesis, located at LABNANO/CBPF. Photo withdrawn from [48]. 31
3.6 The diffraction pattern in thin films (A) and the quadratic fitting (red line) for obtaining the film thickness (B). 32
3.7 MOKE geometries: (A) Polar, (B) Longitudinal and (C) Transversal. . . 34
3.8 Focused magneto-optic Kerr effect magnetometry in the longitudinal geometry principle of operation. 35

3.9 Focused magneto-optic Kerr effect magnetometry in the longitudinal geometry setup. Extracted from [48] . . . 36
3.10 Atomic Force Microscopy (AFM) scheme. The interaction between the tip and the sample topography causes deflections in the cantilever that are optically detected at a photodiode. This allows the sample surface to be mapped. . . . 37

4.1 Mumax3 Simulations: Néel wall with longitudinal periodic boundary conditions. . . . 40
4.2 Mumax3 Simulations: An out-of-plane sinc pulse was applied at the antenna and the time evolution of the z-component of the magnetization was saved and Fourier transformed. . . . 41
4.3 Mumax3 Simulations: The out-of-plane magnetization configuration due to a sinusoidal excitation at a 20 nm thick antenna at the center in several frequencies. The blue and red colors are for +z and -z magnetization, respectively. . . . 43
4.4 Mumax3 Simulations: The z-magnetization across the y-direction for a fixed x-position for 1 GHz, 4 GHz and 6 GHz sinusoidal excitations. 44
4.5 Mumax3 Simulations: Dispersion relation for the spin waves confined within a Néel wall in a 10 μm x 1 μm x 5 nm permalloy rectangle with longitudinal periodic boundary conditions, excited at a 20 nm dot at the wall center. . . . 44
4.6 Mumax3 Simulations: Group velocity (A) and propagation length (B) of the confined spin-waves as a function of frequency. . . . 45
4.7 Mumax3 Simulations: Néel wall displacement due to a transverse bias magnetic field. . . . 47
4.8 Mumax3 Simulations: Landau-domain in a 5 μm x 1 μm permalloy rectangle. . . . 48
4.9 Mumax3 Simulations. . . . 49
4.10 Spin waves excited at one side of the Néel wall only pass through the vortex in specific frequencies. . . . 50
4.11 Landau-domain with 2 mT field. . . . 51
4.12 FMR eigenmodes for an out-of plane excitation within a Néel wall. . . . 52
4.13 Out-of-plane magnetization in the Néel wall for a 2.4 GHz excitation. . 53
4.14 The dispersion relation of propagating spin-waves excited in a 20 nm dot within the Néel wall of a 5 μm x 1 μm x 5 nm permalloy rectangle. 54
4.15 Comparasion between the dispersion relation in an infinite Néel wall (with longitudinal periodic boundary conditions) and in a finite wall in a Landau state. . . . 54
4.16 Magnetic configurations before and after relaxation . . . 55

4.17 The total energy for a 1 μm x L μm x 5 nm permalloy rectangle as a function of L. Three regions can be identified: A and C, where the ground state is a uniform state, and B, where it is the Landau-state. . . 56
4.18 The total energy for a 2L μm x L μm x 5 nm permalloy rectangle as a function of L. The lower energy state is highlighted in each region. . . 57
4.19 The total energy for a 5L μm x L μm x 5 nm permalloy rectangle as a function of L. The lower energy state is always the uniform. 58
4.20 The nanostructures fabricated by electron-beam lithography in order to stabilize the Landau state: a rectangle with a 10 μm width that gradually narrows to a constant 5 μm width on one side. 59
4.21 Several possible magnetic configurations for the nanostructure. 60
4.22 Longitudinal hysteresis cycle simulated for a 5 μm x 1μm x 5 nm permalloy rectangle. After the first saturating field is achieved, the information about the initial state (uniform, Landau or diamond) is completely lost. 62
4.23 Transverse hysteresis cycle simulated for a 5 μm x 1μm x 5 nm permalloy rectangle. 63
4.24 The hysteresis loop of a matrix of the permalloy elements, measured by SQUID magnetometry. 64
4.25 The hysteresis loop of one single permalloy element, measured by Magneto-optic Kerr effect (MOKE) magnetometry. 64
4.26 Magnetic force microscopy of elements 66
4.27 Kerr image of one CoFeB element with an increasing longitudinal external magnetic field in the sequence (A) to (C). 67
4.28 Kerr image of CoFeB element under a transverse external field. 67
4.29 MOKE images after demagnetization. 68

List of Abbreviations

CMOS	**C**omplementary **M**etal-**O**xide **S**emiconductor
FFT	**F**ast **F**ourier **T**ransform
FMR	**F**erro**m**agnetic **R**esonance
VNA	**V**ector **N**etwork **A**nalyzer
MOKE	**M**agneto-**O**ptic **K**err **E**ffect
SQUID	**S**uperconducting **Q**uantum **I**nterference **D**evice
LLG	**L**andau-**L**ifshitz-**G**ilbert
GPU	**G**raphics **P**rocessing **U**nit
CUDA	**C**ompute **U**nified **D**evice **A**rchitecture
Py	**P**ermallo**y**

List of Symbols

$\vec{B}$	magnetic field	T
$\vec{M}$	magnetization	$\mathrm{A\,m^{-1}}$
$\vec{m}$	reduced magnetization	
A	exchange stiffness	$\mathrm{J\,m^{-1}}$
Ku_1	uniaxial anisotropy constant	$\mathrm{J/m^3}$
α	Gilbert damping parameter	
τ	torque	N m
γ	gyromagnetic ratio	$\mathrm{rad\,s^{-1}\,T^{-1}}$
c	speed of Light	$2.997\,924\,58 \times 10^{8}\,\mathrm{m\,s^{-1}}$
μ_0	magnetic Permeability in Vacuum	$4\pi \times 10^{-7}\,\mathrm{H\,m^{-1}}$
μ_B	Bohr magneton	$9.274\,009\,994 \times 10^{-24}\,\mathrm{J\,T^{-1}}$
h	Planck's constant	$6.626\,070\,04 \times 10^{-34}\,\mathrm{J\,s}$

Chapter 1

Introduction

1.1 Motivation

The semiconductor industry has rapidly grown from few companies in the 1960s, when the transistor manufacturing became viable, to a worldwide 400 billion US dollars sector in 2017 [1]. The technology revolution that accompanied that — the world of computers, high-speed internet and smartphones — has been made possible through the exponential miniaturization of microprocessors and increasing data processing speed. This is a consequence of the computing industry rule of thumb: the Moore's law, that states that the number of transistors in an integrated circuit will double every two years or so [2].

However, as the transistors scale to a few-nanometers size range, the CMOS technology reaches a physical constraint, the quantum mechanics limit, in which its intrinsic uncertainties would make them hopelessly unreliable for the currently employed Boolean logic. Nevertheless, the current major drawback in keeping Moore's law is the substantial power consumption due to the electric current inherent Joule heating [3]. Thus, to overcome that, several novel research fields have been proposing low-dissipation information carriers as substitutes for the electron, such as photons in photonics [4], the electron spin in spintronics [5] and spin-waves, and their quanta magnons, in magnonics [6].

Spin waves are perturbations of the microscopic magnetization vectors that propagate in a magnetic material. They were introduced by Bloch, in 1930, in order to explain the low-energy collective spin excitations that caused a $T^{3/2}$ temperature dependence of the spontaneous magnetization of a ferromagnet [7] at low temperatures. As no charge transport is needed for spin waves, their propagation can be free of Joule heat losses. Also, their spectrum covers the GHz range, which is currently used in communication, and can also reach the promissing THz range [8]. Their relatively low group velocities reduces their wavelength to the nanoscale, thus allowing the miniaturization of magnon-based devices [9].

Magnonics is the research field that aims to use spin-waves for information transport and processing, which can be encoded either in the wave amplitude or phase. Magnonic devices make use of the inherent wave characteristics [6], such as spin-wave excitation and propagation [10–12], interference and diffraction [13, 14], refraction and reflection [15], and quantization due to lateral confinement [16]. The recent advances in nanofabrication and in micromagnetic simulations have boosted the demonstration and realization of several magnonic devices, such as spin-wave diodes [17], multiplexers [18], logic gates [19–21] and waveguides [22, 23].

One main building block of a magnonic device is a waveguide to transmit the spin-wave from one physical location to a desired position. This is generally done through a geometrically patterned microstrips with a large external magnetic field to saturate their magnetization, in order to select specific spin-wave modes [24, 25]. Although significant progress has been made, as integration with spin-torque nanodevices [26] and propagation in curved geometries [22, 27, 28], the continuous application of a magnetic field still jeopardizes the energy efficiency of the system.

One way to overcome that is the use of dipolar coupled magnetic nanostructures with well-defined uniform remanent states due to shape anisotropy [29]. These allow different geometries without an external field, but once the system is fabricated, no flexibility in the pathway can be made any further. A fundamentally different approach that has been proposed would be the use of surfaces and boundaries, which naturally confine spin-waves within their width, as channels for the wave propagation [30, 31].

The use of magnetic domain walls as spin-wave channels was firstly addressed by a numerical study [30] for specific wall conditions. It has gained momentum after a work [32] has shown the experimental realization of spin-wave transmission in magnetic Néel walls. These walls are found in remanent Landau-domains states in permalloy nanostructures, so they do not need an external magnetic field. Also, the domain wall can be easily moved through the use of very small magnetic fields, and charge or spin currents. All of these show the potential of using magnetic domain walls as low-energy and flexible channels for spin-wave transmission in magnonic devices [21, 33, 34].

1.2 Objectives

This thesis aims to computationally and experimentally evaluate the use of Néel domain walls as spin-wave waveguides for information transmission and processing for magnonic applications.

Through micromagnetic simulations, we aim to analyze the nature of the spin-waves that can be excited within a magnetic Néel wall: its confinement within the

wall width, its dispersion characteristics and its flexibility under external magnetic fields conditions. Also, to find the ground-state magnetic configuration for permalloy rectangles and compute their behaviour under an external field.

Experimentally, we aim to fabricate, through lithographic techniques, permalloy or CoFeB nanostructures that can contain a magnetic Landau-domain configuration, and identify the conditions to reproducibly obtain the magnetic Néel wall, in order to perform static and dynamic magnetic characterization experiments.

1.3 This Thesis

This thesis is organized in the following manner: a theoretical background, the computational and experimental methods, the results and discussion, and conclusions and future work.

In chapter 2, the micromagnetic equations are explained: the magnetic free energy terms and the Landau-Lifshitz-Gilbert equation. The equations for magnetic domain and domain walls are derived, and the possible low-energy magnetic configurations for permalloy rectangles are discussed. Also, the solutions for spin-waves in the magnetostatic regime in thin films are obtained.

In chapter 3, the micromagnetic simulation software Mumax3 [35] is described along the static and dynamic simulations protocols. Also, the fabrication of samples through lithography processes is explained, along with the characterization methods of SQUID magnetometry, magneto-optic Kerr effect magnetometry and imaging and magnetic force microscopy.

Chapter 4 shows the results and discussion for micromagnetic simulations of spin-waves for an infinite Néel wall and for a finite Néel wall in a Landau-domain configuration. Also, the simulations of the lowest-energy magnetic state for permalloy rectangles and hysteresis loops of the main states. The experimentally fabricated structures are shown and the magnetometry experiments, along with the magnetic domain images are shown and explained.

Chapter 5 presents the current conclusions and future work.

Chapter 2

Theoretical Background

2.1 Magnetic Materials

The magnetic proprieties of a material arises from its electrons proprieties — for instance, the total angular momentum (J), with the orbital (L), and electronic and nuclear spin (S) angular momenta terms — and their interaction with each other and with external magnetic fields [36]. The atomic magnetic moment (μ) is evaluated through eq. 2.1, where g is the Landé g-factor, μ_B is the Bohr magneton and J is the total angular momentum quantum number ($J = L + S$) [37].

$$\mu = -g\mu_B J \tag{2.1}$$

Materials with no resulting atomic magnetic moment are called diamagnetic. Those that, even though there is a resulting magnetic moment, no order is present, are called paramagnetic (Fig. 2.1 (A)). If there are both an effective moment and a regular arrangement, then we have magnetic materials [37].

The latter can be classified according to the relative orientation between neighboring moments (Fig. 2.1): ferromagnetic (B) — with a parallel order of spins —, antiferromagnetic (C) — antiparallel order, with zero net magnetization — , ferrimagnetic (D) — antiparallel order with a net magnetization —.

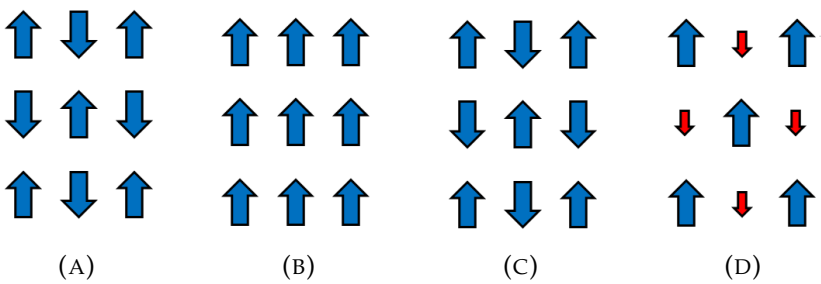

FIGURE 2.1: Classification of magnetic materials: (A) paramagnetic, (B) ferromagnetic, (C) antiferromagnetic and (D) ferrimagnetic.

The effective momentum of a material is described by the magnetization vector ($\vec{M}$, S.I. unit A m^{-1}), eq. 2.2, which is the sum of all atomic momenta ($\vec{\mu}$, eq. 2.1) divided by its volume (V). An external magnetic field ($\vec{H}$, S.I. unit A m^{-1}) may induce a magnetization in a material, the resulting field can be described by the magnetic induction — or magnetic flux density — vector field ($\vec{B}$, S.I. unit T), eq. 2.3.

$$\vec{M} = \lim_{V \to 0} \frac{\sum \vec{\mu}}{V} \tag{2.2}$$

$$\vec{B} = \mu_0(\vec{M} + \vec{H}) \tag{2.3}$$

We can, then, describe the magnetic behavior of a material by how its magnetization changes with the application of an external magnetic field [38] through a quantity called susceptibility (χ, dimensionless), eq. 2.4.

$$\chi = \frac{M}{H} \tag{2.4}$$

A magnetization curve is the graphical representation of the magnetization vs the external field, fig. 2.2(A). For dia-, para- or antiferromagnets, that have no net magnetization, the curve is linear — the former with a negative slope, and a positive slope for the other two —. For ferri- or ferromagnets, fig. 2.2(B) the curve is non-linear, and it reaches a constant value of M at large values of H, the saturation magnetization (M_S).

Also, even when the field is removed, the ferri- or ferromagnets still retain a finite value of magnetization, the remanence magnetizaton (M_R), this behavior is known as hysteresis. The magnetization only returns to zero when a strong enough field is applied in the opposite direction, this magntitude is called coercive field (H_C) [38].

A hard ferromagnet needs a high field in order to achieve the saturation, whereas a soft ferromagnet only needs a small field for that. The main material used in this work is permalloy (Py), here taken for $Ni_{80}Fe_{20}$, which is a soft magnet — it typically needs a field of around 1 A/m to saturate [38].

In the magnetization curve of a ferromagnet, if we travel between large enough external fields so that the material reaches the magnetization saturation, it is the maximum hysteresis achievable, called the major loop, Fig. 2.2(B). But if the cycling process stops before the field needed for saturation, then we have a minor loop. If we keep alternating the field direction and slowly decreasing the amplitude, the material will reach smaller and smaller loops until arriving at the origin. This process is called cyclic demagnetization [38].

The magnetization behavior as a function of the temperature is also an important feature, usually graphed as the inverse of the susceptibility (χ^{-1}) vs temperature

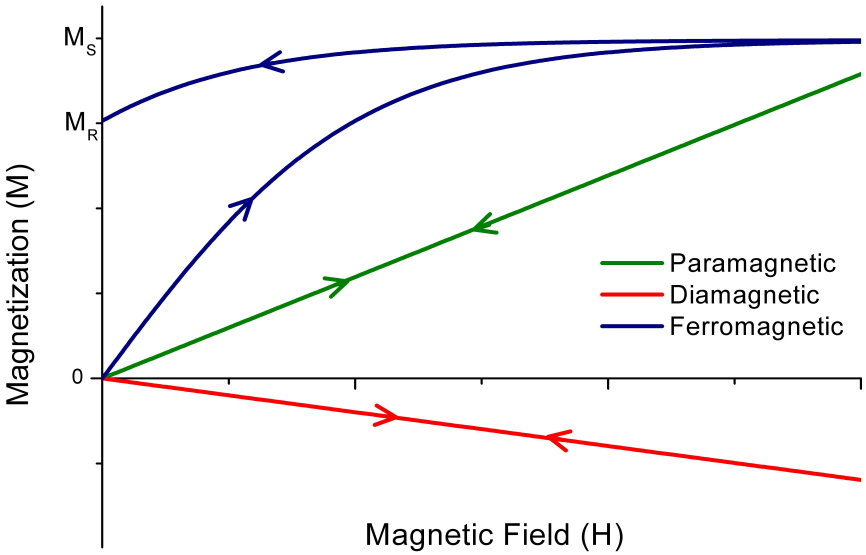

(A)

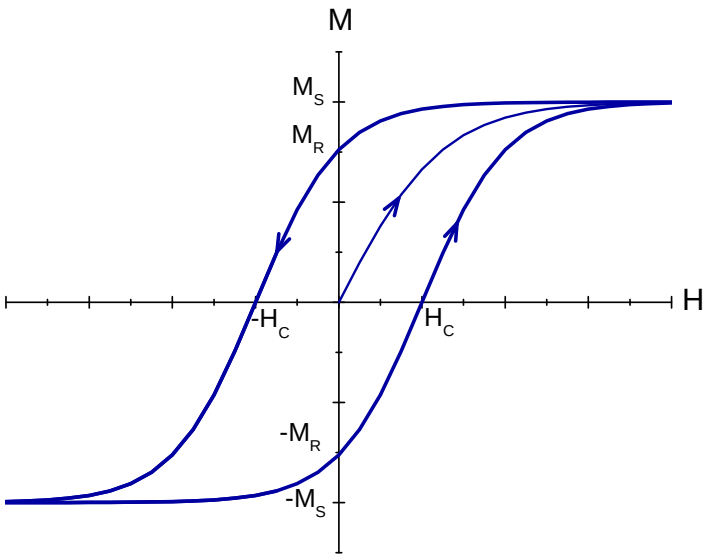

(B)

FIGURE 2.2: (A) Typical magnetization curve for a diamagnet (red), a paramagnet (green) and a ferri- or ferromagnet (blue). (B) A complete magnetization curve for a ferromagnet.

(T). For a paramagnet, it is given by eq. 2.5, where x is given by eq. 2.6.This leads to eq. 2.7 in the small x limit — low field and/or high temperature limit —, which is a straight line in the χ^{-1} vs T curve, known as Curie Law, where C is the Curie constant [37], Fig. 2.3(A).

$$M = M_0 \left[\left(1 + \frac{1}{2J}\right) \left[coth\left(1 + \frac{1}{2J}\right) x \right] - \frac{1}{2J} coth\left(\frac{x}{2J}\right) \right] \tag{2.5}$$

$$x = \frac{g\mu_0\mu_B JH}{k_B T} \tag{2.6}$$

$$\chi = \frac{\mu_0 n g^2 J(J+1)}{3k_B T} = \frac{C}{T} \tag{2.7}$$

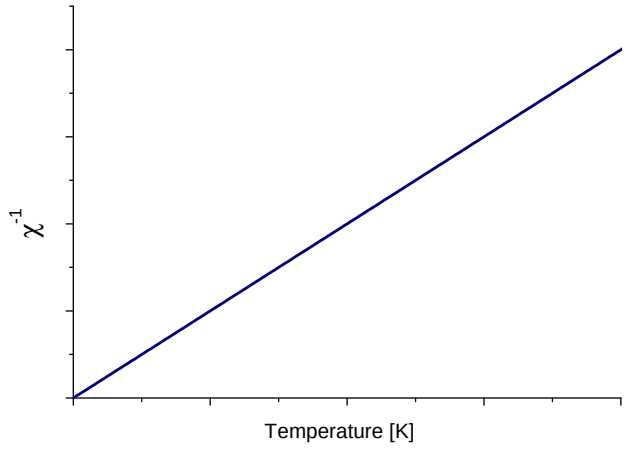

(A) Paramagnet

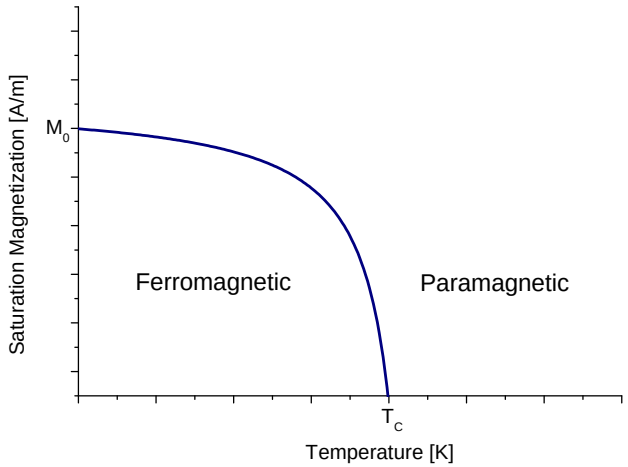

(B) Ferromagnet

FIGURE 2.3: (A) Paramagnetic inverse of magnetic susceptibility vs temperature, Curie law, eq. 2.7. (B) Ferromagnetic saturation magnetization vs temperature. The material transitions to a paramagnetic behavior above the Curie temperature (T_C).

For a ferromagnet, the magnetization saturation is decrescent with the temperature — its maximum value, M_0, occours, classically, at 0 K — and it reaches a critical temperature (the Curie temperature, T_C) where the magnetic order is destroyed, and above that, the material has a paramagnetic behavior, Fig. 2.3(B). Besides the cyclic demagnetization, another way of demagnetizing a ferromagnet is by heating it above its Curie temperature so that it becomes paramagnetic and then cool it down without any external fields. This is called thermal demagnetization.

2.2 Ferromagnetism

A ferromagnet is a magnetic material that, below its Curie temperature, can retain a long-range ordering of its unpaired magnetic moments even without the presence of an external field. The first breakthrough in understanding this behavior was the mean field theory by Pierre Weiss (1906), which postulated that a strong internal field — called the molecular field (H_M) — allows the atomic magnetic moments to align despite the effects of temperature [39]. This field is proportional to the material magnetization, eq. 2.8, where λ_M is the molecular field constant.

$$H_M = \lambda_M M \tag{2.8}$$

In order to explain the existence of the demagnetized states, Weiss also postulated the presence of magnetic domains, that are small regions within the ferromagnet, each of which is saturated, but in different direction, allowing the net magnetization to be zero. Therefore, the application of a magnetic field would make the domains rotate towards the field direction until the multi-domain state becomes a single-domain, the saturated state.

Although Weiss did not explain the physical origin of this molecular field, and the interaction terms that are ignored when applying a mean field theory, his two postulates — the spontaneous magnetization and the magnetic domains — are still accepted as the basis of understanding ferromagnetism [38]. As the local magnetization magnitude has a constant value, it is handy to use the magnetization direction vector ($\vec{m}$) only — the reduced magnetization —, as defined in eq. 2.9, where $\mid \vec{m} \mid^2 = 1$.

$$\vec{m} = \frac{\vec{M}}{M_S} \tag{2.9}$$

The current understanding of the magnetic interactions in a ferromagnet, which will ultimately be the physical cause of its behavior, can be described by the total magnetic free energy, eq. 2.10 . It contains several interaction terms, such as the exchange energy — the physical origin of the Weiss molecular field —, the Zeeman energy — the tendency of the magnetization to align to an external field —, the

long-range magnetostatic energy and the anisotropy energy, which will be further explained in the following sections.

$$E = E_{ex} + E_{Zeeman} + E_{ms} + E_A + ... \tag{2.10}$$

2.2.1 Exchange Energy

The spontaneous magnetization of a ferromagnet, the Weiss molecular field, was not elucidated until 1928 when Heisenberg introduced the quantum-mechanical exchange interaction, which arises from the indistinguishability of electrons [37]. This interaction between two adjacent spins can be described by the Heisenberg hamiltonian, eq. 2.11.

$$\mathcal{H} = -2J_{ex}\vec{S}_i \cdot \vec{S}_j \tag{2.11}$$

Where J_{ex} is the exchange integral, which is positive for ferromagnets — minimum energy exchange occurs when all spins are parallel — and negative for antiferromagnets. If we introduce a continuous $\vec{m}$ function in the lattice position r_j, we can also write the exchange energy for a pair of spins as 2.12.

$$E_{ex}^{pair} = -2J_{ex}S^2[(\vec{r}_j \cdot \nabla)\vec{m}]^2 \tag{2.12}$$

We can then derive the total exchange energy in a sample, eq. 2.13, where A_{ex} is the exchange stiffness constant, which measures how hard it is from a spin to deviate from the parallel configuration in a ferromagnet. For example, in a cubic system with lattice parameter a, the exchange stiffness is eq. 2.14. For permalloy, $A_{ex} = 1.3 \times 10^{-11}\,\mathrm{J\,m^{-1}}$.

$$E_{ex} = A_{ex} \int (\nabla \vec{m})^2 dV \tag{2.13}$$

$$A_{ex} = \frac{J_{ex}S^2}{a} \tag{2.14}$$

Essentially, the exchange energy measures the non-uniformity of the magnetization across the sample, eq. 2.13. It is minimum when the magnetization of the sample is entirely uniform [37].

2.2.2 Zeeman Energy

Zeeman energy term arises from the interaction between the spins and an external magnetic field ($\vec{H_{ext}}$). It can be described as eq. 2.15. It has its minimum value when the spins are parallel to the external field. For a large enough field, the sample will become saturated in the field direction.

$$E_{Zeeman} = -\mu_0 M_S \int \vec{m} \cdot \vec{H_{ext}} dV \tag{2.15}$$

2.2.3 Magnetostatic Energy

Besides the interaction with an external magnetic field, the material also interacts with its own magnetic field, the demagnetizing field or stray field ($\vec{H}_d$). The energy term derived from this interaction is the magnetostatic or stray field or dipolar energy.

From Maxwell's equation (eq. 2.16), we can derive an expression for the stray field, eq. 2.17. Thus, the sinks and sources of magnetization behave as "magnetic charges", although they never appear isolated [40]. The magnetostatic energy of a sample is evaluated as eq. 2.18.

$$\nabla \cdot \vec{B} = \nabla \cdot \mu_0(\vec{H} + \vec{M}) = 0 \tag{2.16}$$

$$\nabla \cdot \vec{H}_d = -\nabla \cdot \vec{M} \tag{2.17}$$

$$E_{ms} = \frac{1}{2}\mu_0 \int\limits_{allspace} \vec{H_d}^2 dV = -\frac{1}{2} \int\limits_{sample} \vec{H}_d \cdot \vec{M} dV \tag{2.18}$$

As an example, the stray field of an ellipsoid is linearly proportional to its magnetization, eq. 2.19, where N_d is the demagnetizing factor that is direction-dependent. Its magnetostatic energy is, then, eq. 2.20, where θ is the angle between the rotational symmetry direction and the magnetization [37].

$$\vec{H}_d = -N_d \vec{M} \tag{2.19}$$

$$E_{ms} = \frac{1}{2}\mu_0 M_S^2 V(N_\perp sin^2\theta + N_\parallel cos^2\theta) \tag{2.20}$$

Notice that there are different values for the demagnetizing factor for a parallel ($N_\parallel$) to the rotational symmetry axis direction and for a perpendicular direction ($N_\perp$) to it. This is known as shape anisotropy, which means that the dipolar energy is minimized for specific directions of magnetization — easy and hard axes of magnetization arise —.

For example, the needle of a compass will have an easy axis along its length, and for a thin film, in-plane magnetization is favoured. The magnetostatic energy is also the physical origin of the formation of magnetic domains, as we shall later see.

2.2.4 Anisotropy Energy

The anisotropy (or magnetocrystalline) energy arises from the charge distribution of the crystal field, which can be understood as the spin-orbit coupling between the magnetic momenta of the atoms and the crystal structure of the material, making certain crystallographic axes more energetically favoured than others [40].

In the simplest case, a material has an energy minimum at one specific axis: uniaxial anisotropy. Assuming that the anisotropy energy depends only on the angle (θ) between that axis and the magnetization direction can be written, for the two lowest energy terms as eq. 2.21, as: [37].

$$E_A = \int (K_{u_1} sin^2\theta + K_{u_2} sin^4\theta) dV \tag{2.21}$$

2.3 Magnetic Domains and Domain Walls

Even though a ferromagnet presents spontaneous magnetization, a macroscopic sample can exhibit demagnetized states. This is possible because magnetic materials are composed of magnetic domains — regions where all spins are parallel —, but as each domain can point at a different direction, the overall magnetization can be zero [37].

The physical origin of the division in domains comes mainly from the magnetostatic energy. For instance, consider a monodomain large crystal with uniaxial anisotropy, fig. 2.4a. Free poles on the top and bottom of the sample are a large source of demagnetizing field ($\vec{H}_d$), so the magnetostatic energy has a high value, eq. 2.18. If the sample splits into two oppositely magnetized domains (fig. 2.4b), the north and south poles become closer to one another, causing the energy to be reduced to almost half of the initial value [38].

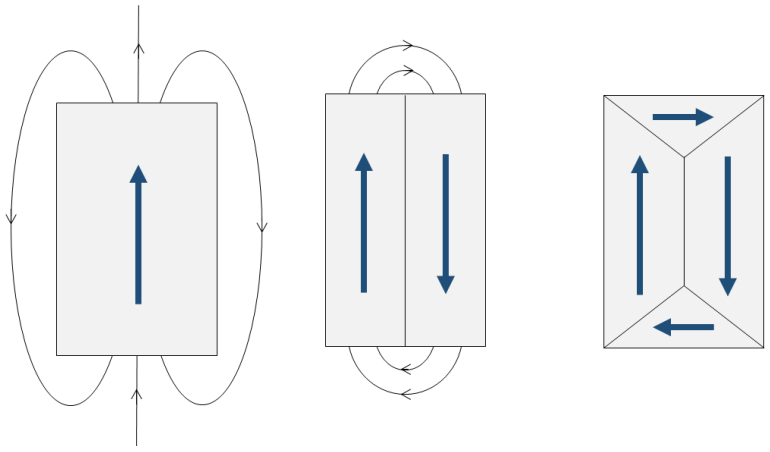

(A) Monodomain (B) Two Domains (C) Closure Domain

FIGURE 2.4: The division in domains lowers the magnetostatic energy of the sample.

We can define a single-domain critical diameter (D_{cr}) in which particles with dimensions below that constant are single-domains and above that, the division in domains is more energetically favorable. This can be done by finding the size conditions that the energy for a single and a two-domain structure are equal.

For example, let's consider an ellipsoid with two possible magnetic configuration with the magnetization in the major axis: (1) monodomain (fig. 2.4a) and (2)

two oppositely magnetized domains separated by a domain wall (fig. 2.4b). The magnetostatic energy for the single domain state (1), with a long semi-axis a and a short semiaxis b, and demagnetizing factor along the major axis $N_{\|}$ the free energy is: [37]

$$E_{ms}(1) = -\frac{1}{2}\mu_0 \vec{H}_d \cdot \vec{M}V = \frac{1}{2}\mu_0 N_{\|} M_S^2 \left(\frac{4}{3}\pi a^2 b\right) \tag{2.22}$$

For a two domain state (2), the magnetostatic energy taken as a integral over the whole space will have a negligible contribution at large distances, so the energy will be lower than the single state, which we will assume that the magnetostatic term is multiplied by a factor $\alpha < 1$.

Also, the domain wall energy shall be added, which is the surface energy density γ times the cross sectional area:

$$E_{ms}(2) = \alpha E_{ms}(1) + E_{wall} \tag{2.23}$$

$$E_{ms}(2) = \frac{1}{2}\alpha\mu_0 N_{\|} M_S^2 \left(\frac{4}{3}\pi a^2 b + \gamma\pi ab\right) \tag{2.24}$$

By equating the two expressions, the critical single-domain diameter for an ellipsoid, $D_{cr} = 2a$, is

$$D_{cr} = \frac{3\gamma}{(1-\alpha)N_{\|}\mu_0 M_S^2} \tag{2.25}$$

For a Bloch domain wall energy density ($\gamma = 4\sqrt{AK_u}$, eq. 2.30) and assuming $\alpha = 0.5$ for a sphere, which has $N_{\|} = 1/3$, one obtains:

$$D_{cr} = \frac{72\sqrt{AK_u}}{\mu_0 M_S^2} \tag{2.26}$$

If the sample splits into more and more domains, the dipolar energy becomes lower and lower, but this cannot continue indefinitely, since the transition region between one domain and its neighbours — the domain walls — increase the exchange and anisotropy energies of the system. If the domains have magnetization directions almost parallel to the surface of the sample, then we a have a closure-domain (fig. 2.4c), which are magnetic configurations with very low magnetostatic energy, as they avoid the presence of magnetic poles [37].

As stated above, domain walls are transition regions between two magnetic domains with different magnetization directions. For instance, consider a sample with two oppositely magnetized domains at the easy axis $\pm y$. If the transition is abrupt, then we have antiparallel spins at the interface, which will have a large energy associated with it. The energy can, then, be lower if the 180^o change take place gradually over N spins, so the angle between neighbouring spins is $\phi = \pi/N$ [38].

The exchange energy of the wall can be evaluated as:

$$E_{ex} = A\left(\frac{d\phi}{dx}\right)^2 \tag{2.27}$$

If we have a general anisotropy energy $E_K = g(\phi)$, then we can evaluate the total wall surface energy as:

$$\gamma_{wall} = \int_{-\infty}^{\infty} \left[A\left(\frac{d\phi}{dx}\right)^2 + g(\phi)\right] dx \tag{2.28}$$

There are two main types of domain walls: if the spins of the wall rotate perpendicular to the plane of the domain spins — the Bloch wall, fig. 2.5a — and if the spins of the wall rotate in the same plane of the spins of the domains — the Néel wall, fig. 2.5b —.

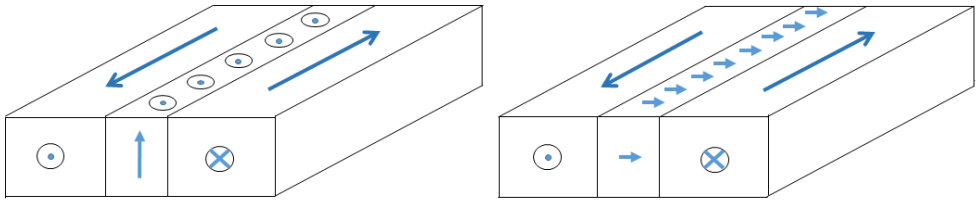

(A) Bloch Wall (B) Néel Wall

FIGURE 2.5: The two main types of domain wall.

In the Bloch wall (fig. 2.5a) the magnetization rotates parallel to the wall plane, which results in a zero global magnetic charge inside the wall. The stray field is, then, zero, making this wall the lowest energy one for a bulk material. Consider a 180^o Bloch wall separating two domains of opposite magnetization in a material with uniaxial anisotropy:

$$E_K = g(\phi) = K_u sin^2\phi \tag{2.29}$$

We can, then, obtain a Bloch wall total energy density (exchange and anisotropy), through eq. 2.28, as:

$$\gamma_{Bloch}^{uniaxial} = 4\sqrt{AK_u} \tag{2.30}$$

We can define a domain wall width as the product of the number of spins in the wall (N) multiplied by the spacing between them (a), in equilibrium, which can be obtained as

$$\delta_{Bloch} = Na = \pi\sqrt{\frac{A}{K_u}} \tag{2.31}$$

In the Néel wall (fig. 2.5b), as the magnetization rotates in plane, uncompensated magnetic charges arise, which makes the magnetostatic energy not negligible:

$$e_{ms} = -\frac{1}{2}\mu_0 M_s^2 cos\theta \tag{2.32}$$

As a consequence, the Néel surface energy density is higher than the Bloch wall:

$$\gamma_{Neel} = 4\sqrt{A\left(K_1 + \frac{1}{2}\mu_0 M_s^2\right)} \tag{2.33}$$

However, its wall width is lower than the Bloch wall:

$$\delta_{Neel} = \pi\sqrt{\frac{A}{K_1 + \frac{1}{2}\mu_0 M_s^2}} \tag{2.34}$$

Therefore, although the Bloch wall has a lower energy density for thick samples, in thins film, with thicknesses in the order of magnitude of the Bloch width, the Néel wall becomes the favoured structure.

There is also another kind of domain wall in thin films, the cross-tie wall. This is an intermediate between the Néel and the Bloch walls and is composed of a line of vortices and antivortices that are formed as an attempt to mix the magnetic charges on the wall and reduce the magnetostatic energy. Basically, if the film is thin enough, Néel walls are the lowest energy state, and, as the thickness grows, the cross-tie wall becomes more favorable, followed by the Bloch wall [38].

2.4 Micromagnetic Equations

Micromagnetism is an approach for describing magnetic materials that, instead of studying each spin and its interactions, considers the magnetization as a continuous function $\vec{M}(\vec{r})$. The sample is then divided in volumes that are larger than the atomic scale but small enough so that magnetic domains and domain walls can be resolved.

2.4.1 Energy Minimization

If a sample is smaller than a critical size, the magnetization will be parallel everywhere. If it exceeds this size, it will divide into domains and the direction of $\vec{M}$ will vary with the position. The magnetic configuration of the sample $\vec{M}(\vec{r})$ can, then, be obtained by the total energy (eq. 2.35) minimization of the specimen [38].

$$E = E_{ex} + E_A + E_{ms} + E_{Zeeman} + ... \tag{2.35}$$

We can define all the interactions that lead to energy terms (exchange, anisotropy, stay field) as an effective field:

$$\vec{H}_{eff} = -\frac{1}{V}\frac{\partial E}{\partial M} \tag{2.36}$$

The minimization of energy leads to $\vec{m}(\vec{r})$ being parallel to $\vec{H}_{eff}$. As a consequence, the torque that $\vec{H}_{eff}$ exerts in $\vec{m}$ is zero:

$$\mu_0 \vec{m} \times \vec{H}_{eff} = 0 \tag{2.37}$$

For instance, we can write eq. 2.38 for a material with uniaxial anisotropy.

$$E = \frac{\mu_0 M_S^2}{2} \int_V \left[\frac{2A}{\mu_0 M_S^2} (\nabla \vec{m})^2 + \frac{2K_u}{\mu_0 M_S^2} e_A(\theta) - \frac{1}{M_S} \vec{m} \cdot \vec{H}_d - \frac{2}{M_S} \vec{m} \cdot \vec{H} \right] dV \tag{2.38}$$

From this equation, the coefficient of the first term is called l_{ex}^2, the square of the exchange length (2.39), which is a length scale in which the exchange interaction dominates magnetostatic effects in that material [37].

$$l_{ex} = \sqrt{\frac{2A}{\mu_0 M_S^2}} \tag{2.39}$$

2.4.2 Magnetization Dynamics

In an equilibrium condition, the torque that the effective field exerts on the magnetization is null (eq. 2.37). But if the magnetization is withdrawn from equilibrium (by applying an external magnetic field, for example) a finite torque will be exerted and we can find an equation of motion as eq. 2.40, where γ_e is the electron gyromagnetic ratio.

$$\frac{d\vec{M}}{dt} = -\gamma_e \mu_0 (\vec{M} \times \vec{H}_{eff}) \tag{2.40}$$

This equation describes a precession of $\vec{M}$ around $\vec{H}_{eff}$. The system would keep this motion endlessly if no damping mechanism existed. The damped system precesses until it reaches a new equilibrium configuration. The relaxation mechanism is described phenomenologically by the Gilbert damping term (α), through the Landau-Lifshitz-Gilbert (LLG) equation:

$$\frac{d\vec{M}}{dt} = -\gamma \vec{M} \times \vec{H}_{eff} + \frac{\alpha}{M_S} \vec{M} \times (\vec{M} \times \vec{H}_{eff}) \tag{2.41}$$

2.5 Magnetic Configurations in Permalloy Rectangles

The magnetic ground state configuration of a sample is found out by the energy minimization micromagnetic equation. Nevertheless, this is not a trivial issue, as it can vary with the sample exact shape, size and its magnetic history.

This problem became clear when NIST proposed its standard problem 1 (SD1): the hysteresis loop of a $2\mu m$ x $1\mu m$ x $20nm$ permalloy rectangle, fig. 2.6. The anonymously submitted results presented very different coercive fields and different magnetic states. These discrepancies have been explained though programming problems, underdiscretization and different starting conditions [41].

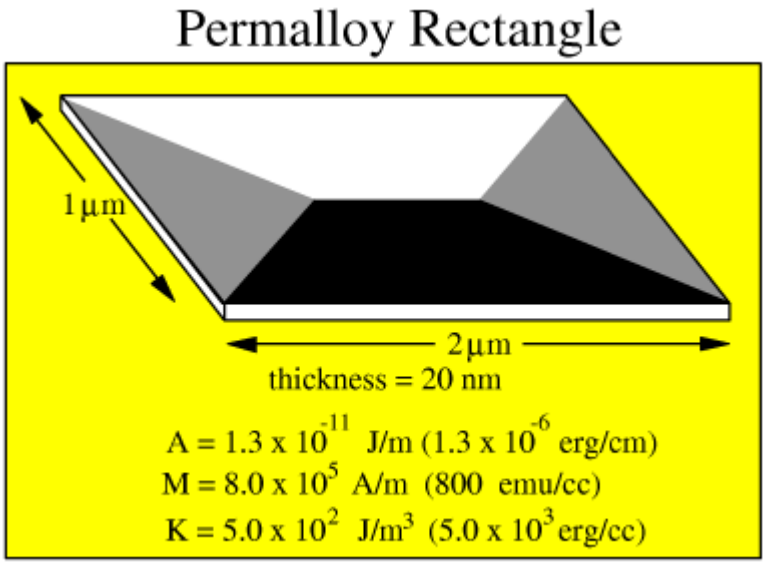

FIGURE 2.6: NIST Standard problem 1.
Source: https://www.ctcms.nist.gov/ rdm/mumag.org.html

Permalloy is a soft magnetic material with low magnetocrystalline anisotropy. In thin films, the magnetic configuration tends to be in-plane due to shape anisotropy. The low energy magnetic states are ultimately determined by the competition between the exchange energy, which tends to align the neighbouring spins, and the magnetostatic energy, that tends to form flux-closure states.

Several magnetic configurations are known for micron-sized permalloy rectangles, between stable and metastable states, the main ones are shown in fig. 2.7. They can be divided in basically two categories: (1) high average magnetization: the $C-$, S- and flower states, and (2) low average magnetization (flux-closure): diamond, Landau and cross-tie states.

The high average magnetization configurations are essentially uniform states. The boundary creates a shape anisotropy in which the dipolar energy is minimized through a rotation of the magnetic moments at the edges. This rotation characterizes the type of state: S-, C- or flower. These states are the lower energy ones in very small particles, in which the exchange energy dominates (typically for lengths smaller than 100 nm), and in high aspect ratio elements, as the large distance between opposite poles decreases their magnetostatic energy [41].

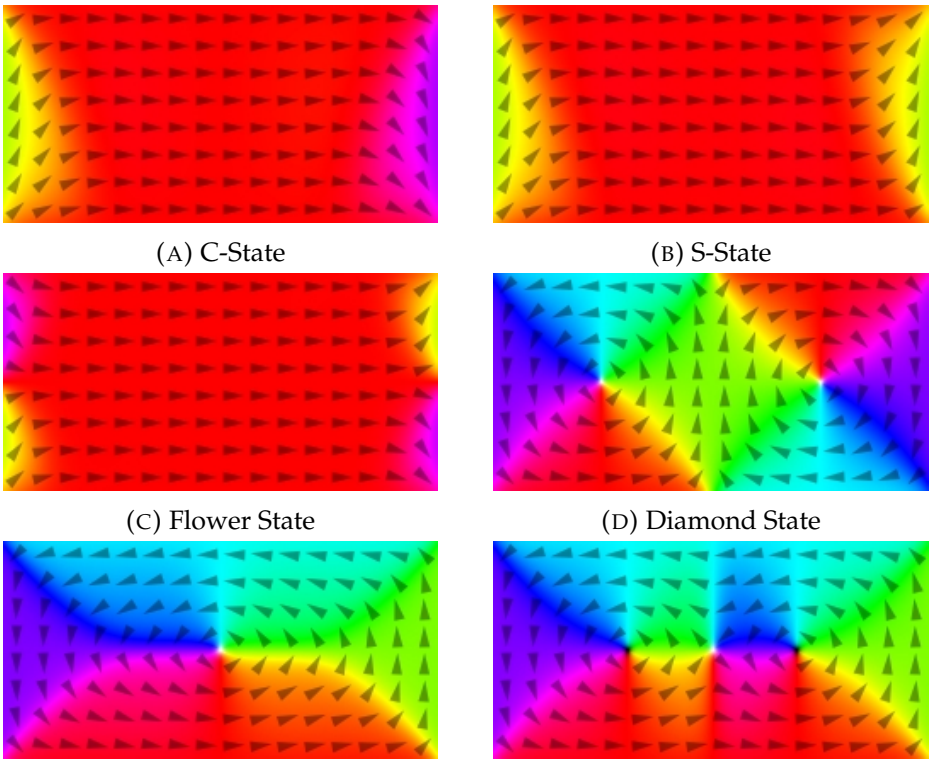

(A) C-State (B) S-State

(C) Flower State (D) Diamond State

(E) Landau State (F) Cross-Tie State

FIGURE 2.7: Magnetic configurations in thin-film permalloy rectangles. Images obtained from a 2 μm x 1 μm x 5 nm permalloy rectangle simulation from the micromagnetic simulation software Mumax3[35].

Typically, the S- and C- states are the minimum energy when the exchange interaction dominates over the magnetostatic one. S- or C- state transition to the flower state often only happens in high external fields, due to the Zeeman energy contribution. S- and C- states are nearly degenerate states, although the C-state is slightly favoured for small particles [41].

The low net magnetization configurations are flux-closure states, thus they minimize the magnetostatic energy of the system with the division in domains and domain walls. If the length of a permalloy rectangle keeps increasing from a S- or C- state, typically a transition to the Landau state will be the first to happen. The Landau state (fig. 2.7e), consists of 4 magnetic domains that effectively closes the flux with a relatively narrow 180^o Néel wall at its center, that is separated in two through a magnetic vortex.

Although 90^o walls are energetically more favourable than 180^o ones, they have a larger width, which makes the diamond state (fig. 2.7d) the most favourable one for higher lengths. The simpler diamond state consists of 7 domains, with 2 vortexes with opposite circularities. At higher aspect ratios more domains and vortexes with alternating circularities may appear.

Finally, the cross-tie state (fig. 2.7f) is an intermediate between the Néel wall,

which is favoured in low thicknesses, and the Bloch wall, favoured in higher thicknesses. It consists of a Landau state, with a Néel wall with extra vortexes and antivortexes between them. The energy of a 90^o Néel wall is about 12% of the 180^o one, so the total energy is lowered by replacing a 180^o Néel wall by the rather complex cross-tie configuration [40]. The one shown in fig. 2.7f is a single cross-tie, but for different aspect ratios, sizes and thicknesses, much more complex structures, with more vortexes, might appear.

2.6 Spin Waves

A local perturbation in the magnetization can propagate across a magnetic material in a wave-like manner, the so-called spin waves. They were first introduced in 1930 by Bloch [7] in order to explain the saturation magnetization reduction with the increasing of temperature. At 0 K, all the spins are parallel. When the temperature rises to a finite value, although much smaller then the Curie temperature, low-energy collective excitations of exchange-coupled spins lowers the sample's magnetization in a $T^{3/2}$ manner.

These excitations correspond, in a classical analogy, to a linear chain of spins precessing around an effective field, with the same frequency, but with a small phase change between neighbours, fig. 2.8. If the phase difference between them is large, then the spin-wave wavelength is small, we say that the system is in the exchange regime. If the phase difference is small, then the wavelength is large ($\lambda \gg l_{ex}$) and the dipolar interaction dominates, the magnetostatic regime is achieved.

In the magnetostatic regime, in which the dipolar interaction is the main restoring force, the spin-waves are typically much more dispersive than electromagnetic waves, with eigenfrequencies in the low-GHz range, and also, they are anisotropic, even for isotropic media, as shall be seen in the dispersion relation for an infinite thin film. At the low wavelength exchange regime, the spin-waves tend to be more isotropic, with frequencies that can go up to the THz range, and with group velocities that increases with the wavevector [8].

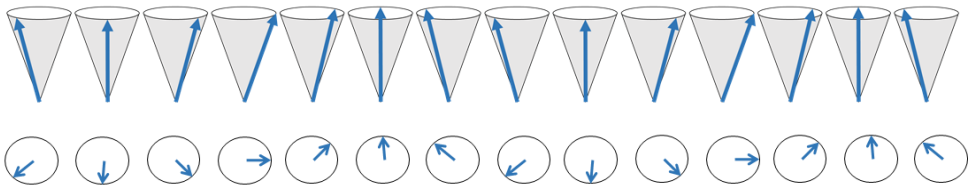

FIGURE 2.8: Pictorial representation of a spin wave.

Let's consider a linear chain of n spins, separated by a distance a, coupled by the exchange interaction only. The Heisenberg hamiltonian is eq. 2.42, where we assume that only the nearest neighbours interactions are not negligible, also $s = 1/2$

and $J_{ex} > 0$. It can be shown [42] that the eigenvalue of the energy in that system is eq. 2.43. In the $ka \ll 1$ limit, the dispersion relation reduces to the quadratic eq. 2.44, which was the first dispersion relation derived for a spin wave, made by Bloch [7].

$$\mathcal{H} = -2\frac{J_{ex}}{\hbar}\sum_n \vec{S}_n \cdot \vec{S}_{n+1} \tag{2.42}$$

$$E = \hbar\omega = 2J_{ex}(1 - cos(ka)) \tag{2.43}$$

$$\omega = \frac{J_{ex}a^2}{\hbar}k^2 \tag{2.44}$$

For a ferromagnetic material, we want to consider not only the exchange, but also magnetostatic, Zeeman and anisotropy energies. In order to do so, we have to use the macroscopic Landau-Lifshitz equation for the motion of the magnetization (eq. 2.40), where we decompose the magnetization and effective field in static and dynamical components:

$$\vec{M}(t) = M_S\hat{z} + \vec{m}e^{i\omega t} \tag{2.45}$$

$$\vec{H}_{eff}(t) = H_0\hat{z} + \vec{h}e^{i\omega t} \tag{2.46}$$

The magneto-quasi-static approximation of the Maxwell equations can be used when the spin wave wavelength is much different from that of an electromagnetic wave of the same frequency ($k \gg \omega\sqrt{\epsilon}/c$). From that, we can write the magnetostatic scalar potential $\vec{h} = -\nabla\psi$, and obtain the Walker's equation [42]:

$$(1+\chi)\left[\frac{\partial^2\psi}{\partial x^2} + \frac{\partial^2\psi}{\partial y^2}\right] + \frac{\partial^2\psi}{\partial z^2} = 0 \tag{2.47}$$

For an infinite bulk material, we may consider uniform infinite plane wave solutions for $\vec{h}$ and $\vec{m}$, and, by applying them to eq. 2.47, one can arrive in the dispersion relation [42]:

$$\omega(k) = \sqrt{(\omega_0 + \omega_M A k^2)(\omega_0 + \omega_M A k^2 + \omega_M sin^2\theta)} \tag{2.48}$$

Where A is the exchange stiffness, θ is the angle between the effective field H_{eff} and the wave propagation direction k, also:

$$\omega_0 = \gamma\mu_0 H_0 \tag{2.49}$$

$$\omega_M = \gamma\mu_0 M_S \tag{2.50}$$

For $k = 0$ we have $\lambda \to \infty$, which means a uniform movement where all spins are precessing in phase. This is the ferromagnetic resonance (FMR) mode, and it is dominated by the long-range magnetostatic interaction. Its frequency is given by eq. 2.51. Thus, for the exchange regime (high k) we get the typical quadratic dispersion

(eq. 2.52).

$$\omega_{FMR} = \omega(k = 0) = \sqrt{\omega_0(\omega_0 + \omega_M sin^2\theta)} \tag{2.51}$$

$$\omega(k \to \infty) = \omega_M A k^2 \tag{2.52}$$

For a finite body, boundary conditions must be applied at the sample surface in the Walker's equation. For example, this was done by Kittel [43] for a ellipsoid with demagnetizing factors N_x, N_y and N_z, and static field in the z-direction (H_0), in which he arrived in the uniform mode:

$$\omega_{FMR} = \gamma\sqrt{[H_0 + (N_y - N_z)M_S][H_0 + (N_x - N_z)M_S]} \tag{2.53}$$

2.6.1 Spin Waves in Thin Films

The spin wave dispersion curve for a saturated ($\vec{M} \parallel \vec{H}_0$) thin film with thickness d in the magnetostatic regime was first derived by Damon and Eshbach in 1961 [44]. There are basically three possible geometries: (1) the film is magnetized perpendicularly to its plane (fig. 2.9a), (2) the film is magnetized in-plane and the wave vector is parallel to the magnetization ($\vec{k} \parallel \vec{M}$, fig. 2.9b) and (3) also in-plane magnetization, but the magnetization and wave vector are perpendicular to each other ($\vec{k} \perp \vec{M}$, fig. 2.9c).

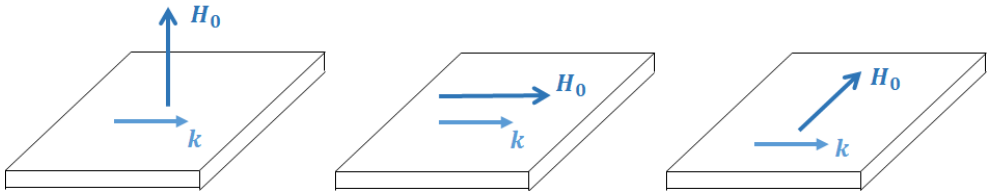

(A) MSFVM (B) MSBVM (C) MSSM

FIGURE 2.9: Different geometries for spin waves propagating in a thin film. (A) Magnetostatic Forward Volume Modes (MSFVM). (B) Magnetostatic Backward Volume Modes (MSBVM). (C) Magnetostatic Surface Modes (MSSM).

If a plane wave is excited with wave vector $\vec{k} = \vec{k}_\parallel + \vec{k}_\perp$, where these are, respectively, the parallel and perpendicular to the plane components. We will apply the Walker's equation (eq. 2.47) inside the film, and, outside the film, as $\chi = 0$, it reduces to the Laplace's equation ($\nabla^2\psi = 0$).

(1) For the first geometry, a normally magnetized film, fig. 2.9a, we apply the appropriate boundary conditions [42], the dispersion relation can be calculated for the lowest-order mode as eq. 2.54:

$$\omega_{MSFVM} = \sqrt{\omega_0\left[\omega_0 + \omega_M\left(1 - \frac{1 - e^{-k_\parallel d}}{k_\parallel d}\right)\right]} \tag{2.54}$$

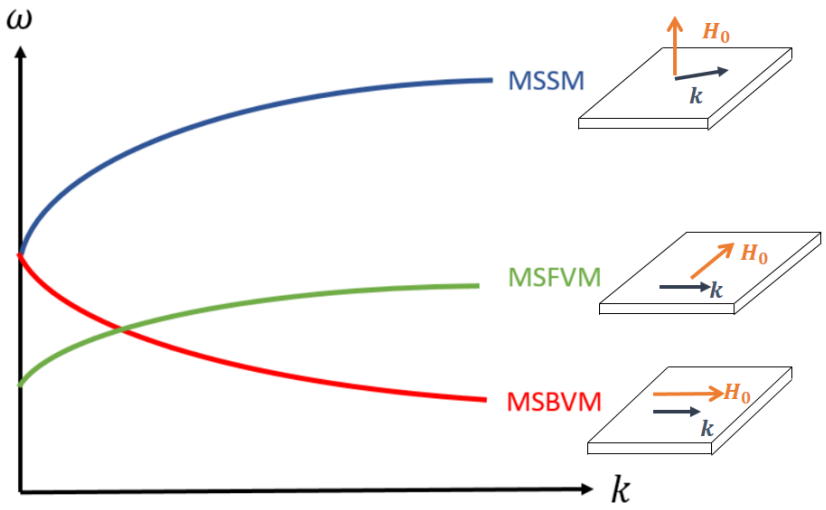

FIGURE 2.10: Typical dispersion relation for the lowest-order magnetostatic mode for each geometry.

These waves have a positive dispersion, see fig. 2.10, (frequency increases with k), therefore the phase ($v_{ph} = \omega/k$) and group velocities ($v_g = \partial\omega/\partial k$) are both in the same direction, which is the definition of a forward wave. The dispersion only depends in the magnitude and not the direction of $k_{\parallel}$, which means that there is a isotropic wave propagation in the film plane. Also, the amplitude is distributed sinusoidally throughout all the volume. These waves modes are, then, called *magnetostatic forward volume modes* (MSFVM).

(2) For a tangentially magnetized film with $\vec{k} \parallel \vec{M}$ (fig. 2.9b) the dispersion relation for the lowest-order mode is:

$$\omega_{MSBVM} = \sqrt{\omega_0 \left[\omega_0 + \omega_M \left(\frac{1 - e^{-k_\perp d}}{k_\perp d} \right) \right]} \tag{2.55}$$

These waves have a negative slope, fig. 2.10, (frequency decreases with k), which results in a negative group velocity, so the group and phase velocities have different directions (backward wave). Also, the dispersion does not change by reversing the in-plane direction of propagation and, just like for the last geometry, the amplitude is distributed sinusoidally throughout the whole volume of the sample. These are the *magnetostatic backward volume modes* (MSBVM).

(3) Finally, for the tangentially magnetized film with $\vec{k} \perp \vec{M}$ (fig. 2.9c), the following dispersion curve can be obtained:

$$\omega_{MSSM} = \sqrt{\omega_0(\omega_0 + \omega_M) + \frac{\omega_M^2}{4}[1 - e^{-2kd}]} \tag{2.56}$$

In this mode, the wave amplitude decays exponentially from the surface of the film,

and for that it is called *magnetostatic surface mode* (MSSM) — also known as Damon-Eshbach (DE) mode. The phase and group velocities point in the same direction, fig. 2.10. The dispersion relation is invariant to the reversal of the propagation direction, but the mode is not. Actually, the fields of the mode change from one surface of the film to the other when the propagation direction is reversed, this is called field displacement non-reciprocity [42].

These results were generalized by Kalinikos and A N Slavin in 1986 through the use of perturbation theory [45]. They have taken in account not only the magnetostatic interaction but also the exchange energy — the dipole-exchange spin waves — in thin films for an arbitrary polar (ϕ) and azimuthal (θ) angles of magnetization for a film in the xy plane with thickness d. The derived dispersion relation:

$$\omega(k) = \sqrt{(\omega_H + \omega_M A k_\parallel^2)(\omega_H + \omega_M A k_\parallel^2 + \omega_M F_{nn})} \tag{2.57}$$

$$F_{nn} = P_{nn} + sin^2\theta \left(1 - P_{nn}(1 + cos^2\phi) + \omega_M \frac{P_{nn}(1 - P_{nn})sin^2\phi}{\omega_H + \omega_M A k_\parallel^2} \right) \tag{2.58}$$

Where, the matrix element P_{nn} varies in the range $0 < P_{nn} < 1$, and will have different expressions for pinned and unpinned surfaces. For a unpinned surface, the expression is

$$P_{nn'} = \frac{k_\perp^2}{k_{n'}^2}\delta_{nn'} + \frac{k_\perp^4}{k_n^2 k_{n'}^2} \frac{[1 - (-1)^n e^{-k_\perp L}]}{k_\perp d} \frac{1 + (-1)^{n+n'}}{\sqrt{(1 + \delta_{0n})(1 + \delta_{0n'})}} \tag{2.59}$$

Which, for the lowest order mode it becomes:

$$P_{00} = 1 - \frac{1 - e^{-kd}}{kd} \tag{2.60}$$

In summary, eq. 2.57 generalizes the spin-waves modes that can be obtained in a thin film. In the low wavevelength limit, the exchange-dominated regime, the equation presents a quadratic relation. In the magnostatic regime, long wavelength limit, the equations for the forward surface modes, and backward and forward volume modes can be obtained by applying the appropriate azimuthal and polar angles.

Chapter 3

Methods

3.1 Micromagnetic Simulations

Micromagnetic simulations are important tools for the prediction of magnetic domain structures and the dynamic behavior of magnetic micro- and nano-sized elements. It is suited for a length scale that is large enough so that the atomic structure can be neglected, but small enough for domain walls to be noticeable.

MuMax3 [35] was employed for that purpose, which is an open-source GPU-accelerated micromagnetic simulation software, written in Go language and CUDA, that uses a finite-difference discretization method. Static simulations are executed through the *relax()* command, which is an energy minimization method followed by a torque minimization. The dynamics of magnetization is evaluated by a Runge-Kutta (RK45) method for solving the Landau-Lifshitz torque equation (eq. 3.1), for a specified gyromagnetic ratio (γ) and Gilbert damping parameter (α).

$$\tau = \frac{\gamma}{1+\alpha^2}(\vec{m} \times \vec{H}_{eff} + \alpha(\vec{m} \times (\vec{m} \times \vec{H}_{eff}))) \tag{3.1}$$

The discretization of the sample is a critical issue as a small cell size is desired for obtaining a high resolution, but at the same time it demands computational memory and time. On the other hand, in order do get reliable solutions, the cell length has to be smaller than the material exchange length (eq. 2.39).

As we have simulated permalloy structures, an exchange stiffness $A = 13 \times 10^{-12} J/m$ and a saturation magnetization $M_S = 8 \times 10^5 A/m$ were assumed [46]. The exchange length for permalloy is approximately $l_{ex} \approx 5.7nm$. Therefore, the cell sizes we used were $L \leq 5nm$. The phenomenological Gilbert damping parameter for the permalloy thin film structures was set to $\alpha = 0.007$ [47].

The investigation of the dynamical response of a structure to an alternate external magnetic field was done through a sinc-function pulse, eq. 3.2 (Fig. 3.1a). The Fourier transform (FT) of the sinc-function is a step-function (Fig. 3.1b) that

simultaneously excites all the frequencies up to a cut-off frequency (f_0). The sample's magnetization response to that pulse is then saved as a function of time. After performing a The FFT-intensity peaks correspond to a ferromagnetic resonance state.

$$H_{ext}(t) = H_0 \frac{sin(2\pi f_0 t)}{2\pi f_0 t} \tag{3.2}$$

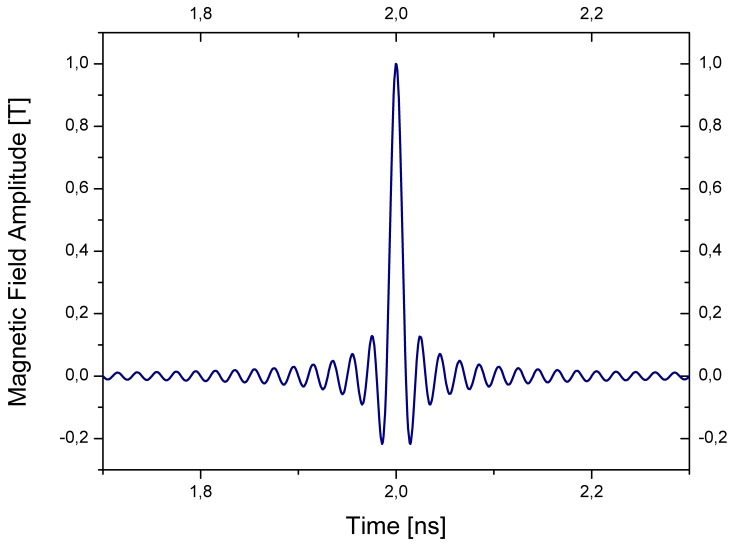

(A) Sinc-Function.

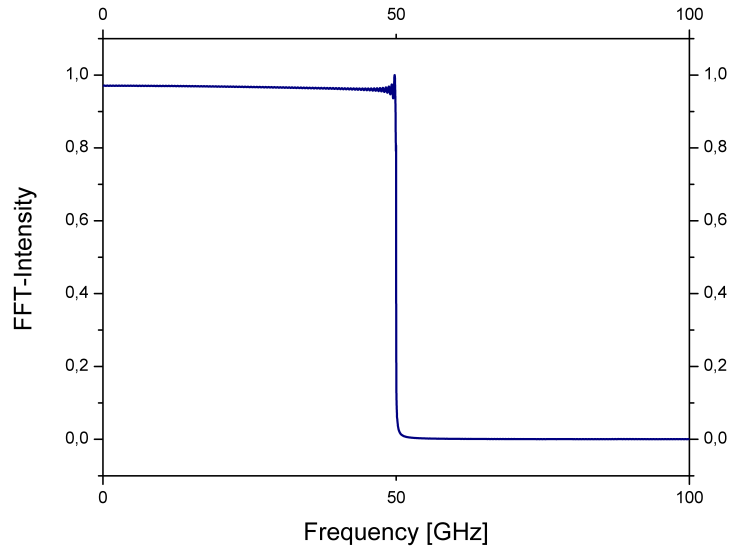

(B) Sinc-Function Fourier transform.

FIGURE 3.1: (A) The Sinc-Function with a cut-off frequency of 50 GHz and (B) its fast Fourier transform in the frequency domain.

3.1.1 Static Magnetization Methods

3.1.1.1 Magnetic Ground-State

In order to obtain the magnetic ground state of permalloy rectangles, the following method was applied:

1. The length and width of the rectangle is defined;
2. An initial magnetization sate was defined between uniform (S, C or flower), Landau or diamond states with a random noise applied in each one;
3. The *relax()* command is applied until a minimum energy and minimum torque state is achieved;
4. The total energy (exchange and magnetostatic) are saved;
5. A total energy vs. size curve is plotted.

3.1.1.2 Hysteresis Curves

The method for obtaining magnetization curves are:

1. The length, width and initial magnetization state are defined;
2. The system is relaxed and the final magnetization state is saved;
3. An external magnetic field is applied in steps of δB = 0.1 mT;
4. In each step, the system is relaxed and the magnetization is saved;
5. A magnetization vs. applied field curve is plotted for a specific direction.

3.1.2 Magnetization Dynamics Methods

3.1.2.1 Magnetic Eigenmodes

The dynamic response of the system to an alternate external magnetic field is obtained as:

1. The initial magnetization is defined and relaxed;
2. A sinc-pulse is applied as an external magnetic field in a specific region of the sample (antenna) in the z-direction (out-of-plane);
3. The system is allowed to respond to the pulse and the z-magnetization is saved until it returns to equilibrium;
4. The magnetization as a function of time is Fourier transformed;
5. A FFT intensity vs. frequency curve is plotted.

3.1.2.2 Dispersion Relation

The dispersion relation, group velocity and propagation length of the waves is obtained as:

1. The initial magnetization is defined and relaxed;
2. An out-of-plane sinusoidal pulse is applied with a specified frequency (varying in δf = 0.25 GHz) as an external field in a specific region of the sample;
3. The magnetization components in each cell is saved as a function of time;
4. The z-magnetization is plotted against the x-component for a fixed y-position ($y = 0$, at the center);
5. The curve is fitted as a damped sine wave (eq. 3.3), and the wavenumber (k) and damping coefficient (propagation length, Λ) are obtained.

$$m_z(x) = m_0 \, sin(kx + \phi) \, e^{-x/\Lambda} \tag{3.3}$$

6. A frequency vs. wavenumber (dispersion relation) and a propagation length vs. frequency curves are plotted;
7. The dispersion relation curve is derived and multiplied by 2π in order to obtain a group velocity vs. frequency curve (eq. 3.4).

$$v_g = 2\pi \frac{\partial f}{\partial k} \tag{3.4}$$

3.2 Fabrication of Samples

Lithography and metal deposition techniques were employed for the production of nano/micron-sized structures at LABNANO/CBPF.

Optical and electron-beam lithography are conventional methods for nano/micron-sized structures fabrication. Optical lithography uses light to change the chemical proprieties of a photosensitive resin (also known as resist) to create a micron-sized pattern. In order to achieve sub-micron scale patterning, electron-beam lithography is typically employed. It uses a collimated electron beam from a scanning electron microscope to create the pattern on a resist.

The resist is a photosensitive or electron-sensitive polymer in a solvent. It works as a mask, protecting some areas from etching or avoiding metal deposition to occur. A positive resist, used in additive lithography processes, will suffer chemical bonds breaking after being exposed, which will lower its molecular weight and make the exposed areas more soluble to some solvents (called developers). Besides, the opposite happens in a negative resist, used in subtractive lithography, the exposition

causes a local polymerization or cross-linking, which increases its molecular weight, making the exposed areas less soluble.

In the additive process, the one used in this thesis, see fig. 3.2, a resist, spun on a substrate, is exposed either to light or to an electron-beam, then it is developed in order to remove only the desired areas. After, a thin film is deposited and the resist is lifted-off and only the exposed areas remain on the substrate.

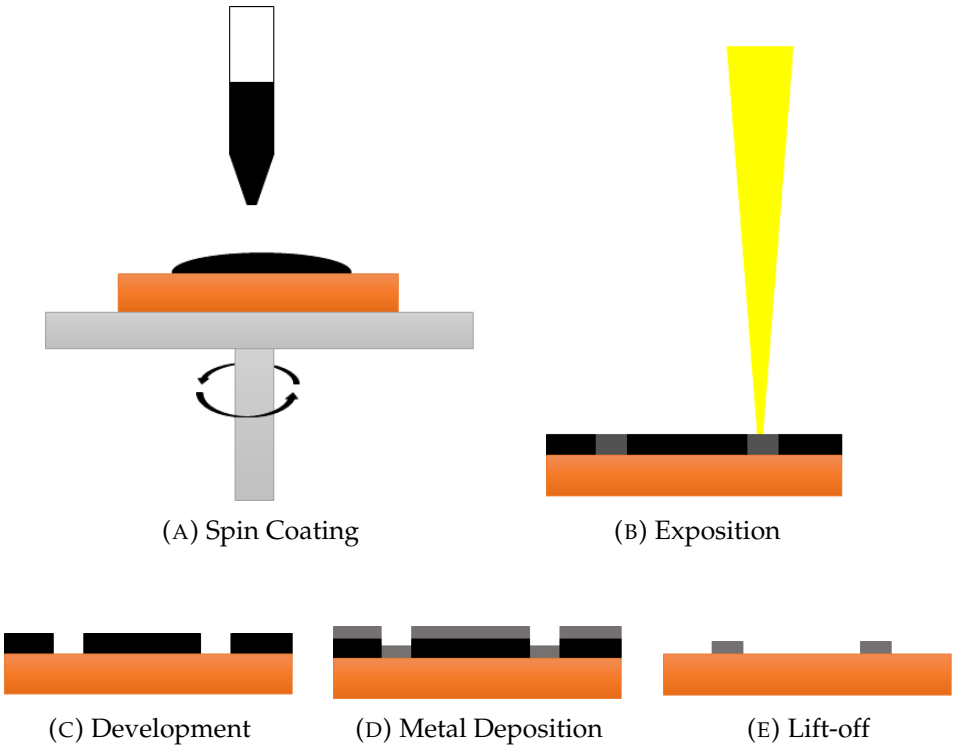

(A) Spin Coating (B) Exposition

(C) Development (D) Metal Deposition (E) Lift-off

FIGURE 3.2: Additive lithography with positive-resist steps.

In the subtractive process, the thin-film is first deposited on top of the substrate, and only after that, a resist is spun over the film. The resist is then exposed, followed by a developing process that removes the desired areas, leaving the film exposed. Later on, a plasma etching process is employed to corrode the non-protected metal until reaching the substrate. Then, either an oxigen plasma etching and/or a lift-off step, is used to remove the remaining resist, leaving only the metallic designed pattern.

3.2.1 Optical Lithography: Positive Resist

Optical Lithography was applied in order to achieve structures with dimension sizes above 10 μm. An overview of the process is schematically shown in fig. 3.2.

Inside the class 1000 cleanroom at LABNANO/CBPF, a positive AZ1505 resist from Clariant with spectral photosensitivity between 310 and 440 nm is deposited on a Si/SiO_2 substrate through a spin coating process. The substrate is fixed inside

the spinner and resist is applied at its center. The system then starts to rotate at 4000 rpm for 40 seconds in order to spread the resist over the whole surface with a homogeneous thickness of 0.5 μm. The substrate is then placed in a hot plate at 100^oC for 60 seconds for polymer curing.

The sample is then placed inside a Heidelberg μPG 101 Laser Writer where a pattern will be exposed on the photoresist through a laser beam with a specific power and pixel exposure time. The pattern is designed in a computer-aided design open-source software, Libre CAD. To determine the optimum power and exposure time, for each design a dose test is performed.

The dose test consist in the exposing the same design several times, each of which have a different power but the same pixel exposure time. After that, a second dose test is done with that specific power, but with varying exposure times. The system is again analyzed to find the best value. For our samples, we a power of 5 mW was used with a relative pixel exposure time between 40% - 60%. A Clariant AZ 300 MIF Photoresist Developer is then applied for 60 seconds on the sample in order to solubilize only the laser-exposed areas leaving the substrate unprotected exclusively in these places.

Magnetron Sputtering is then used for the desired metal deposition, which will be further explained in section 3.2.3. The whole surface of the substrate is covered with the metal and in the last step, the lift-off, the sample is submerged in acetone, which will dissolve the remaining resist, leaving the developed areas only, where the metal was deposited directly to the substrate. The system is placed in a ultrasonic bath, for at least 5 minutes, until all the resist is dissolved. The substrate is then cleaned with isopropyl alcohol followed by deionized water, and it is dried with an air flow so that no stains are left on the surface.

The optical lithography with positive resist process is summarized below:

1. **Resist deposition**: AZ1505 Clariant resist is deposited on a SiO_2 substrate in a spin coater at 4000 rpm for 40 seconds, followed by 60 seconds in a hot plate at 100^o C.
2. **Exposition**: The pattern is exposed in a μPG 101 Laser Writer, with a previously optimized dose and exposure time.
3. **Development**: the sample is submerged in a Clariant AZ 300 MIF photoresist developer for 60 seconds.
4. **Metallization**: a thin-film metallic layer is deposited through magnetron sputtering with the desired thickness.
5. **Lift-off**: the sample is submerged in acetone and placed in an ultrasonic bath until all the resist is dissolved.

3.2.2 Electron-Beam Lithography: Positive Resist

Electron-Beam Lithography was applied for obtaining structures with dimension sizes below 10 μm. An overview of the process is schematically shown in Fig. 3.2.

At a class 1000 cleanroom at LABNANO/CBPF, a positive AR-P 672.045 resist from ALLRESIST, which is PMMA 950 K dissolved in anisole, is spun on a Si/SiO_2 substrate at 4000 rpm for 60 seconds in order to achieve a 0.23 μm thickness. It is then placed in a hot plate at 150^oC for 3 minutes for solvent evaporation.

The sample is placed in a Raith e-LiNE lithographic system.The electron-beam expositions have been performed at a z = 29 mm height, aperture size 30 μm, 20 kV of acceleration voltage and a write field of 100 μm. For each sample the electron microscope image has to be optimized for aperture alignment, astigmatism and working distance.

The working distance for the samples is around 5.4 mm, and it is optimized by burning contamination dots on the sample, which creates spots on the surface. The smaller the spot diameter, the more collimated is the beam. The area dose applied for this resist was between 80 - 110 $\mu C/cm^2$, according to a dose test that is previously done for optimization purposes (as the one in fig. 3.3), with a spot size around 15 nm.

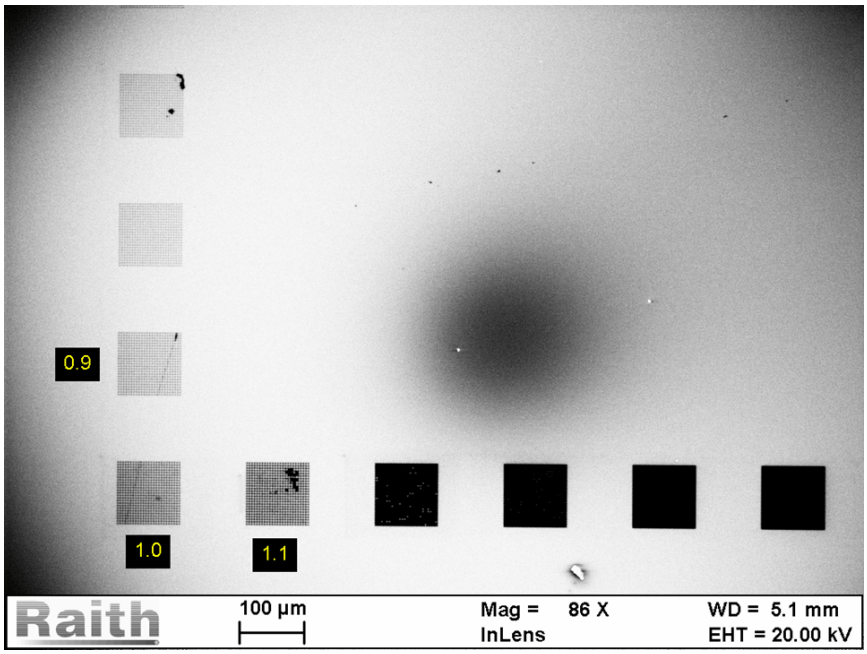

FIGURE 3.3: An example of an electron-beam lithography dose test with doses varying between 70 and 300 $\mu C/cm^2$.

After the exposition, the sample is developed in a 70% isopropyil alcohol and 30% deionized water solution for 60 seconds for dissolution of the e-beam exposed areas only. The desired metal is then deposited through a magnetron sputtering

technique, at a base pressure around 10^{-8} Torr and argon working pressure of 5 mTor.

In the final lift-off step, the sample is immersed in acetone for 3 minutes, followed by 15 seconds of ultrasonic bath, in order to dissolve all the remaining resist, leaving only the metallic areas that were attached directly to the substrate. The substrate is then cleaned with isopropyl alcohol followed by deionized water, and it is dried with an air flow so that no stains are left on the surface. The sample is then analyzed in an electron microscope in order to characterize its final size and roughness.

The electron-beam lithography with positive resist process is summarized below:

1. **Resist deposition**: ALLRESIST AR-P 672.045 950k PMMA resist is deposited on a SiO_2 substrate in a spin coater at 4000 rpm for 60 seconds, followed by 3 minutes in a hot plate at 150^o C.
2. **Exposition**: The pattern is exposed in a Raith e-LINE lithographic microscope at a 29 mm height, 30 μm aperture, 20 kV acceleration voltage and 100 μm writefield, with a previously optimized dose.
3. **Development**: the sample is submerged in a 70% isopropyil alcohol and 30% deionized water solution for 60 seconds.
4. **Metallization**: a thin-film metallic layer is deposited through magnetron sputtering with the desired thickness.
5. **Lift-off**: the sample is submerged in acetone for 3 minutes and placed in an ultrasonic bath for 15 seconds.

3.2.3 Magnetron Sputtering

Magnetron sputtering technique is used for thin-film metal deposition, in this thesis mainly Au, Permalloy ($Ni_{80}Fe_{20}$) and CoFeB. In a high vacuum main chamber, with a base pressure around 10^{-8} Torr, a negative potential is applied to the target metal whereas a positive bias is applied to the substrate, that is placed facing the target.

The chamber is then filled with a high purity inert gas, for instance Argon, with working pressure of 5 mTorr. As shown in fig. 3.4, the Argon is ionized in the presence of the electrical field and the gas ions are accelerated towards the target metal. The high energy molecular collisions that take place forces the negatively charged target metal atoms to be ejected into the plasma and those are accelerated to the positively charged substrate, forming a thin film coating above the sample.

In order to enhance the adherence between the metal and the substrate, a thin (usually less than 5 nm) buffer layer, titanium or tantalum for example, is deposited

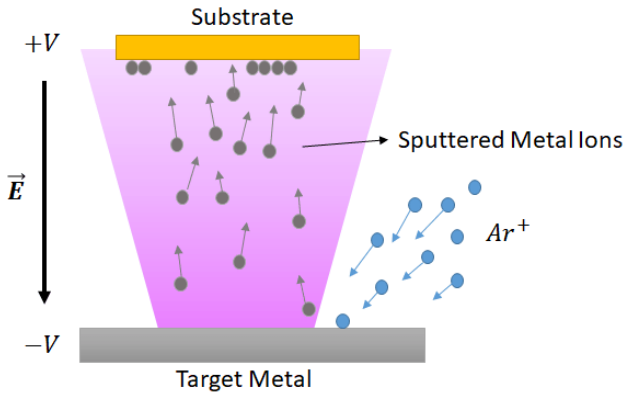

FIGURE 3.4: Schematic representation of plasma formation in magnetron sputtering. The ionized argon atoms hit the surface of the target metal, ejecting atoms that are accelerated towards the sample, that coats it.

before the target metal. On top of the metal, a thin capping layer is also deposited to avoid oxidation, as tantalum or ruthenium.

An AJA International magnetron sputtering, see fig. 3.5 , was employed in this thesis, with 6 guns, which are connected to 4 DC sources and 2 RF sources. A secondary load-lock chabber is used to exchange samples in order to always keep the main chamber at high vaccum. A Phase II J AJA software allows the control of the system, as deposition pressure and gas type, source current and power, deposition time and layer sequence.

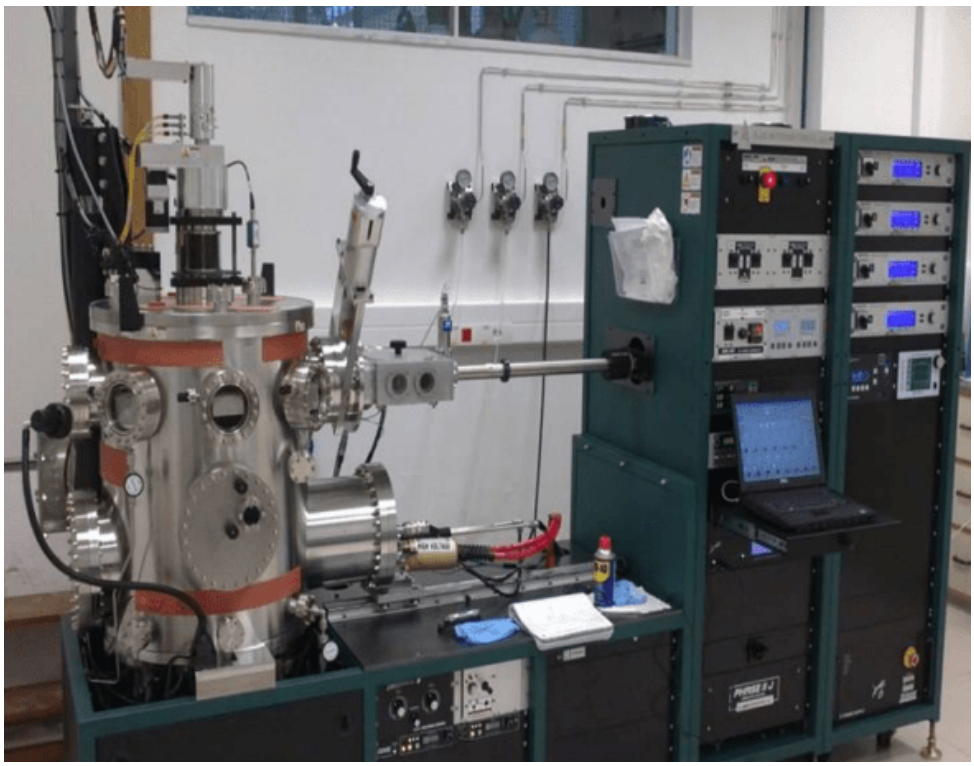

FIGURE 3.5: The AJA International magnetron sputtering used in this thesis, located at LABNANO/CBPF. Photo withdrawn from [48].

3.2.3.1 X-ray Reflectivity

To obtain a precise thickness control in magnetron sputtering, a calibration step is performed before any sample fabrication. For each target metal a thin film is deposited on a Si substrate for a certain amount of time. The film thickness is obtained by an X-Ray Reflectivity measurement.

A PANalytical X'Pert PRO X-Ray irradiates Cu Kα_1 X-rays with a 1.54056 Angstrom wavelength towards the surface of the film. Above the critical angle for total reflection (θ_C), the Fresnel reflection from the air/thin-film and the one from the thin-film/substrate interfaces interfere generating low-angle fringes, called Kiessig fringes, see fig. 3.6a.

The complex refractive index of the sample can be given by

$$\eta = 1 - \delta - i\beta \tag{3.5}$$

Bragg's law can be written for reflectivity, for a film with thickness t in the nth order as

$$n\lambda = 2t\ sin\theta \tag{3.6}$$

Considering the real part of the refractive index only, one can obtain:

$$sin^2\theta = \left(\frac{\lambda}{2t}\right)^2 n^2 + 2\delta \tag{3.7}$$

By plotting $sin^2\theta$ as a function of n, a quadratic function is found, in which the film thickness can be obtained from the n^2 coefficient, as shown in fig. 3.6b.

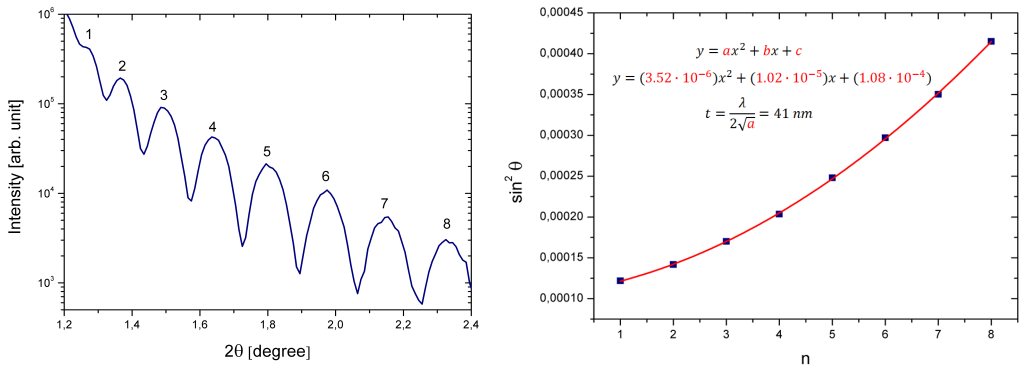

(A) (B)

FIGURE 3.6: The diffraction pattern in thin films (A) and the quadratic fitting (red line) for obtaining the film thickness (B).

3.3 SQUID Magnetometry

Superconducting **QU**antum **I**nterference **D**evice (SQUID) magnetometer is based on the interference between two superconducting Joseph junctions connected in parallel in a superconducting loop which is used for highly sensitive magnetic flux measurements.

The magnetic flux that passes through a superconducting loop is quantized in units of $\phi_0 = h/2e \approx 2.07 \times 10^{-15} Tm^2$. A superconducting current flows through the loop, with equal currents in each junction. Any magnetic flux change inside the coil will modify its induction, adding a current to one junction and subtracting from the other, due to Faraday's law.

As the superconducting current has a wave nature, a phase difference will appear between the Josephson junctions, resulting in a periodic variation of the resistance with the magnetic flux. Also, a periodic voltage drop will arise in the detection circuit, in which each voltage drop step corresponds to the passage of one flux quantum, allowing it to be a high sensitive fluxmeter [38].

A Magnetic Property Measurement System (MPMS) from Quantum Design was employed for magnetometry measurement through a vibrating sample magnetometry (VSM) technique. The system uses a superconducting magnet that can apply magnetic fields up to 7 T [49].

In the SQUID-VSM technique, the sample vibrates around the center of the detection coils at a fixed frequency ω, where the position can be described as $z(t) =$ B $sin(\omega t)$, where B is the amplitude of vibration. In each oscillation, there is a peak at the detection coils, and the signal can be described, as a function of time, as eq. 3.8, where A is a scaling factor that is proportional to the sample magnetic moment.

$$V(t) = AB^2\, sin^2(\omega t) = \frac{AB^2}{2}[1 - cos(2\omega t)] \tag{3.8}$$

A lock-in amplifier is then used to quantify and isolate the signal that occurs at a 2ω frequency, caused exclusively by the sample, for an appropriate choice of vibration frequency [49].

3.4 Magneto-Optic Kerr Effect (MOKE)

The magneto-optic Kerr effect (MOKE) describes the change in polarization when light is reflected by a magnetic medium. This effect is used for magnetometry measurements (MOKE magnetometry), as for magnetic domains observation (Kerr microscopy).

The first description of a magneto-optical phenomenon was done by Faraday, in 1845, in which he observed that a beam of polarized light changes its polarization angle when passing through a glass under the application of a magnetic field. This change in angle is proportional the magnitude of the field, this is known as magneto-optic Faraday effect. 32 years later, another magneto-optical effect was discovered by John Kerr. He realized that the polarized light undergoes a rotation after reflection from a polished magnetic material, later called Kerr effect [50].

The physical origin of the magneto-optic effects can be explained, in a classical manner, as the difference in movement exerted in the electrons of the material by the left- or right-circularly polarized light due to the Lorentz force. The linearly polarized light can be described as the superposition of two circularly polarized components, and the right(left) circularly polarized light will induce the motion of the electrons in a right(left) circular path, with radius proportional to their electric dipole moment [51].

In the absence of a field, both radii will be the same, so no net polarization rotation take place. When the magnetic field is applied, an additional force will be present, pointing toward from the center for one of the motions, and away for the other, thus one radius will be bigger than the other. Different dielectric constants for the right- and left- circularly polarized modes will take place and the reflected light will experience a polarization rotation [51]. The quantum mechanical spin-orbit interaction was necessary to explain the unusually large values of the magneto-optical effect in ferromagnetic materials, as it links the electron magnetic moment to its motion.

Three different geometries can be used to measure the magnetisation components, longitudinal (L-MOKE), polar (P-MOKE) and transversal (T-MOKE), depicted in fig. 3.7. While L- and T-MOKE are sensible to the rotation in the polarization plane, the P-MOKE is only sensible to intensity changes.

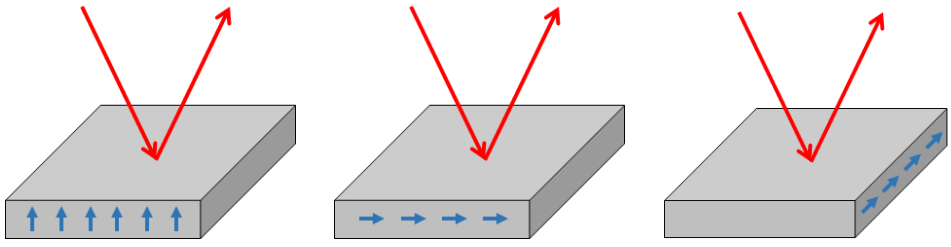

(A) P-MOKE (B) L-MOKE (C) T-MOKE

FIGURE 3.7: MOKE geometries: (A) Polar, (B) Longitudinal and (C) Transversal.

3.4.1 MOKE Magnetometry

The longitudinal geometry, L-MOKE, was employed in this thesis as a focused magnetometer. The experimental setup is shown in fig. 3.8. The monochromatic laser

light reached the sample surface linearly polarized in the y-direction due to the polarizer. The reflection will generate a small electric field in the perpendicular direction (x), due to the Kerr effect. Another polarizer, called analyzer, is placed between the sample and the photodiode, with a variable angle ϕ. The Kerr signal is related the Kerr rotation θ_K and also to the analyser angle, eq. 3.9 for a perfect polarizer.

$$\text{Kerr Signal} = \frac{2sin(2\theta_K)}{tan(\phi)} \tag{3.9}$$

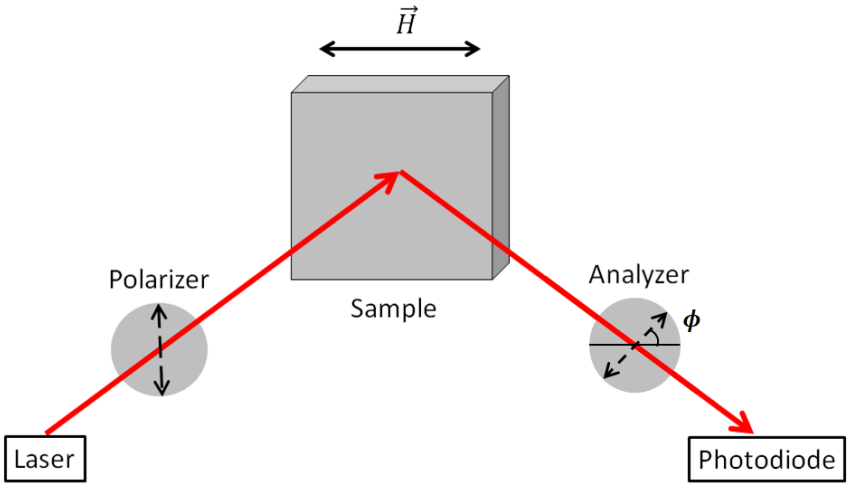

FIGURE 3.8: Focused magneto-optic Kerr effect magnetometry in the longitudinal geometry principle of operation.

A 635 nm and 3 mW laser beam is modulated in amplitude at a 50 kHz frequency, in order to allow a synchronous detection at the lock-in, fig. 3.9. The beam goes through the polarizer, followed by a beam splitter, which directs one splitted beam directly to the photodiode and the other to be reflected at the sample.

The sample is placed between the poles of a magnet that can reach up to 120 mT. Before the sample, an objetive lens allows the beam to be focused only in the desired area of the sample, which can be seen through an optical microscope. The beam, then, goes through the analyser and reaches the photodiode, that subtracts the intensity between the two splitted beams, thus transforming the light signal into an electrical signal that is sent to a lock-in amplifier, which can be seen through an oscilloscope.

A Hall sensor placed between the magnet, above the sample, is also connected to the oscilloscope, for magnetic field measurements, which allow the magnetization curves to be obtained in real time.

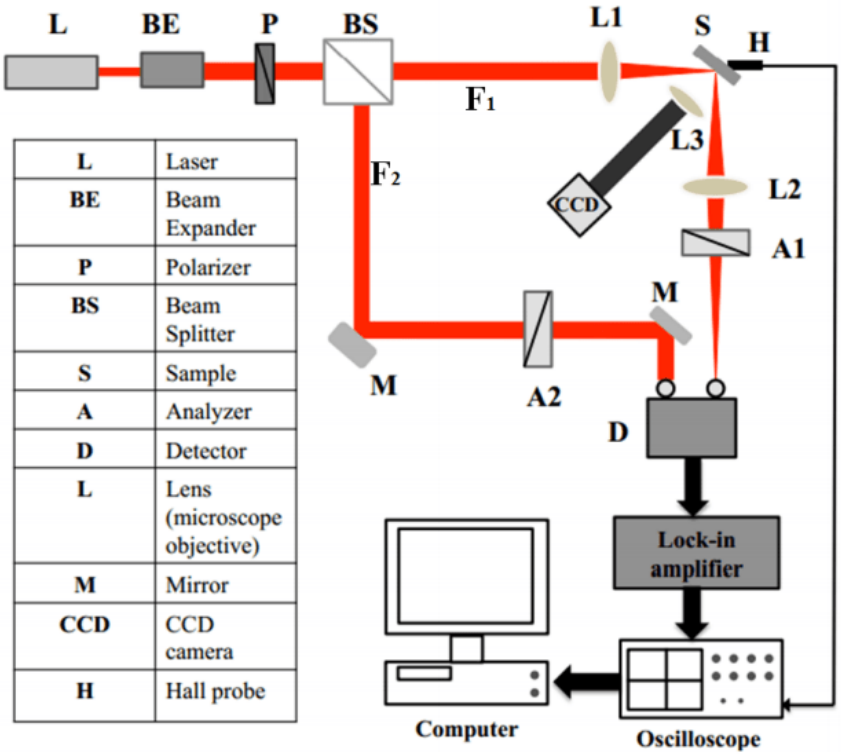

FIGURE 3.9: Focused magneto-optic Kerr effect magnetometry in the longitudinal geometry setup. Extracted from [48]

3.4.2 Kerr Microscopy

The Magneto-optic Kerr microscopy is a polarized light microscopy that allows a non-destructive observation of magnetic domains due to different rotation angles due to Kerr effect in different magnetization directions.

For two domains with opposite magnetization the amplitude of the reflected light will have opposite signs. We can decompose this reflected amplitude in the component of the initial polarization angle (A_N) and the effective Kerr amplitude (A_K). Then, $A = A_N \pm A_K$, where $\theta_K = A_K / A_N$ for small angles. If the analyser is placed at an angle $\phi = \theta_K$, then one domain will appear completely dark, whereas the other will have a small brightness [40].

For an analyser angle beyond θ_K the contrast, given by the differece in intensity between the dark and bright domains is given by eq. 3.10, which is linear with the Kerr amplitude, and therefore, linear with the magnetization [40].

$$I_2 - I_1 = 2sin(\phi) A_K A_N \tag{3.10}$$

3.5 Magnetic Force Microscopy

The magnetic force microscopy (MFM) is a variant of the atomic force microscopy (AFM) that scans a magnetic surface and records magnetostatic forces between the sample and the tip [40].

The AFM is based in the interaction force between a very sharp tip, that is mounted in a mechanical lever, the cantilever, and a surface (see fig. 3.10). As the tip gets closer of further way for the surface, attractive or respulsive forces due to atomic interactions take place, which can be described by the Lennard-Jones potential. As the tip scans the sample, the cantilever is deflected accordingly to the surface topography, thus creating a three-dimensional nanometric topographic map of the surface.

The tip scans the sample, and its topography is detected due to the cantilever deflections that happen due to atomic interactions, described by the Lennard-Jones potential. As the deflections are very small, an optical detection method is employed with a 4-quadrant photodiode.

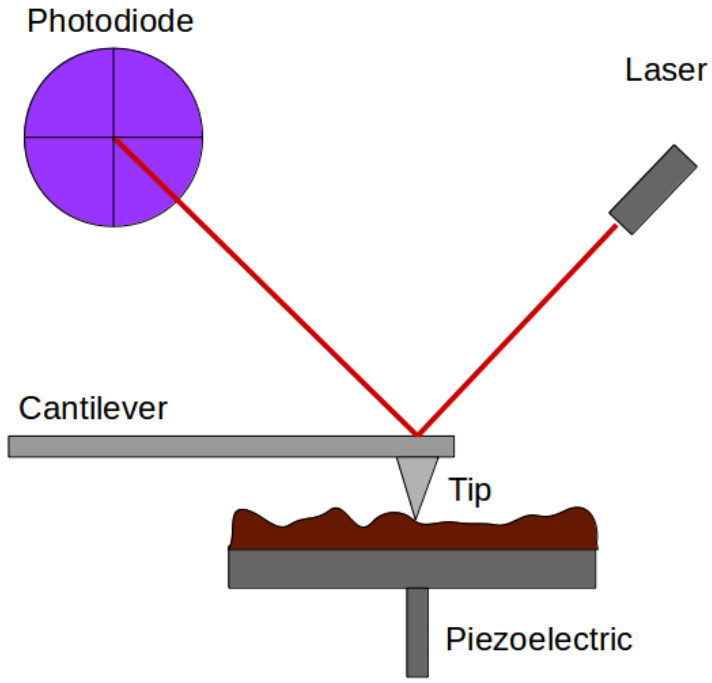

FIGURE 3.10: Atomic Force Microscopy (AFM) scheme. The interaction between the tip and the sample topography causes deflections in the cantilever that are optically detected at a photodiode. This allows the sample surface to be mapped.

Two main modes of operation are used for AFM imaging: contact (or static) and tapping (or AC, or intermittent) modes. In the contact mode, the tip touches the sample at a constant height, controlled by the feedback system. The z-deflection, made by a piezoelectric material, that is needed to keep a constant tip/sample distance is

equivalent to the sample's topography. In the tapping mode, the cantilever oscillates near it resonance frequency, and the feedback system keeps the amplitude constant. The interaction with the sample surface causes amplitude and phase changes, that are recorded and used to reconstruct the topography [40].

In the MFM, the tip has a hard magnet layer that is kept at a height in which the magnetostatic interaction dominates, tipically a few dozens of nanometers (e.g. 60 nm). The oscillation frequency of the cantilever, even in the tapping mode, is many orders of magnitude lower than the Larmour frequency of the electrons, so the magnetic configuration of the sample can be considered in equilibrium in every point. The force between the sample and the tip can be computed as the gradient of the interaction energy, $\vec{F} = -\nabla E_{int}$, which can be described by eq. 3.11, which offer information about the stray field of the sample, known the magnetization of the tip, or vice-versa [40].

$$E_{int} = -\int_{tip} \vec{M}_{tip} \cdot \vec{H}_{sample}\, \mathrm{dV} = -\int_{sample} \vec{M}_{sample} \cdot \vec{H}_{tip}\, \mathrm{dV} \tag{3.11}$$

Constrast in the MFM image can be generated by three main mechanisms: charge, susceptibility and hysteresis contrast. Charge contrast happens when the interaction between the sample and the hard magnet tip is weak enough so that no modification occurs in neither of them. The MFM image will be derived from the original charge distribution of the sample. The image should be inverted if the magnetization direction of the sample is in the oppostite direction.

When there is interaction between the sample and the probe, the hard magnet tip often causes reversible distortions in a soft magnet sample, which is the susceptibility contrast. The hysteresis contrast, caused by strong interactions, lead to irreversible changes, which are source for artifacts and distorted images, and should be avoided. This last limits the sensitivity and resolution of the technique [40].

The most common MFM imaging procedure is the so-called two-pass lift mode, in which the sample is first scanned in tapping mode, to obtain topographic information. Then, in a second pass, the tip is raised several nanometers above the sample, at a constant height, typically between 60-100 nm, accordingly with its topography, in order to detect only the magnetic interactions, through a force gradient detection by phase or frequency changes.

Chapter 4

Results and Discussion

4.1 Micromagnetic Simulations: Spin-Waves in Néel Walls

This section is aimed to investigate the nature of the spin-waves that can be excited within an infinite Néel wall and to describe their suitability for magnonic applications, by means of micromagnetic simulations.

We set a 10 μm x 1 μm x 5 nm permalloy rectangle, with periodic boundary conditions at the major length, divided in (4.88 x 3.9 x 5) nm^3 cells. These values were chosen so that the number of cells is a power or 2 in every direction (1024 x 256 x 1), which accelerates the computational time for the software.

To obtain the Néel wall, the system was split in three longitudinal regions: a 20 nm wide central region, with magnetization along the +y direction, and the other two, below and above this central one, with +x and -x magnetization, respectively. The system was then allowed to relax until reaching a minimum energy configuration shown in fig. 4.1a.

The magnetization rotates in a counterclockwise direction from a +x at the bottom domain to a -x magnetization in the top domain, and the Néel wall is the center of this transition, where the magnetization is in the +y direction. Fig. 4.1b shows the x-magnetization as a function of the y-component, which changes from a +1 to a -1 direction.

The magnetostatic field generated by this magnetization state across the rectangle width (y-direction) is shown in fig. 4.1c. At both edges, narrow peaks can be seen as a consequence of the minimization of the magnetostatic energy at borders.

A main peak is found at the center, as magnetic charges ($\nabla \cdot \vec{M}$) arise from the magnetization rotation from one domain to the other. The center of the peak corresponds to the Néel wall center, and its width at half maximum, to the wall width, measured to be 74 nm.

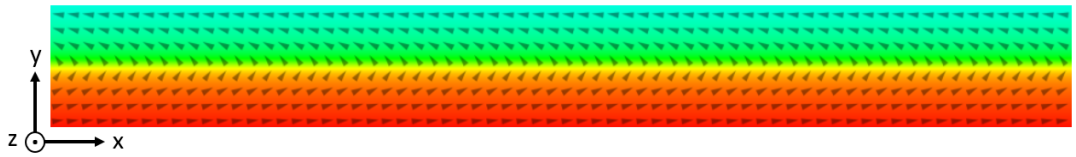

(A) Néel wall in 10 μm x 1 μm x 5 nm permalloy rectangle with periodic boundary conditions at the x-direction.

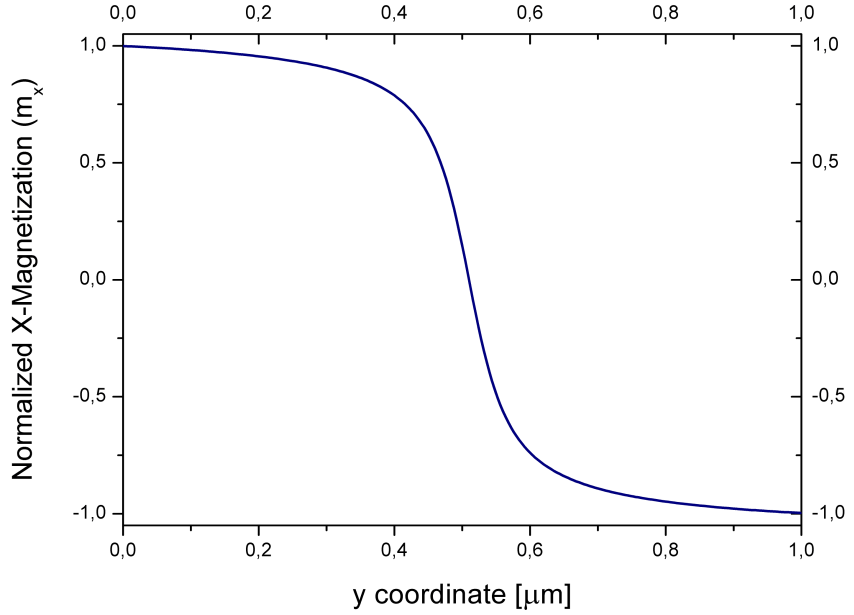

(B) The normalized x-component of its magnetization

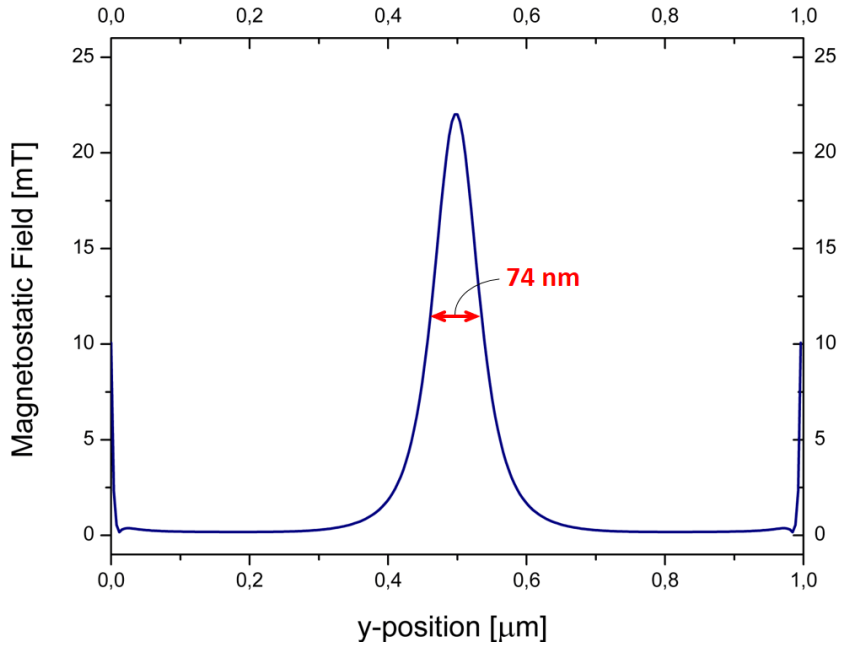

(C) The magnetostatic field intensity across a transverse cross-section (y-direction), in which the 74 nm Néel wall width was estimated by its width at half maximum.

FIGURE 4.1: Mumax3 Simulations: Néel wall with longitudinal periodic boundary conditions.

In order to excite spin-waves, a 1 μm x 20 nm x 5 nm region was defined transversely at the center of the structure (antenna, in fig. 4.2a). An out-of-plane sinc-function pulse was applied in that region, with 100 mT intensity and 40 GHz cut-off frequency (eq. 4.1), and we allowed the wave to spread all over the structure until the magnetization returned to equilibrium. The z-component of the magnetization was Fourier-transformed in two different regions as shown in fig. 4.2a: inside the domain wall (Region 1), and in one of the uniform domains (Region 2).

$$\mu_0 H_z = 100\ mT\ \frac{sin[2\pi\ (40GHz)]}{2\pi\ (40GHz)} \tag{4.1}$$

The resulting spectrum can be seen in fig. 4.2b. Up to 2.2 GHz the excitation is mainly inside the Néel wall (Region 1) which is an indication that the spin waves are confined to the wall width. At 2.5 GHz the first peak inside the domain can be seen, and, above that frequency, the magnetization main peaks are coincident inside and outside the domain wall.

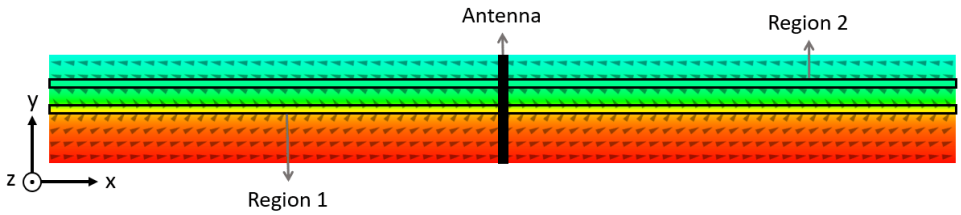

(A) The region of excitation (Antenna) and the two regions in which the z-magnetization was saved: within the Néel wall (Region 1) and within the domain (Region 2).

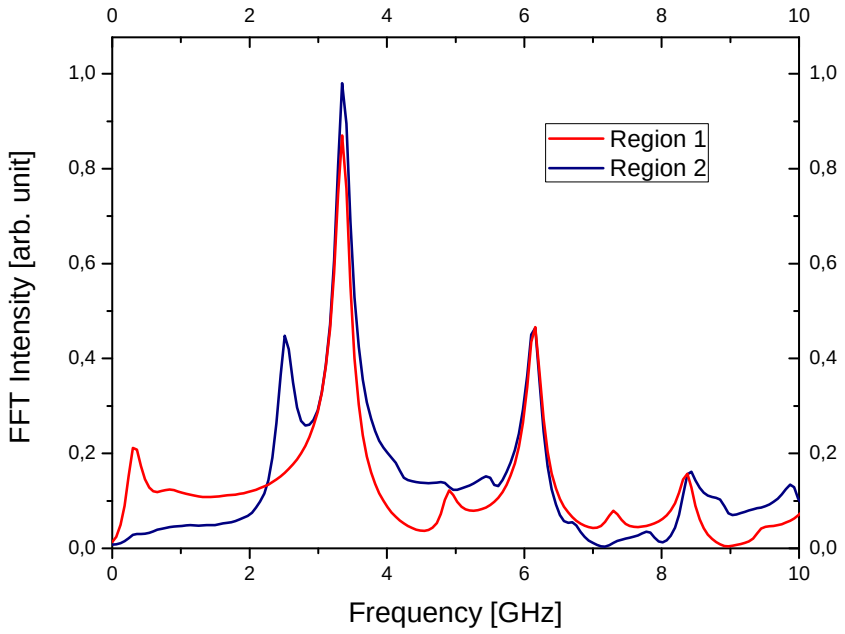

(B) Fourier transform intensity of z-magnetization of both regions.

FIGURE 4.2: Mumax3 Simulations: An out-of-plane sinc pulse was applied at the antenna and the time evolution of the z-component of the magnetization was saved and Fourier transformed.

To further investigate the propagation, a sinusoidal pulse was applied in the antenna in certain frequencies and let run until reaching a steady state, and then, the magnetization was saved as a function of time. Fig. 4.3 shows the z-component of the magnetization for several excitation frequencies.

Well defined wave-vectors can be seen within the wall, which is a necessary precondition for many magnonic applications in information transmission and processing that rely in wave interference [32]. Also, it can be seen that the spin-waves are actually confined to the Néel wall at low frequencies and that it starts to spread to the domains as the frequency increases. For frequencies above 3 GHz, complex interference patterns start to arise due to wave reflection at the borders.

The z-component of the magnetization was obtained, for a fixed x-position, as a function of the y-coordinate for two different frequencies, see fig. 4.4. For the 1 GHz excitation, a peak at the wall region is readily seen, with a 100 nm width at half-maximum, which is slightly larger than the 74 nm wall width. On the other hand, for the 4 GHz excitation, an important part of the excitation is in the uniform domain region, and for 6 GHz the confinement effect is completely lost.

To quantify the dispersion of the waves confined within the Néel wall width only, a 100 mT sinusoidal out-of-plane pulse was again applied, this time restricted at a 20 nm circular region at the center of the structure to avoid wave reflection at the borders.

Frequencies ranging from 0.5 to 4 GHz were applied, and the z-magnetization was saved after a steady state was reached. From the images, the wavelength was extracted for each frequency. The dispersion relation, frequency vs. wavenumber ($k = 2\pi/\lambda$), was then obtained for frequencies up to 3.2 GHz, as shown in fig. **??**.

For frequencies above 3.2 GHz, the modes are predominantly in the uniform domains, which is not in the scope of this study. As the excitation is done at the center of the rectangle, our wavelength measurement is limited half of its length, 5 μm, that corresponds to k = 1.3 μm^{-1}. All wavenumbers below that were determined by curve fitting, and have a high uncertainty associated.

There was no difference in wavelength for the waves propagating in the +x and -x directions, which is an indication of the reciprocity for spin-wave propagation within the wall [33]. Even though the spin-waves are restricted to the nano-sized Néel wall width, the dispersion relation (fig. **??**) is non-quadratic and it is in the low wave vector range, showing that it is in the magnetostatic regime, as discussed in section 2.6.1 and not in the exchange regime. This is a result of the dipolar energy being the main energy responsible to domain formation, and the stray field being at its maximum at the domain wall width center.

As the wall is in the y-direction and the wave vector in the x-direction, the system is in the Damon-Eshbach geometry ($\vec{M} \perp \vec{k}$), which generate magnetostatic

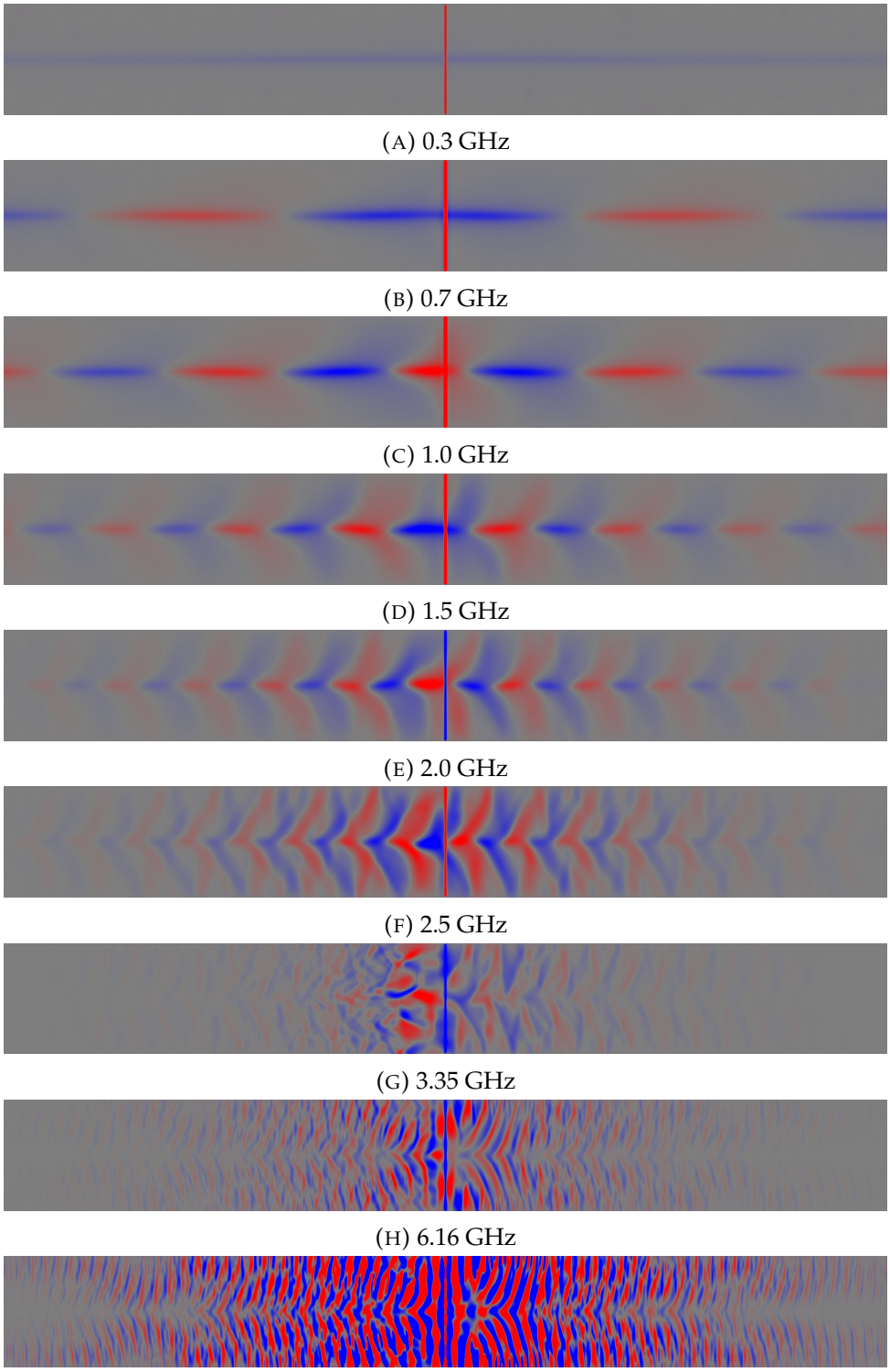

(A) 0.3 GHz

(B) 0.7 GHz

(C) 1.0 GHz

(D) 1.5 GHz

(E) 2.0 GHz

(F) 2.5 GHz

(G) 3.35 GHz

(H) 6.16 GHz

(I) 7.3 GHz

FIGURE 4.3: Mumax3 Simulations: The out-of-plane magnetization configuration due to a sinusoidal excitation at a 20 nm thick antenna at the center in several frequencies. The blue and red colors are for +z and -z magnetization, respectively.

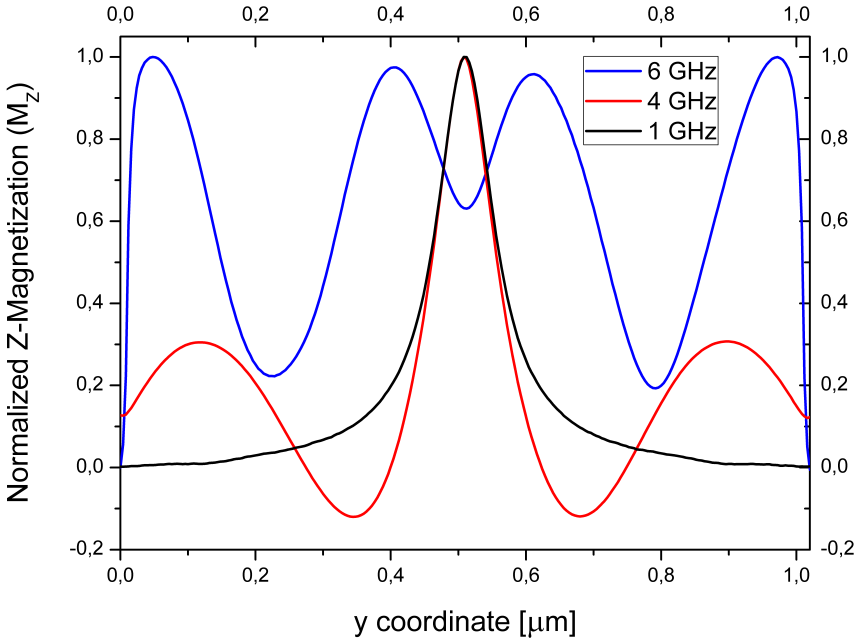

FIGURE 4.4: Mumax3 Simulations: The z-magnetization across the y-direction for a fixed x-position for 1 GHz, 4 GHz and 6 GHz sinusoidal excitations.

forward surface spin-waves. Therefore, as expected, a positive dispersion, in which phase and group velocities point at the same direction, was obtained, which is also a basic precondition for several magnonic device concepts [18, 52].

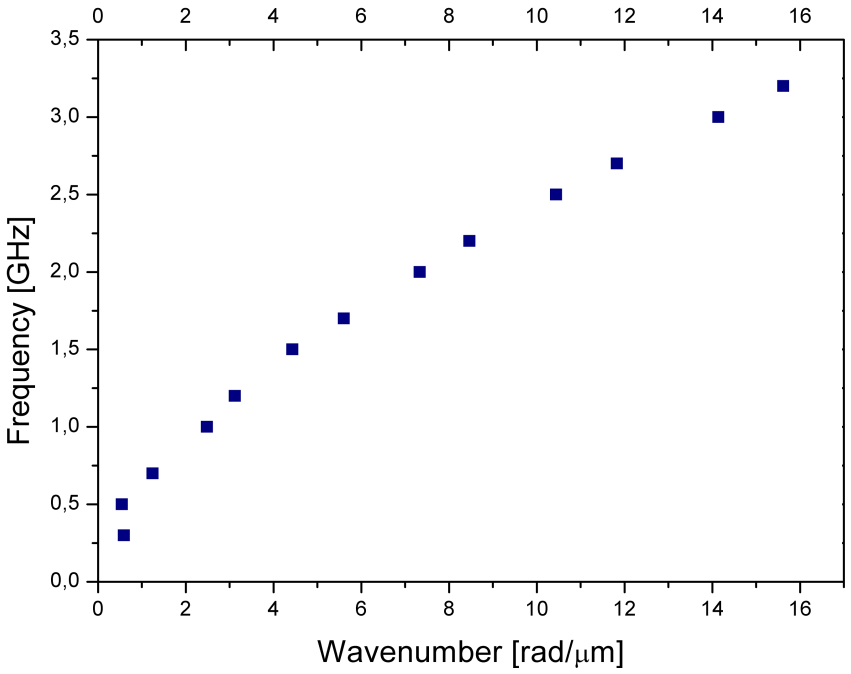

FIGURE 4.5: Mumax3 Simulations: Dispersion relation for the spin waves confined within a Néel wall in a 10 μm x 1 μm x 5 nm permalloy rectangle with longitudinal periodic boundary conditions, excited at a 20 nm dot at the wall center.

However, the equation for magnetostatic forward spin-wave modes in an infinite thin film, eq. 2.56, did not fit well for this case, which has no bias external

field. This is an indication that the physical model is not complete for this scenario, and several other factors should be taken in account for obtaining an appropriate analytical expression.

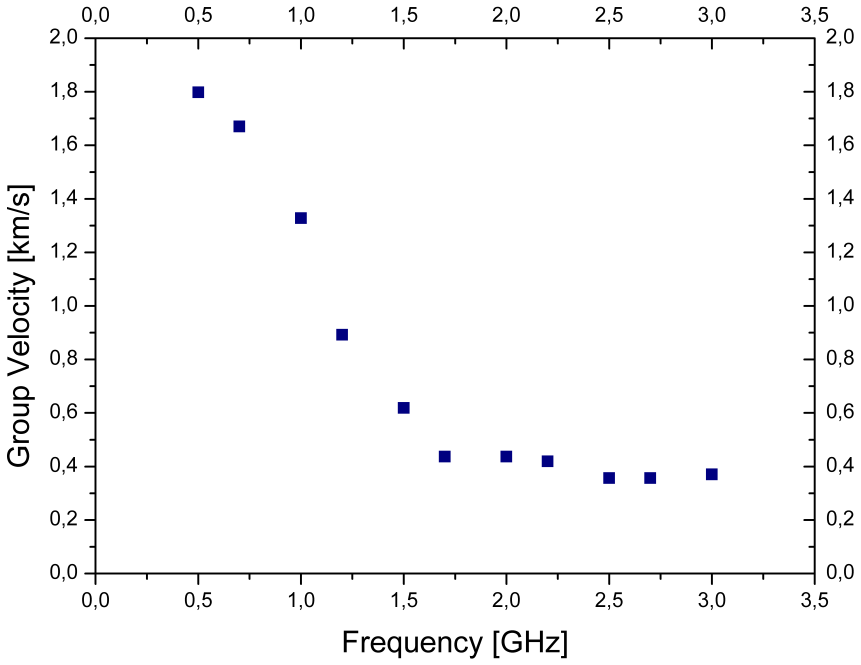

(A)

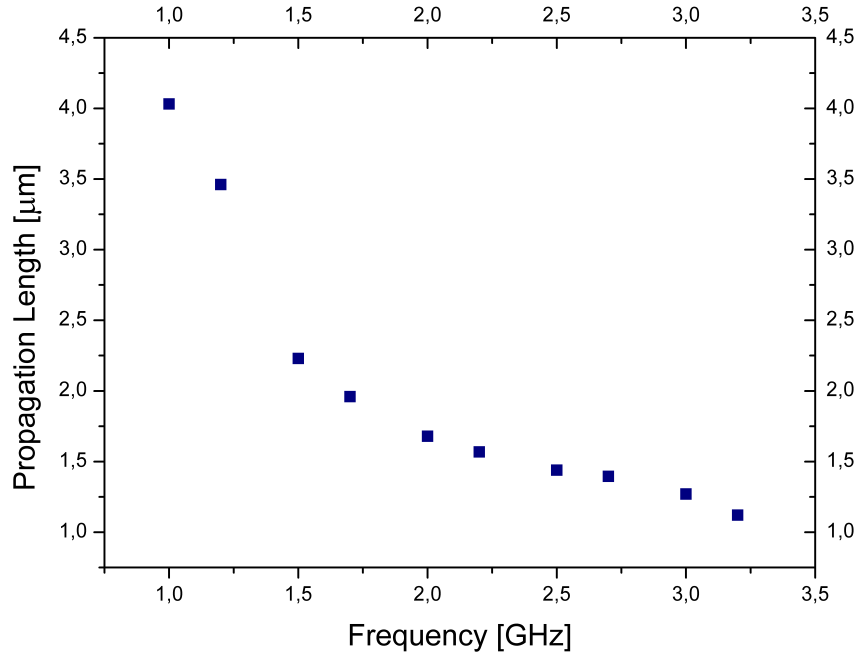

(B)

FIGURE 4.6: Mumax3 Simulations: Group velocity (A) and propagation length (B) of the confined spin-waves as a function of frequency.

Another important feature is the group velocity of these waves, fig. 4.6a, that was obtained by the derivative of the dispersion curve, according to the expression

$v_g = 2\pi\,(\partial f / \partial k)$. The group velocity can exceed 1 km/s at frequencies below 1 GHz, which is an important feature for high speed data transporting and processing.

From the images of fig. 4.3 it can be seen that, the higher the frequency, the faster the field amplitude is attenuated. The peak of the curves were fitted in a $y = y_0\, e^{-x/x_0}$ manner, in which x_0 is the propagation length, the distance in which the the magnetization amplitude decreases to $1/e$ of the initial value. The propagation length as a function of the frequency is shown in fig. 4.6b. It has values between 1 and 4 μm, which is in the acceptable range for integrated magnonic circuits [6, 9].

One of the main features of the domain wall as a spin-wave propagation path is its flexibility when compared geometrically confined waveguides. The position of the domain wall in the y direction can be readily controlled through the application of an external magnetic field, fig. 4.7a (top). We applied a longitudinal magnetic field and allowed the system to relax. After that, a 1 GHz out-of-plane sinusoidal excitation was applied in an antenna at the center, fig. 4.7a (bottom). The wave intensity across the minor length is shown in fig. 4.7b.

As the field is applied, one of the domains grows and the other shrinks, and, as a consequence, the domain wall is dislocated either up or down. Small fields, in the 10^{-4} T order of magnitude, are needed for such displacements. The wall shift as a function of the applied field follows a non-linear fashion, see fig. 4.7c. As it gets closer to the edge, more field is needed to displace the wall, and at 7 mT, it is completely expelled from the structure.

Hence, spin-wave propagation in Néel walls presents well-defined wavevectors, which allow the propagation of information along its length, along with a nano-sized lateral confinement in the low-GHz range. Also, the wall shows mobility under the application of external magnetic fields, which is a very useful tool for flexible magnonic devices. However, the Néel wall is naturally found in Landau-states in magnetic nanostructures, which include more features than the model studied here, and it will be examined in the next section.

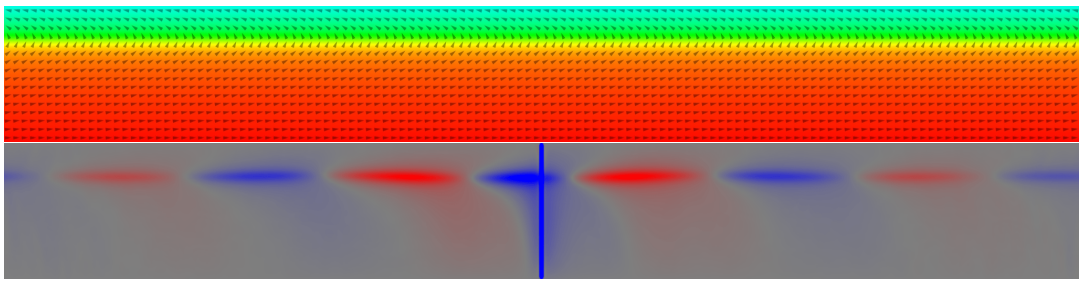

(A) The stable state under a 0.5 mT longitudinal field (top) and a 1 GHz spin-wave propagation in it (bottom).

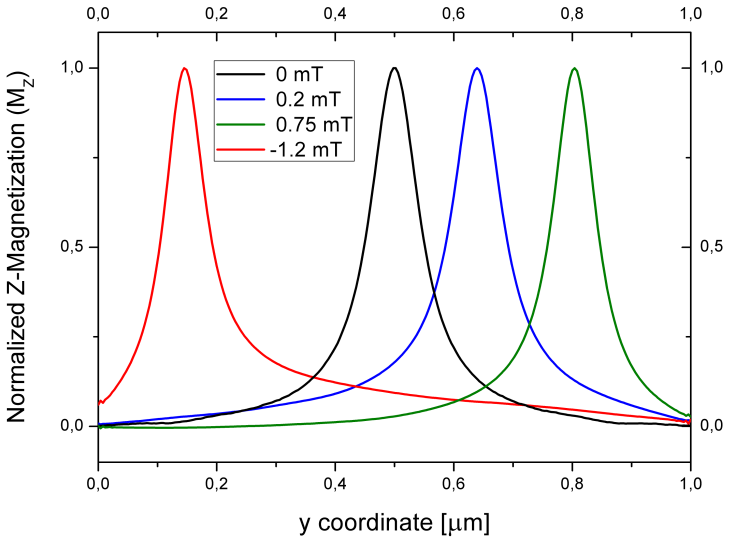

(B) The normalized spin wave intensity across the minor length (y-axis) for a 1 GHz sinusoidal excitation with the application of a static longitudinal field (x-direction).

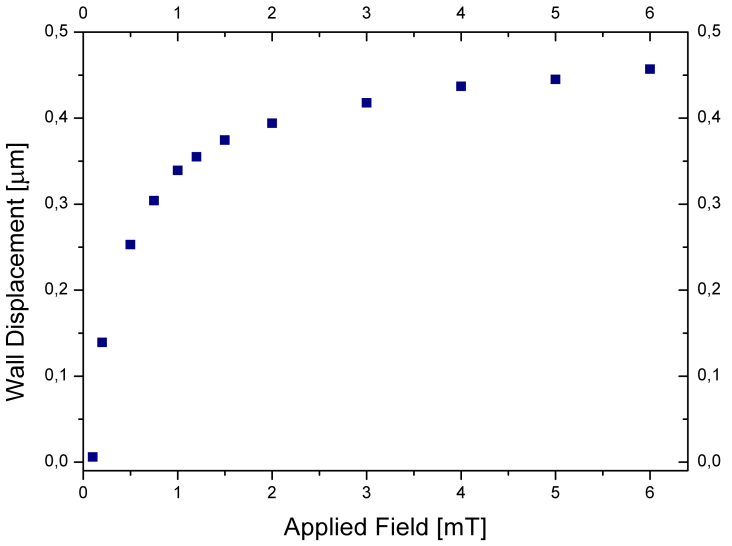

(C) The Néel wall dislocation in the y-direction as a function of the static longitudinal field.

FIGURE 4.7: Mumax3 Simulations: Néel wall displacement due to a transverse bias magnetic field.

4.2 Micromagnetic Simulations: Spin-Waves in Landau Domain States

This section aims to evaluate, through micromagnetic simulations, the spin-wave propagation within a Néel domain wall of a Landau domain state in a permalloy rectangle.

Experimentally, 180^o magnetic Néel walls are found in Landau flux-closure domain structures, as discussed in section 2.5, which can be found in permalloy rectangular nanostructures due to shape anisotropy. Different from the previously examined wall, in this case, the Néel wall has a finite length, with two 90^o walls in each of its ends. Also a vortex is present in its center, which divides the wall in two oppositely magnetized unidimensional regions, see fig. 4.8.

A 5 μm x 1 μm x 5 nm permalloy rectangle was chosen, as a proof-of-concept, in order to allow correlations with the first article to propose this propagation [32]. The sample was divided in (1024 x 256 x 1) rectangular (4.88 nm x 3.9 nm x 5 nm) nm^3 cells.

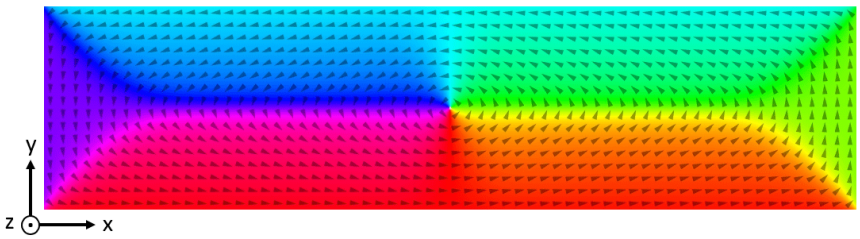

FIGURE 4.8: Landau-domain in a 5 μm x 1 μm permalloy rectangle, obtained by setting an initial vortex state and allowing the system to relax.

By starting with a random magnetization and allowing the sample to relax, three final magnetic structures would randomly appear: uniform, Landau and diamond states. This unreproducibility lead to question of whether the Landau state would actually be the minimum energy configuration for this size and shape. This will be discussed in section 4.3. Finally, the Landau-state was reproducibly achieved by setting an initial vortex state and allowing the system to relax (fig. 4.8).

Just like in the infinite Néel wall case (section 4.1), the wall can be moved in the y-direction trough the application of a longitudinal external field. Besides, in the Landau-state, another degree of freedom comes up: the vortex position in the x-direction can be changed through the application of a transverse magnetic field, see fig. 4.9a.

The vortex displacement as a function of the applied field in the y-direction is shown in fig. 4.9b. As it approaches the edge, a more intense field is necessary for dislocations, until a 9 mT field, in which the vortex is expelled from the structure. However, as the vortex dislocates from the center, the Néel wall gets wider, which

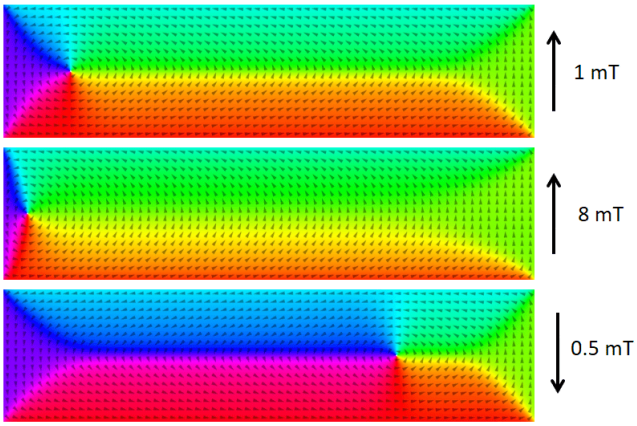

(A) The magnetic ground state when under an external transverse magnetic field.

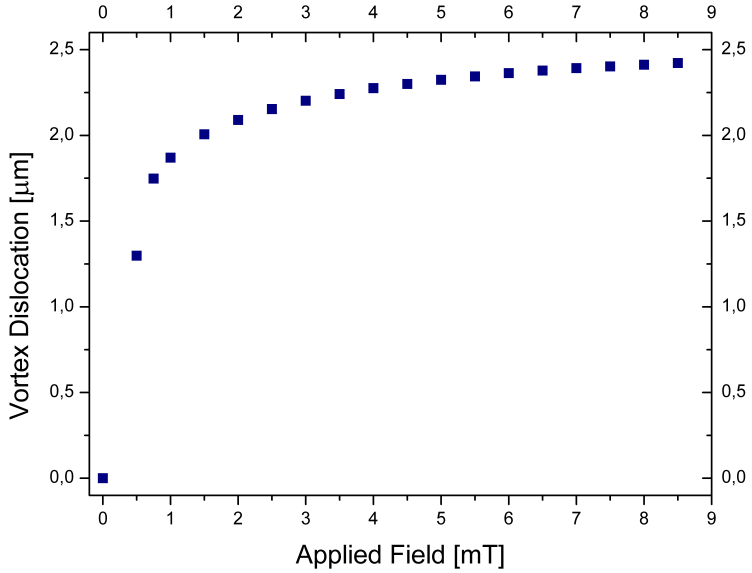

(B) The vortex position as a function of the external transverse field.

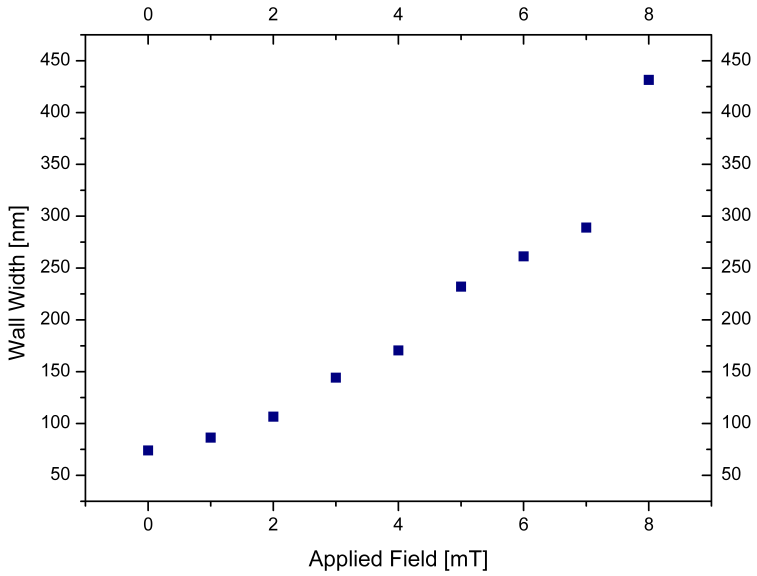

(C) Néel wall width as a function of the external transverse field.

FIGURE 4.9: Mumax3 Simulations.

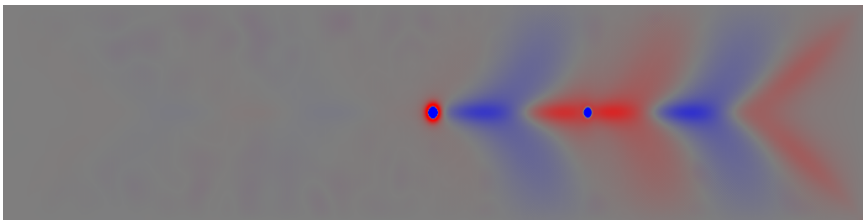

(A) 2 GHz sinusoidal excitation.

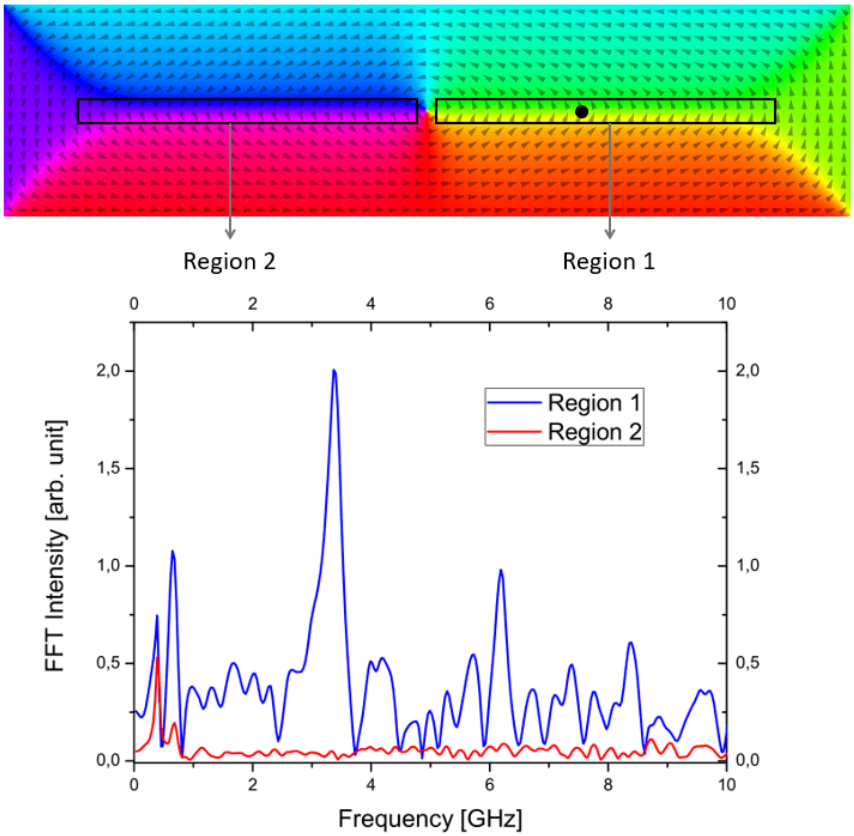

(B) The FFT of the z-component of the magnetization after a sinc excitation in a 20 nm circle (black dot) in two regions: at the same side of the excitation (Region 1) and at the other side (Region 2), after the vortex.

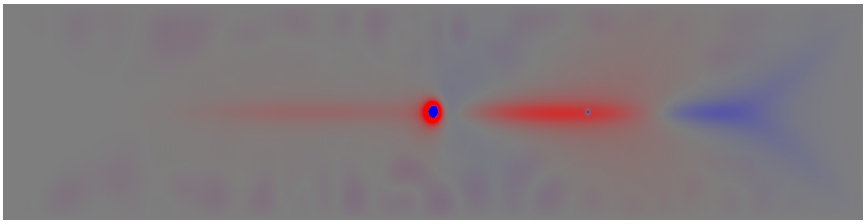

(C) 380 MHz sinusoidal excitation.

FIGURE 4.10: Spin waves excited at one side of the Néel wall only pass through the vortex in specific frequencies.

is shown in fig. 4.9c, calculated as the width at half maximum of the magnetostatic field in the y-direction. It goes from the 74 nm width, at zero-field, to a 431 nm at 8 mT. So, the higher the transverse field, the less confined the spin-waves within the wall will be.

As the Néel wall is separated in two by the vortex, with a +y magnetization at the right side and a -y at the left, when trying to propagate spin-wave within the wall, one has to decide in which one of the sides the excitation will take place. As an example, we performed a 2 GHz sinusoidal excitation inside a 20 nm circle at the right side of the wall, see fig. 4.10a. The vortex acts as a barrier, obstructing the wave propagation, thus limiting it to the +y side of the wall.

This is better shown by a sinc excitation performed at a 20 nm circle, 900 nm to the right from the vortex, followed by a Fourier transform of the z-magnetization in two different regions inside the wall: at the right (Region 1) and at the left (Region 2), see fig. 4.10b. Only at the side of the excitation (Region 1) we find non-zero FFT intensity profiles. The exceptions are 380 and 660 MHz, fig. 4.10c, which are the only frequencies that wave is able to overcome the vortex, hence the vortex acts as a frequency filter.

In order to have a long Néel wall without obstacles for the spin wave propagation, we applied a small static 1 mT magnetic field in the minor length direction of the rectangle with a Landau-domain magnetization. This results in a new equilibrium position to the vortex, closer to the left edge of the rectangle, fig. 4.11.

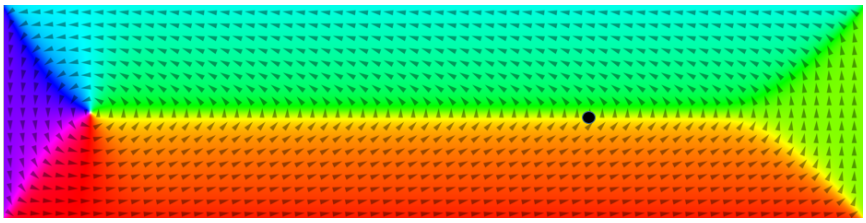

FIGURE 4.11: The equilibrium state of a Landau-domain structure in a 1 μm x 5 μm rectangle with a 1 mT static field in the minor length direction. The black dot shows the position where an out-of-plane pulse was applied.

We excite the Néel wall normal modes through a continuous out-of-plane sinusoidal pulse, with 1 mT amplitude, at a 20 nm circle located at the wall, 900 nm to the right from the sample center, shown by the black dot in fig. 4.11. Several frequencies were applied from 0.5 to 4 GHz, and after a steady state was achieved, the magnetization was saved as a function of time. The z-component of the magnetization for several frequencies is shown in fig. 4.12.

Just like in the infinite Néel wall (section 2.5), the spin-waves have a well-defined wavelength and are confined within the domain wall in frequencies up to around 2.4 GHz. They start to spread to the uniform domains above that, and a

(A) 0.5 GHz

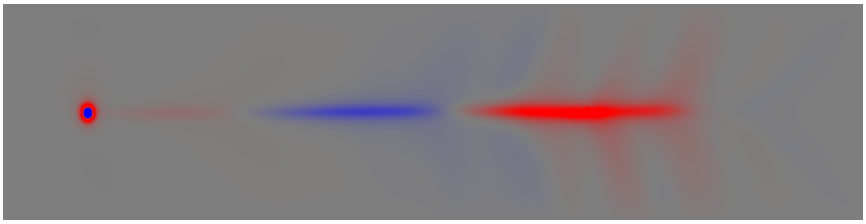

(B) 1.2 GHz

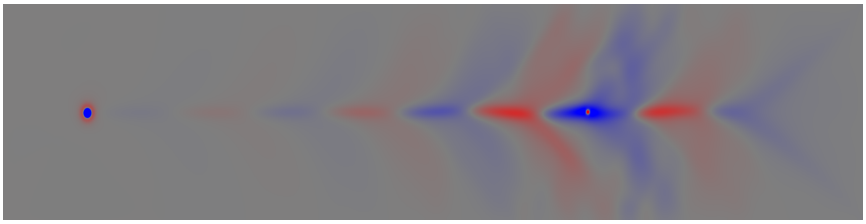

(C) 2.4 GHz

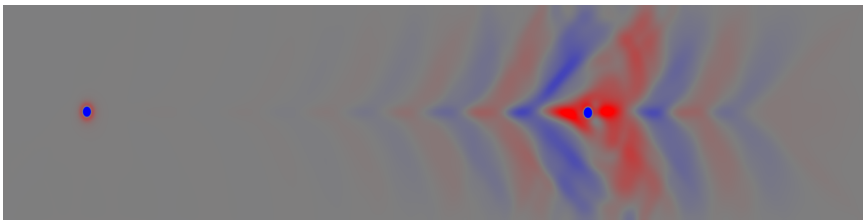

(D) 3.3 GHz

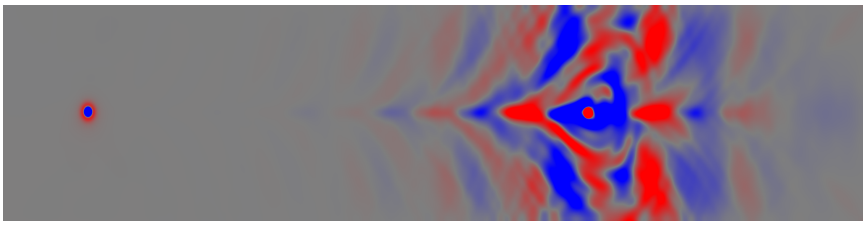

(E) 4.6 GHz

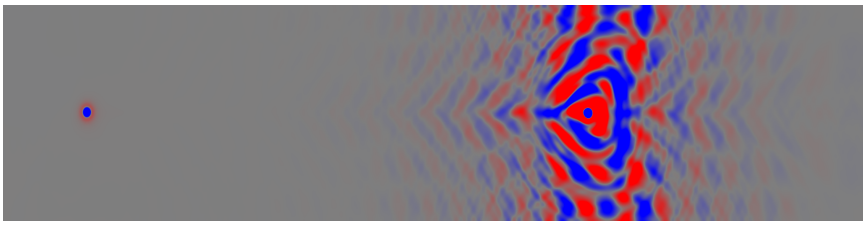

(F) 8.0 GHz

FIGURE 4.12: Ferromagnetic resonance eigenmodes for an out-of plane excitation within the Néel wall. The blue and red colors are for out-of-plane magnetization: +z and -z respectively.

series of reflections take place, resulting in a complex interference pattern, such as the one in fig. 4.12f.

The z-component of the magnetization, along the middle line of the rectangle (line in fig.4.13 top) was mapped as a function of the x-position, fig.4.13 is an example. From that graph, we can extract the corresponding wavelength (λ) for each of the frequencies. One thing to be pointed out is that the spin-wave intensity generated in response to the excitation pulse is orders of magnitude lower than the vortex z-magnetization. So, in fig. 4.13, a high peak can be seen at the left edge of the rectangle, which is the vortex, and its magnetization is almost not changed by the pulse.

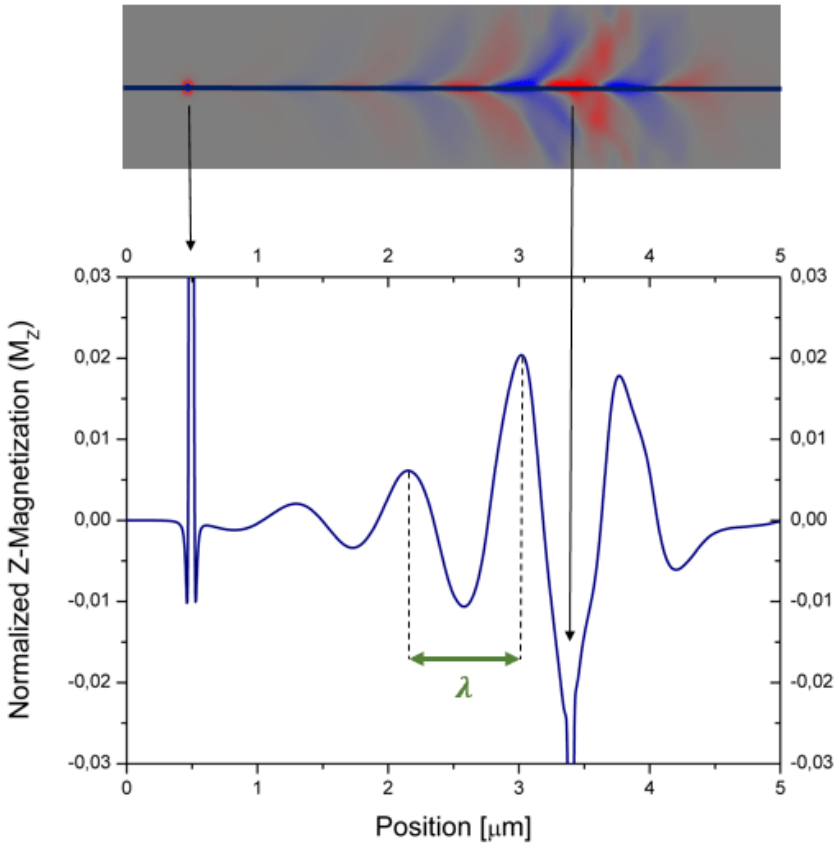

FIGURE 4.13: The out-of-plane magnetization across the line in the top picture as a function of the position for a 2.4 GHz excitation. The arrows show the position of the vortex (left peak) and the sine-excitation circle (right peak) in the graph. In between these two features it is possible to extract the corresponding wavelength (λ).

The dispersion relation for the Néel wall confined spin waves is shown in fig. 4.14. Here, just like in section 4.1, it is qualitatively very similar to the Damon-Eschbach forward surface spin-wave modes, with phase and group velocities pointing at the same direction, and at the magnetostatic regime.

In fact, the dispersion curve from the infinite wall (section 4.1) and for the wall in the Landau domain completely overlap, see fig. 4.15, which shows that propagation characteristics of the waves are much more controlled by the wall itself than

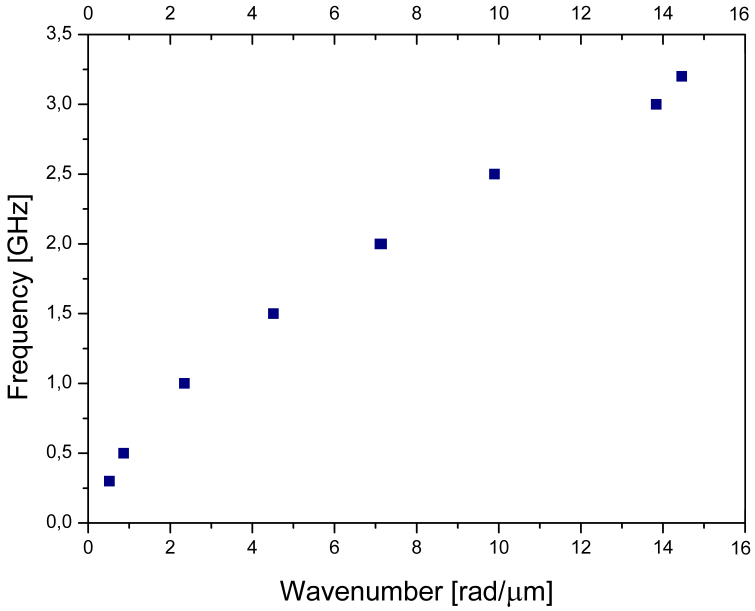

FIGURE 4.14: The dispersion relation of propagating spin-waves excited in a 20 nm dot within the Néel wall of a 5 μm x 1 μm x 5 nm permalloy rectangle.

to the sample dimensions. For instance, in an experimental scenario, the Néel wall does not necessarily need to be in a rectangle, but any shape or size, which allows a flexibility in the design for a magnonic device.

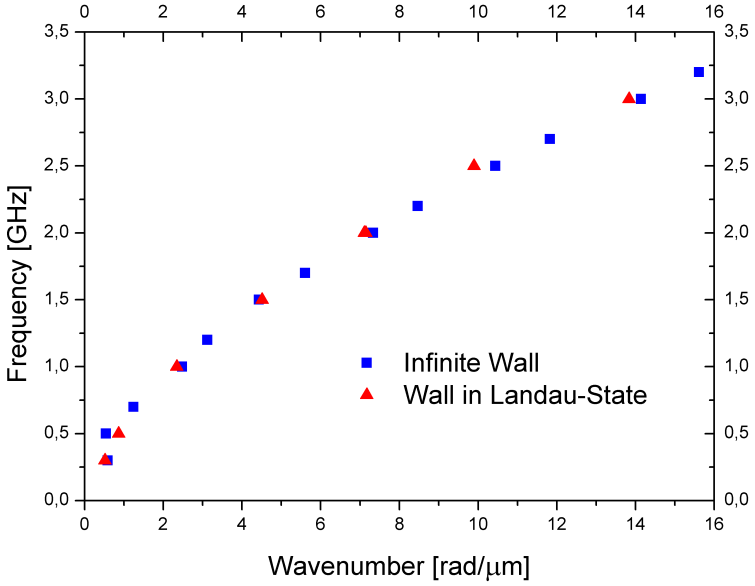

FIGURE 4.15: Comparasion between the dispersion relation in an infinite Néel wall (with longitudinal periodic boundary conditions) and in a finite wall in a Landau state.

4.3 Micromagnetic Simulations: Magnetic Ground-State in Permalloy Rectangles

This section aims to find the lower energy magnetic state of permalloy rectangles for different lengths and aspect ratios, through micromagnetic simulations.

Even though the Landau state could be created in our micromagnetic simulation in a 5x1 μm^2 permalloy rectangle, many difficulties arose from that, as irreversible transitions to uniform or diamond configurations happened in some scenarios. This lead to the question if we were actually dealing with a lower energy state.

We want to investigate the minimum energy structure in a permalloy rectangle by comparing the total energy for the three main possible magnetic configurations: uniform, Landau-domain and diamond state. By uniform, it can be either a C- or S-state, as they are almost degenerate, but not a flower state, as it only appears as a lower energy state in relatively high magnetic field conditions.

For that purpose, an energy minimization through the *relax()* command was applied under different initial conditions, an uniform magnetization for the S- or C- states, fig. 4.16(a). For Landau-domain state, an initial vortex magnetic state is placed at the center of the structure, fig. 4.16(b). For the diamond state, two four vortices, with same polarization but alternate opposite circulations, are placed side by side inside the structure, fig. 4.16(c). A random noise is added to all the initial conditions before relaxation.

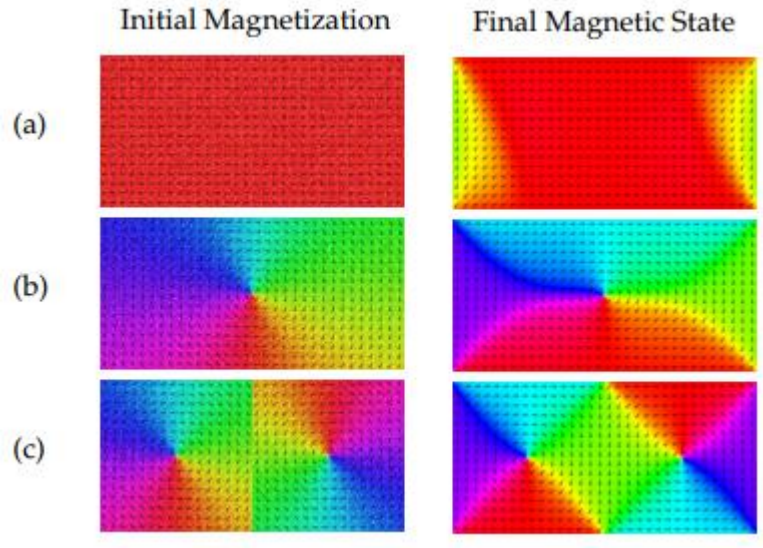

FIGURE 4.16: The initial condition, left column, and the magnetization state after relaxation, right column (a) Uniform State. (b) Landau Flux-Closure State. (c) Diamond State.

As permalloy has a negligible magnetocrystalline anisotropy, the total energy is the sum of the exchange and magnetostatic energies. The thicknesses have been

fixed to 5 nm. The samples were divided in cells with lengths equal or smaller than 5 nm. We have first measured the energy for a rectangle with one length fixed at 1 μm as a function of the other length, in order to evaluate the role of the aspect ratio, see fig. 4.17. Three main regions of lower energy configurations are highlighted: A (uniform), B(Landau) and C (uniform).

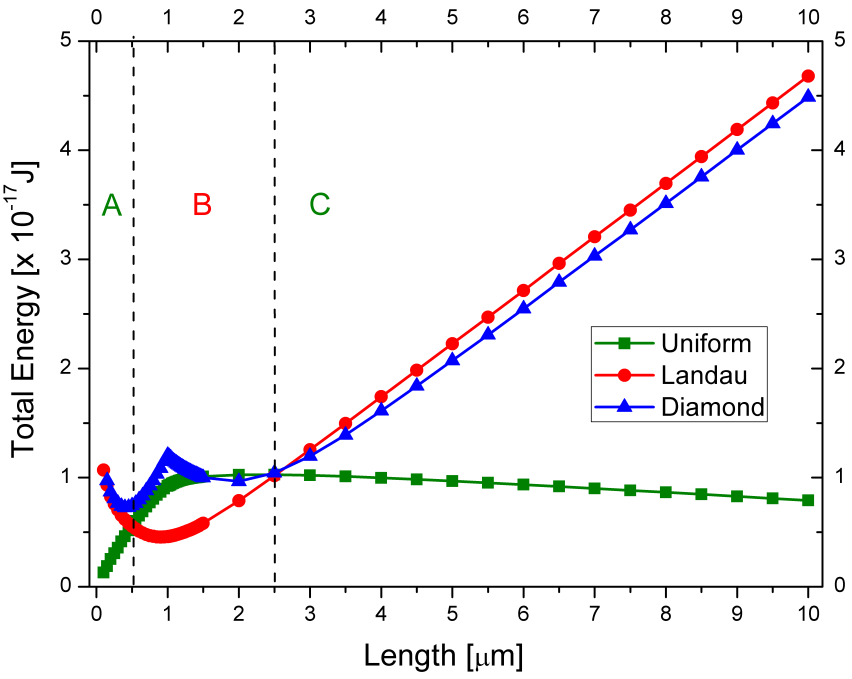

FIGURE 4.17: The total energy for a 1 μm x L μm x 5 nm permalloy rectangle as a function of L. Three regions can be identified: A and C, where the ground state is a uniform state, and B, where it is the Landau-state.

Regions A and C correspond to high aspect ratios, this lowers the dipolar field, as the opposite magnetic charges are relatively far away from each other. As a consequence, the magnetostatic energy becomes negligible compared to the exchange interaction, allowing the formation of S- or C- uniform states. As the length increases, above 600 nm, the Landau-domain structure becomes the ground-state. The magnetostatic energy becomes significant and the size of the sample is above a critical point where the separation in domain is favourable.

As one length keeps increasing, the magnetostatic energy will tend to zero (when opposite charges are infinitely far apart), thus above L > 2.5 μm, the exchange energy dominates again, making the uniform state the ground state again. The diamond state is never a lower energy state in this simulation, as its 90^o Néel walls have a large width and the sample fixed length, 1 μm, they always appear as a local minimum and not as global states.

We have, then, chosen two aspect ratios to further investigate, 1:5, as was the

one previously used in this thesis, and 1:2, which is the aspect ratio of NIST 1 standard problem, that has been extensively studied in [41].

First, we have measured the total energy of a 2L x L x 5 nm permalloy rectangle as a function of L, where it ranges from 300 nm to 5 μm, see fig. 4.18. Three lower energy state regions can be identified. At small lengths, below 350 nm, the sample is a single domain (uniform). Above that, flux-closure domains become the more stable ones. The formation of the Landau domain structure lowers the magnetostatic energy of the system by dividing it in four domains with a 180^o Néel wall in its middle. It is replaced by the diamond state above 2.7 μm as this last presents 90^o Néel walls, that are lower in energy compared to 180^o ones, but they require a larger width in order to become stable [41].

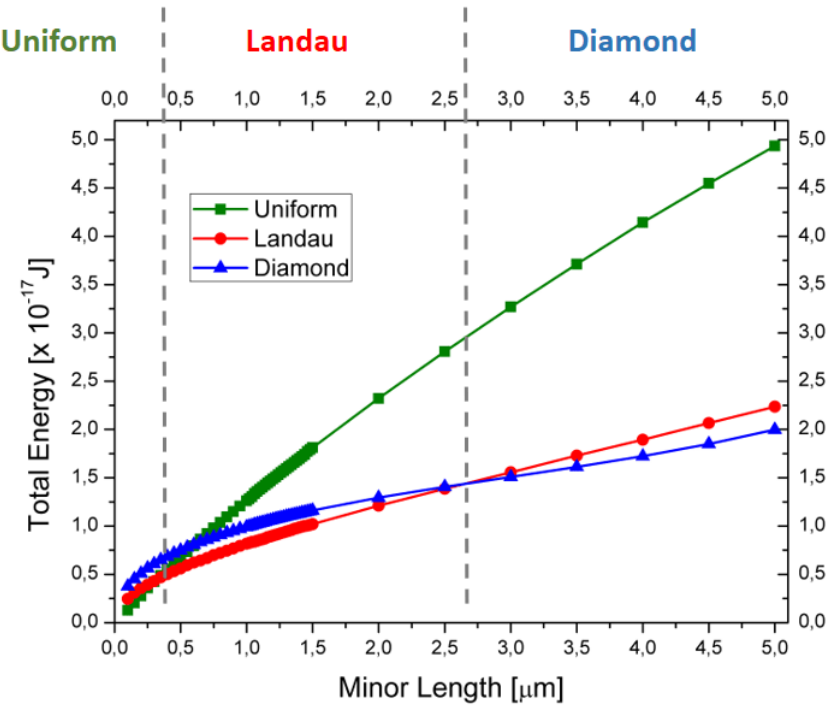

FIGURE 4.18: The total energy for a 2L μm x L μm x 5 nm permalloy rectangle as a function of L. The lower energy state is highlighted in each region.

The same energy measurement was performed for a 5L x L x 5 nm permalloy rectangle, fig. 4.19. This high aspect ratio makes the magnetostatic energy of the system to be much lower than it exchange interaction. Hence, the system does not divide into magnetic domains, and the uniform (C- or S- states) are always the lowest energy configurations.

For instance, although the 1 μm x 5 μm permalloy rectangle has been used as a Landau state in [32] and in our previous simulations, it is not the lower energy state in that geometry. Even though obtaining this configuration might be easy in a simulations, experimentally it would be very difficult and hardly reproducible, as this size always tend to become uniformly magnetized.

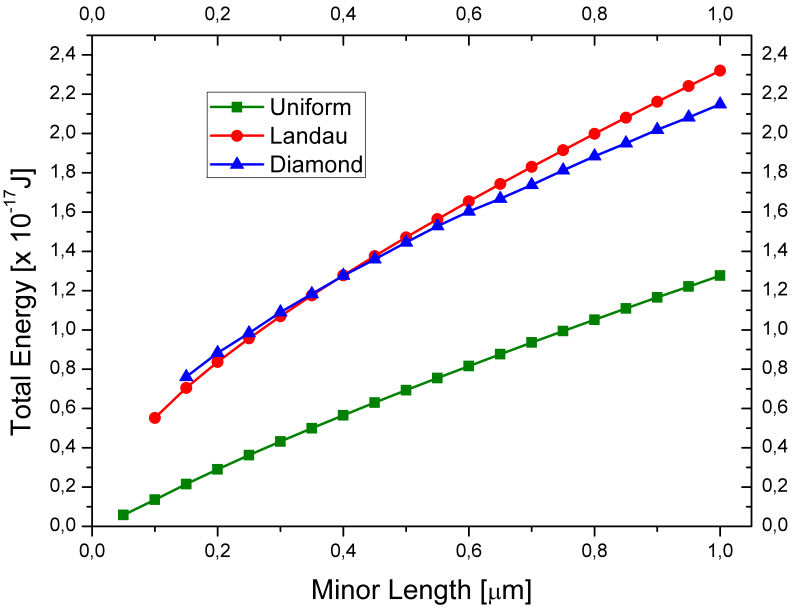

FIGURE 4.19: The total energy for a 5L μm x L μm x 5 nm permalloy rectangle as a function of L. The lower energy state is always the uniform.

Other aspect ratios and sizes, such as 1 μm x 2 μm, would be more reliable to obtain the Landau-domain structure. Nevertheless, experimentally, new challenges arise, such as roughness, the exact lateral shape and the exact surface shape. All of these jeopardize the realization of a reproducible Landau state, and an experimental approach is needed to overcome that, as will be discussed in the next section.

4.4 Fabricated Structures

This section aims to describe and show the samples used in this theses, fabricated by electron beam lithography.

The Néel wall naturally occurs in thin-film permalloy (or CoFeB) nanostructures that present a magnetic Landau flux-closure configuration. Although the Landau state is a minimum energy configuration in permalloy rectangles of certain sizes and aspect ratios, experimentally, obtaining that configuration can be very hard to achieve.

Edge roughness and edge inclination, which are present in any real nanostructure, give rise to an additional anisotropy of magnetostatic origin [53] that makes the desired magnetic state not reproducible, even in arrays of identical structures [54].

To overcome that issue, Wagner *et al.* (2016) [32] have proposed a modification to the structure in order to stabilize the Landau state: a 60 μm x 10 μm rectangle that gradually narrows to a constant 5 μm width on one side.

An array of those structures were fabricated by electron-beam lithography, with a 40 nm thickness of either permalloy or CoFeB, as shown in fig. 4.20.

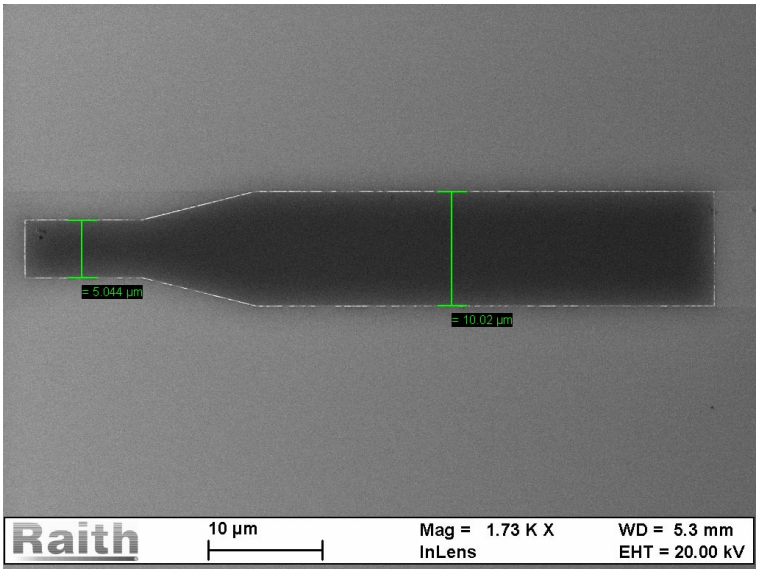

(A) Single element.

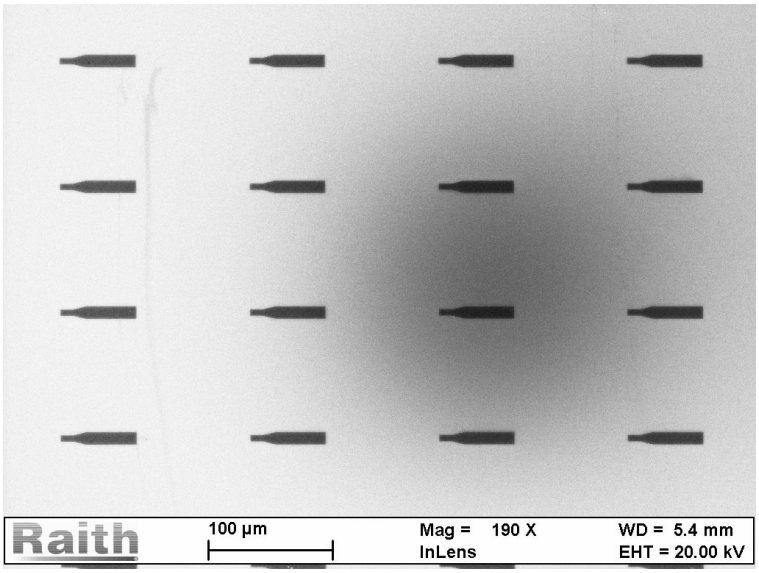

(B) Matrix of elements.

FIGURE 4.20: The nanostructures fabricated by electron-beam lithography in order to stabilize the Landau state: a rectangle with a 10 μm width that gradually narrows to a constant 5 μm width on one side.

Micromagnetic simulations have been performed in order to obtain the possible magnetic states for this structure. They are very similar to the ones obtained for a permalloy rectangle discussed in section 2.5, see fig. 4.21.

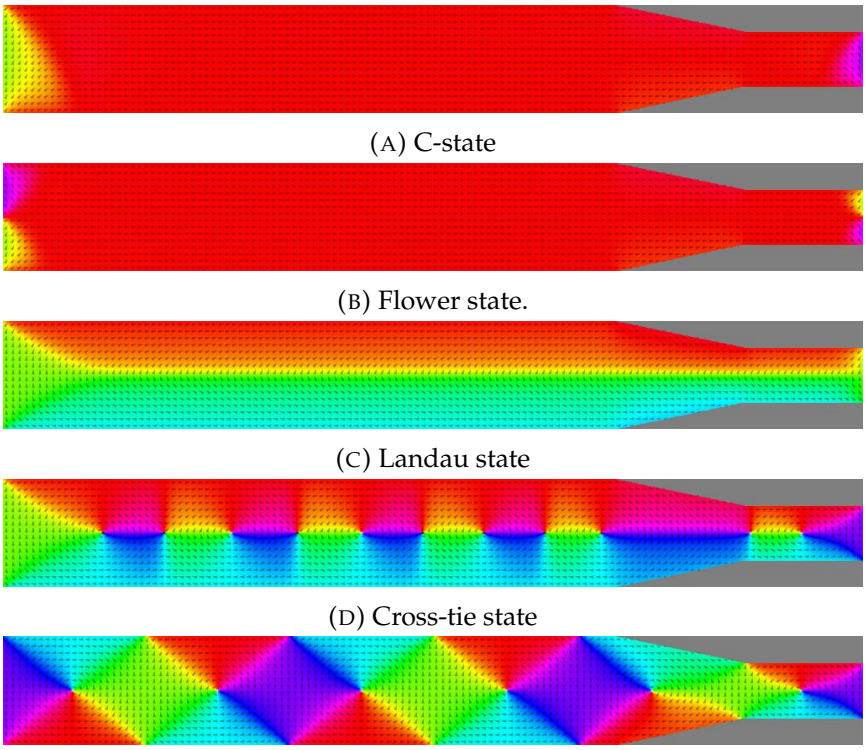

(A) C-state

(B) Flower state.

(C) Landau state

(D) Cross-tie state

(E) Diamond

FIGURE 4.21: Several possible magnetic configurations for the nanostructure.

4.5 Hysteresis Loop

This section intends to present the magnetometry measurements either for a matrix of elements, obtained by SQUID magnetometry, and for a single element, by MOKE magnetometry, and to compare the results with micromagnetic simulations.

4.5.1 Micromagnetic Simulations

We have first used the 5 μm x 1 μm x 5 nm permalloy rectangle to compare the hysteresis loop of the different magnetic configurations: Landau, uniform (either S- or C- state) and diamond. Basically, the chosen magnetic state was set and allowed to relax, after that an external magnetic field was applied and the system is again allowed to relax, and this new magnetic state is saved, as a function of the field.

The external field was applied in the x-direction in the range from -100 mT to 100 mT. The x-component of the magnetization from the zero-field until the first saturation is shown in fig. 4.22a for different initial magnetic states. The uniform state (either S- or C- state) has already a high x-magnetization at zero field and with an increasing external field, the area of the y-directed magnetic moments at its edges shrinks, causing a smooth increase in x-magnetization, until a transition to the flower-state takes place at high-fields (shown in fig. 4.22b).

In the vortex state, a field in the +x direction increases the domain magnetized in the +x direction and shrinks the -x domain. As a result, we see the vortex moving to the +y-direction, until it is abruptly expelled from the rectangle, which can be detected as a sudden jump in the hysteresis curve at 7 mT. After that the system becomes equal to the S- or C- state, and also suffers a transition to the flower state at a high field.

From the 4-vortexes diamond structure, the external field also increases the +x regions and shrinks the -x ones, as a consequence, half of the vortexes move in the +y direction and the other half to the -y direction. A very low field (less than .05 mT) is enough for the adjacent +y domains to merge, which can be seen as an abrupt change in magnetization in fig. 4.22a, and then the expulsion of the vortexes is seen at around 1 mT in the magnetization curve. After that, the system also behaves as a S- or C-state, having a transition to the flower state at a high field.

The transverse hysteresis curve, the external field applied in the y-direction, has similar features to the longitudinal one, although the shape anisotropy makes the field needed for achieving saturating higher. The zero external field till saturation curve can be seen in fig. 4.23a. Starting from a C-state, in which the edges are oppositely magnetized (+y and -y), one of the edges starts propagating towards the other edge with the increasing field, until it reaches the other end, and the -y edge is expelled, which is seen as a small jump in the curve at 7 mT.

In the flux-closure states, the increasing field makes the +y domains grow. In the Landau state it is seen through the movement of the vortex to the left, until it is completely removed from the structure at 8.5 mT. In the diamond state, adjacent +y domains grow, and the domains in the other directions shrink, which can be seen by the vortexes getting closer to each other in pairs. These are then anihilated at 9 mT, and the +y domain merge in a single domain.

All of the structures become a uniform structure, similar to a so-called transverse S- or C-state. If we the external field keeps rising, this state transitions to a transverse flower state. After this state is achieved, all the initial structures follow the same hysteresis curve, as can be seen in fig. 4.23b, with a high remanence and 13 mT coercive field.

Even though the different initial magnetization states have different behaviors, after the first saturation they all irreversibly become a uniform state, S- or C- state, and flower at high fields. From that point, all the magnetization curves match in a way that it is not possible to distinguish between their initial states anymore, as shown in fig. 4.22b. Hence, after the saturation of the sample, the flux-closure domains states are completely lost in that sample. If we want to return to a flux-closure state, a demagnetizing step might be needed.

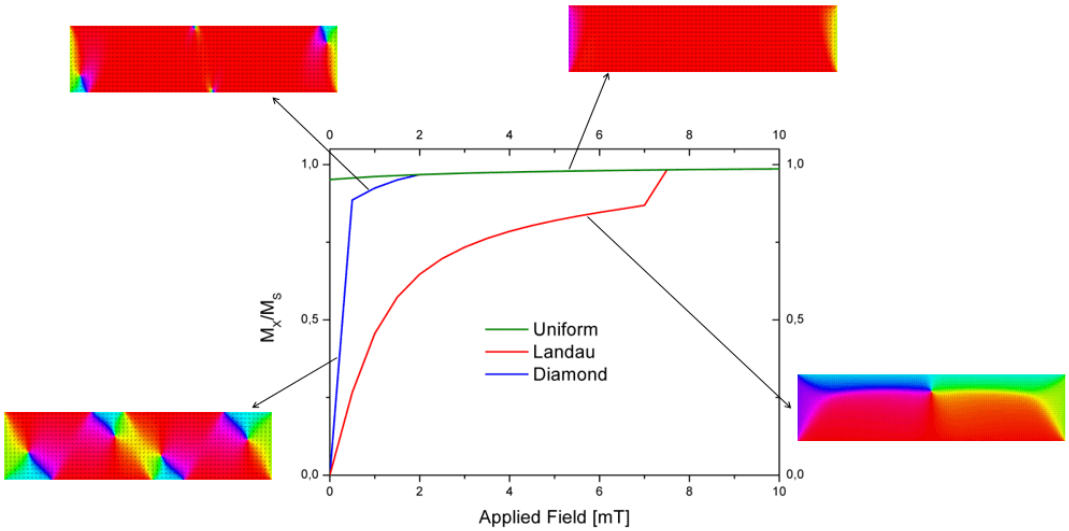

(A) Simulated x-direction hysteresis cycle for different magnetic configurations (uniform, Landau and diamond states from zero-field till saturation.

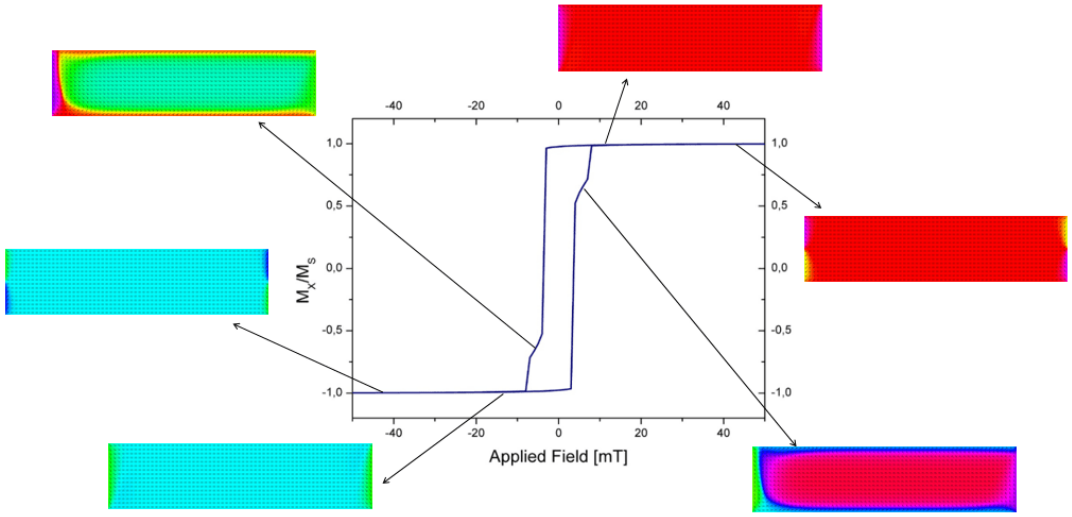

(B) Simulated x-direction hysteresis cycle from positive to negative saturation and back.

FIGURE 4.22: Longitudinal hysteresis cycle simulated for a 5 μm x 1μm x 5 nm permalloy rectangle. After the first saturating field is achieved, the information about the initial state (uniform, Landau or diamond) is completely lost.

4.5.2 Experimental Results

A matrix of elements as fig. 4.20, made of 40 nm thickness of permalloy, was measured by SQUID magnetometry in order to compare the hysteresis loop with the micromagnetic simulations.

The sample was first demagnetized through an alternate exponentially decaying magnetic field, and then the magnetization as a function of applied field was obtained. The result is shown in fig. 4.24.

The round curve obtained by SQUID magnetometry is due to the magnetostatic interaction between different elements in the matrix. This makes the transition from

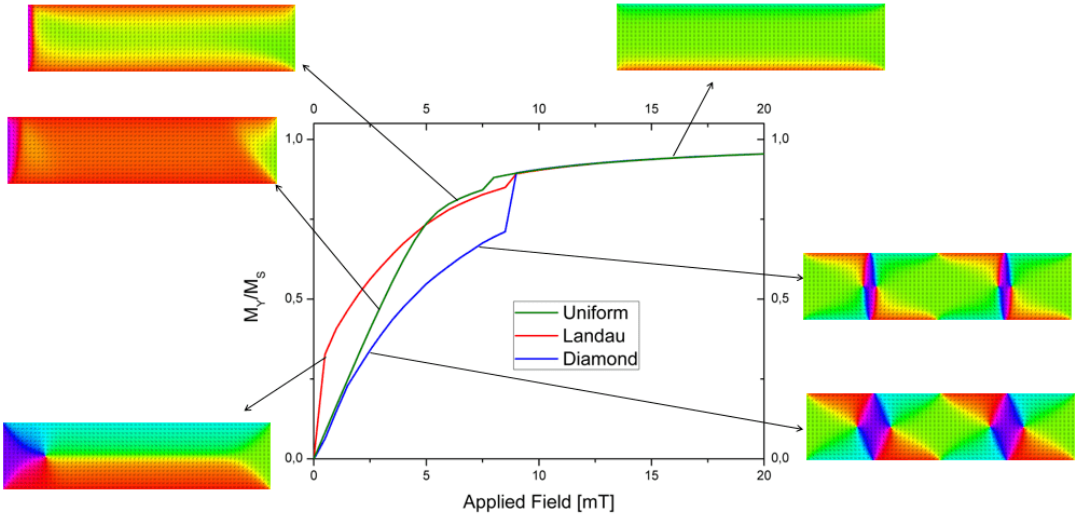

(A) Simulated y-direction hysteresis cycle for different magnetic configurations (uniform, Landau and diamond states from zero-field till saturation.

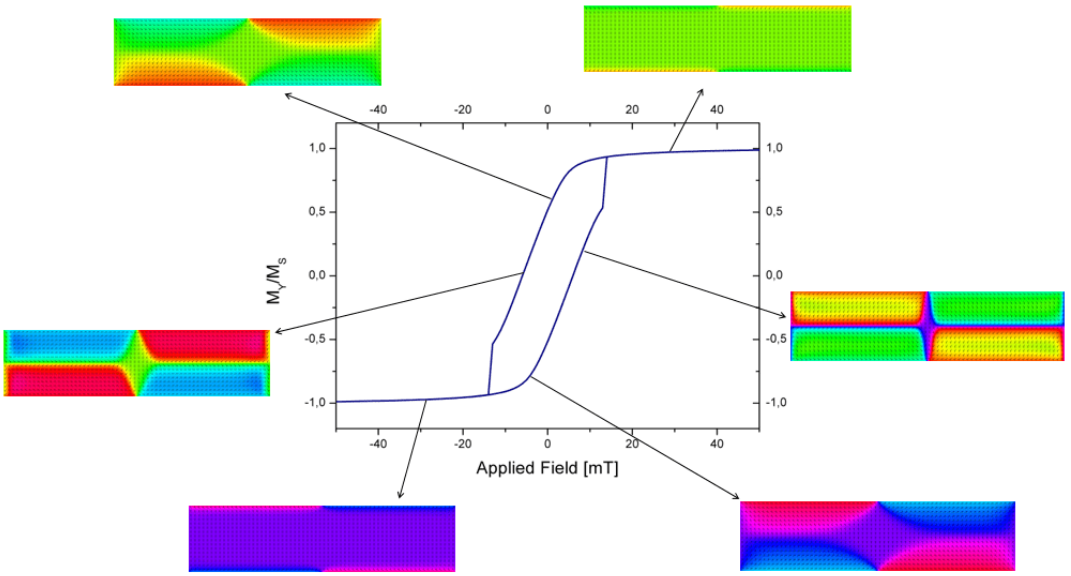

(B) Simulated y-direction hysteresis cycle from positive to negative saturation and back.

FIGURE 4.23: Transverse hysteresis cycle simulated for a 5 μm x 1μm x 5 nm permalloy rectangle.

the saturated state in one direction to the opposite direction not an abrupt movement, but rather a continuous and smooth one, and only one jump is seen from one saturation to the other.

In the inset of fig. 4.24, it is possible to see that the initial configuration, the state after demagnetization, undergoes an abrupt change in magnetization with only a small field applied. As the micromagnetic simulations suggest, this demagnetized state, which can be a Landau-state or a diamond state for example, is irreversibly lost after the application of small magnetic fields.

In order to characterize each element individually, and not the matrix as a whole,

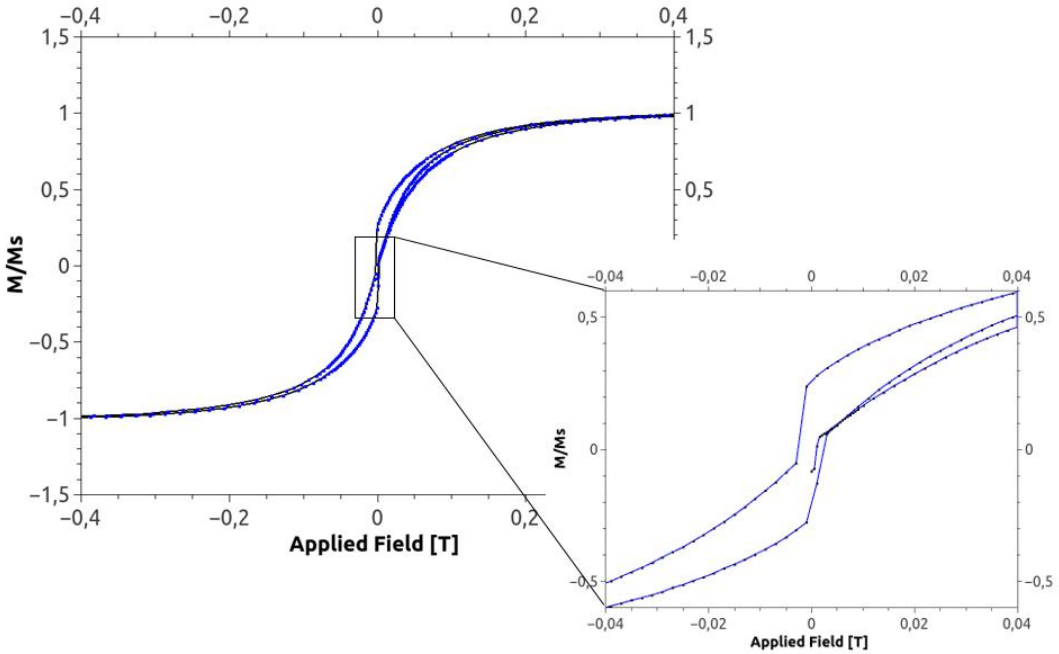

FIGURE 4.24: The hysteresis loop of a matrix of the permalloy elements, measured by SQUID magnetometry.

MOKE magnetometry was applied, with a laser beam that was focused on only one permalloy nanostructure. the result is shown in fig. 4.25.

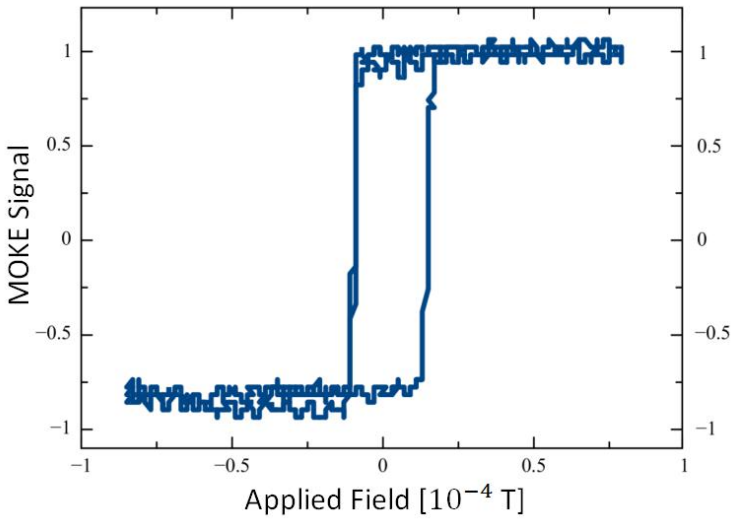

FIGURE 4.25: The hysteresis loop of one single permalloy element, measured by Magneto-optic Kerr effect (MOKE) magnetometry.

This result, with only two sudden jumps in magnetization, suggest that the element presents a bi-stable magnetic configuration. As in the MOKE magnetometry there is no demagnetizing step, any flux-closure state was lost, so the obtained hysteresis curve is very similar to the micromagnetic simulations of a uniform state,

alternating between opposite directions of saturation.

The magnetometry results suggest that the zero-net magnetization configuration, as the desired Landau-state, need a demagnetization step in order to be obtained. Also, the application of an external magnetic field might irreversibly transform it in an uniform S-state or C-state.

4.6 Magnetic Domains Imaging: MFM and Kerr Microscopy

The magnetic domain configuration in the nanostructures is a crucial step in this work, in order to identify it two microscopy techniques were applied: magnetic force microscopy (MFM) and Magneto-Optic Kerr Effect (MOKE) microscopy.

Initially, MFM images were obtained of a matrix of 40 nm thick permalloy elements, as fabricated, in the lift mode two-pass technique at a 35 nm height. The result can be seen in fig. 4.26a. The magnetic contrast can be seen at the edges. At the right end of the structure, a very remarkable line contrast, but no contrast is seen in the middle of the sample, which is what would be expected from a S- or C- state magnetic configuration.

In order to confirm this, micromagnetic simulations of a smaller version of the nanostructure, with a larger width of 1 μm and a smaller one of 0.5 μm, was obtained by setting an initial uniform state and allowing the system to relax, fig. 4.26b(top). A simulated MFM image of the relaxed structure was obtained in MuMax3 for comparison, as fig. 4.26b(bottom). The contrasts are very similar, with only lateral features, with a uniform magnetization in the center of the sample. Only the uniform states were observed in our samples.

We wanted to investigate the effect of applying external fields in the magnetic configuration of our samples. But due to time and equipment limitations, we struggled to accomplish the adequate set-up for that in the MFM. That was overcome through the use of MOKE microscopy. However, as permalloy presents a low contrast in MOKE images, the same structures were fabricated in a 40 nm thick CoFeB, which has a more adequate contrast for Kerr imaging.

First, we apply a longitudinal field until reaching saturation, and all posterior images are subtracted from the saturated one in order to enhance the contrast. Fig. 4.27 shows the sequence obtained for an increasing external field applied in the longitudinal direction of the structure. In fig. 4.27a we see an initial twist of magnetization at one end, and as the field increases, it propagates towards the field direction (fig. 4.27b), moreover, from that, an abrupt inversion of the magnetization occurs (fig. 4.27c).

By applying a transverse magnetic field, the magnetization readily inverts from one direction to the other. The transition is abrupt and the images have to be quickly

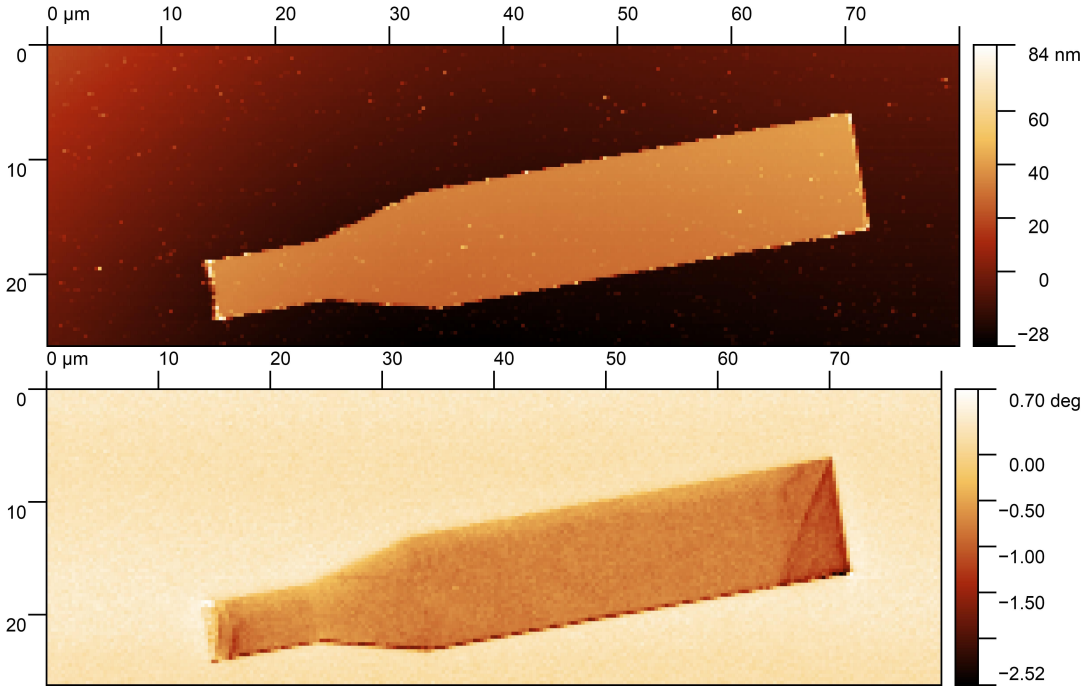

(A) Topographic (top) and magnetic phase (bottom) MFM images of permalloy nanostructure with no application of an external field.

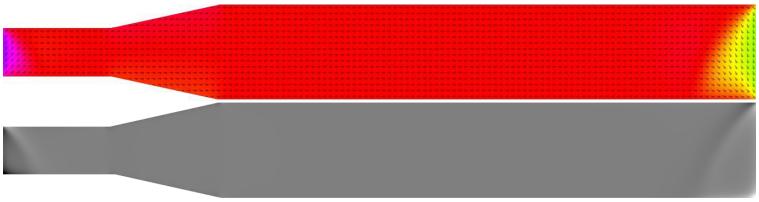

(B) Micromagnetic simulation of the permalloy nanostructure in the uniform state (top) and its MFM image simulation at a 40 nm height (bottom).

FIGURE 4.26: Magnetic force microscopy of elements

taken. the intermediary configurations between the saturated states exhibit complex magnetic patterns, fig. 4.28. However, a longitudinal linear structure seemed to propagate under the inversion. This structure is similar to what would be expected from a Néel wall with cross-ties (fig. 4.21d).

Finally, as we wanted to approach the Landau flux-closure state, from the hysteresis measurements, we found that a demagnetizing external field would be necessary. An alternate decaying magnetic field was then applied transverse to the structures. The sample magnetization was then analyzed for a longitudinal MOKE contrast. Due to the demagnetizing process, it is not possible to subtract the images from the saturated sample, so the contrast was enhanced by subtracting images of slightly different polarization angles: the analyzer was rotated by $\pm 3^o$ in relation to the polarizers.

For a transverse demagnetization and a longitudinal MOKE analysis, the obtained images can be seen in fig. 4.29a. This magnetic configuration is very similar to the 4-domain flux-closure Landau state, with a Néel wall at its center and without

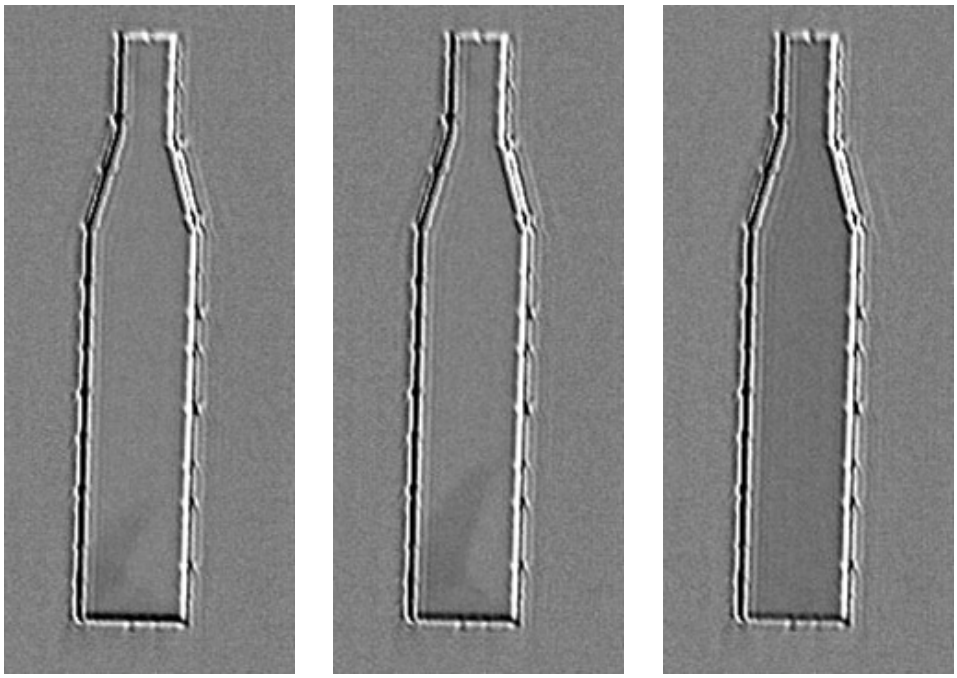

(A) (B) (C)

FIGURE 4.27: Kerr image of one CoFeB element with an increasing longitudinal external magnetic field in the sequence (A) to (C).

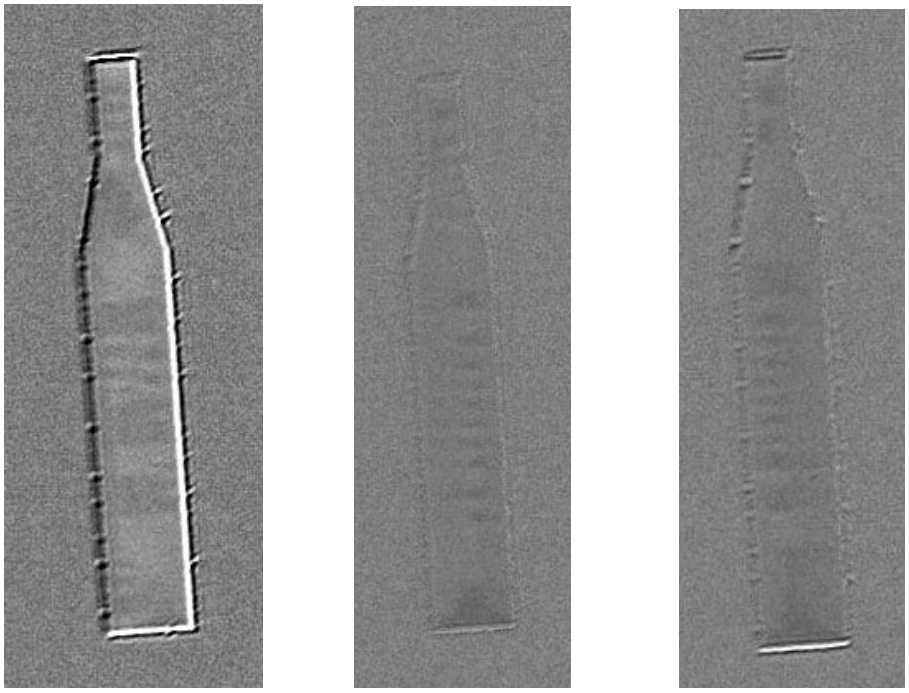

FIGURE 4.28: Kerr image of CoFeB element under a transverse external field.

the cross-ties, as compared to the simulation in fig. 4.29b.

We have then confirmed the protocol in order to obtain the desired Néel wall experimentally. Although an external magnetic field is able to completely destroy the Landau domain state, a transverse demagnetizing field can reproducibly turn

this structure back to the flux-closure state, which is a basic precondition for the realization of ferromagnetic resonance experiments.

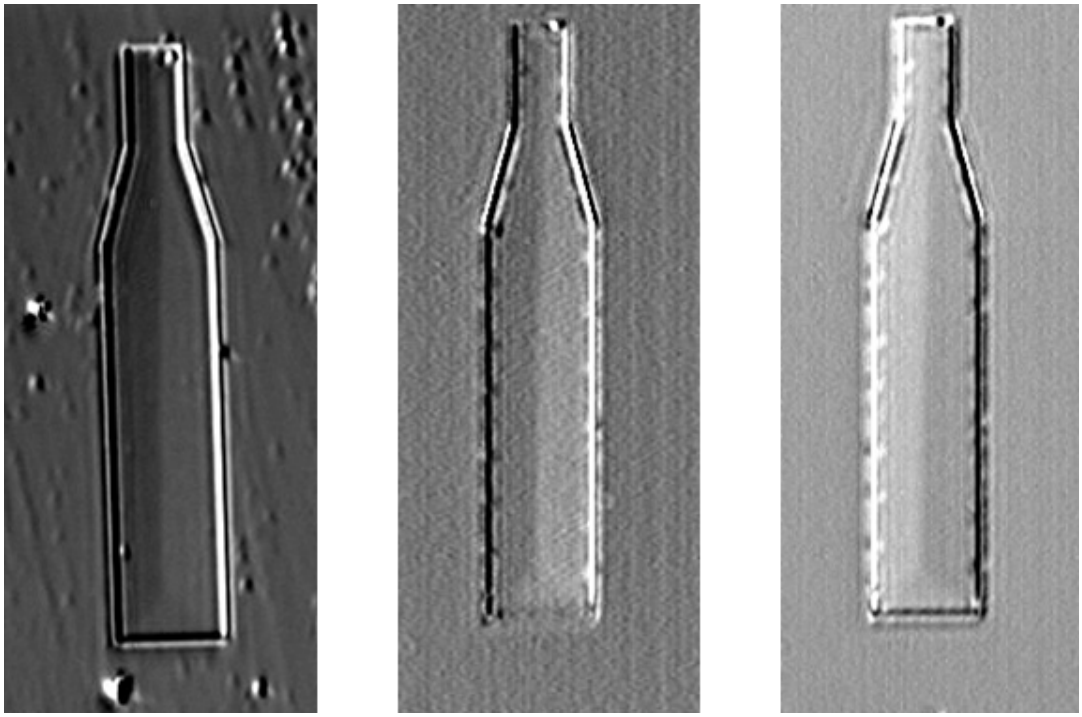

(A) Several structures after a transversal demagnetization process with longitudinal MOKE sensibility.

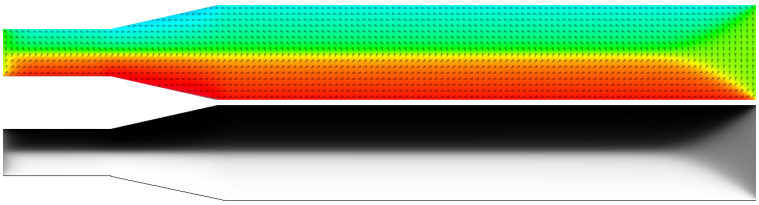

(B) Micromagnetic simulation of the nanostructure with a Néel wall in its center (top), and the longitudinal component of the magnetization in the same structure (bottom).

FIGURE 4.29: MOKE images after demagnetization.

Chapter 5

Conclusions and Future Work

In summary, we have analyzed the suitability of a magnetic Néel wall as a spin-wave nano-sized waveguide for magnonic applications. From an infinite Néel wall, obtained in micromagnetic simulations through periodic boundary conditions, we have shown that the opposite uniform domains generate a strong demagnetizing field inside the wall, which confines the spin-wave within its width, until a frequency around 3 GHz. Above that value, the waves start to spread to the domains and the confinement effect is lost.

Well-defined wave vectors were found for this propagation, with a magnetostatic-dominated dispersion relation with positive dispersion and group velocities up to 1.8 km/s. The attenuation constant, measured by the propagation length can be up to 4 μm due to the narrow alley in which the waves propagate, which avoid scattering at the edges of the sample. Nonetheless, a complete analytical description of the dispersion could not be obtained, and a more complex physical model, which includes the confinement due to the dipolar potential well, is needed.

All of this is tuned with the usual building blocks conditions for a magnonic device design, and without the need of an external magnetic field, making this a very energy-efficient system. Another advantage of the walls is their intrinsic flexibility in response to spin current or magnetic fields. Very low fields are needed for the wall movement along the sample.

The Néel wall are naturally found in Landau-domain states in permalloy nanostructures. The Landau state possesses four uniform domains, and the Néel wall is separated in two oppositely magnetized parts by a magnetic vortex. We have shown that, propagating a spin-wave in one of the sides to the other, the vortex will act as a blockage for the waves, only allowing very specific frequencies to pass. It, therefore, acts as a frequency filter for spin-waves. Also, the dispersion relation is not changed by the sample geometry, which allows a manifold of circuit designs.

One main issue for obtaining a Landau structure experimentally is to find an ideal geometry and size for it to be a magnetic ground state in the permalloy rectangle. As showed, for very small structures, and for rectangles with a high aspect

ratio, the magnetostatic energy becomes much lower than the exchange interaction, and the uniform states tend to become the most stable ones. In order to obtain a Landau state as a ground state, a suitable aspect ratio and a length sized have to be simulated, as for example a 1 μm x 2 μm rectangle.

Experimentally, we have fabricated a structure, through electron-beam lithography and lift-off, that is a 60 μm x 10 μm permalloy rectangle, that at one side the width gradually shrinks to a constant 5 μm value. According to the literature [32], this structure is more stable for a Landau state than the rectangle itself, which we verified experimentally.

Magnetization curves were simulated, and they have shown that flux-closure domain states are completely destroyed after they become saturated. This indicated that in order to obtain a Landau or a diamond state, a demagnetizing step would be needed for reliability. The measured magnetization curves agree with the simulation, as they present a uniform-state like curve. Only after an alternate exponentially decaying magnetic field, a near-zero net magnetization state is obtained.

Through MFM and Kerr microscopy, we could visually confirm the uniform state obtained at the remanence. And we have seen that in order to reproducibly obtain a Landau state, with a Néel wall in its center and without cross-ties, a demagnetizing field has to be applied transversely to the structures. Despite obtaining a protocol for the experimental acquisition of a Néel wall, we have not yet perform dynamic magnetic experiments.

As next steps, micromagnetic simulations of magnonic logic gates that make use of the walls shall be designed, and, experimentally, waveguides are being fabricated for ferromagnetic resonance experiments. We intend to perform time-resolved Kerr microscopy and micro-focused Brillouin light scattering experiments, to determine the wavelength, propagation length and several other experimental parameters, in order to make this feasible for applications in flexible and energy-efficient magnonic devices.

Bibliography

[1] Semiconductor Industry Association. *Annual Semiconductor Sales Increase 21.6 Percent, Top $ 400 Billion for First Time*. 2019. URL: https://www.semiconductors.org/news/2018/02/05/global_sales_report_2017/annual_semiconductor_sales_increase_21.6_percent_top_400_billion_for_first_time/ (visited on 03/12/2018).

[2] M. Mitchell Waldrop. "More than Moore". In: *Nature* 530 (2016), pp. 144–147. URL: https://www.nature.com/news/the-chips-are-down-for-moore-s-law-1.19338.

[3] Jin Lan, Weichao Yu, Ruqian Wu, and Jiang Xiao. "Spin-Wave Diode". In: *Physical Review X* 5.4 (Dec. 2015). DOI: 10.1103/physrevx.5.041049. URL: https://doi.org/10.1103/physrevx.5.041049.

[4] David Thomson, Aaron Zilkie, John E Bowers, Tin Komljenovic, Graham T Reed, Laurent Vivien, Delphine Marris-Morini, Eric Cassan, Léopold Virot, Jean-Marc Fédéli, Jean-Michel Hartmann, Jens H Schmid, Dan-Xia Xu, Frédéric Boeuf, Peter O'Brien, Goran Z Mashanovich, and M Nedeljkovic. "Roadmap on silicon photonics". In: *Journal of Optics* 18.7 (June 2016), p. 073003. DOI: 10.1088/2040-8978/18/7/073003. URL: https://doi.org/10.1088/2040-8978/18/7/073003.

[5] Fabio Pulizzi. "Spintronics". In: *Nature Materials* 11.5 (May 2012), pp. 367–367. DOI: 10.1038/nmat3327. URL: https://doi.org/10.1038/nmat3327.

[6] V V Kruglyak, S O Demokritov, and D Grundler. "Magnonics". In: *Journal of Physics D: Applied Physics* 43.26 (June 2010), p. 264001. DOI: 10.1088/0022-3727/43/26/264001. URL: https://doi.org/10.1088/0022-3727/43/26/264001.

[7] F. Bloch. "Zur Theorie des Ferromagnetismus". In: *Zeitschrift für Physik* 61.3 (Mar. 1930), pp. 206–219. ISSN: 0044-3328. DOI: 10.1007/BF01339661. URL: https://doi.org/10.1007/BF01339661.

[8] Dirk Grundler. "Reconfigurable magnonics heats up". In: *Nature Physics* 11.6 (June 2015), pp. 438–441. DOI: 10.1038/nphys3349. URL: https://doi.org/10.1038/nphys3349.

[9] A. V. Chumak, V. I. Vasyuchka, A. A. Serga, and B. Hillebrands. "Magnon spintronics". In: *Nature Physics* 11.6 (June 2015), pp. 453–461. DOI: 10.1038/nphys3347. URL: https://doi.org/10.1038/nphys3347.

[10] T. Schneider, A. A. Serga, T. Neumann, B. Hillebrands, and M. P. Kostylev. "Phase reciprocity of spin-wave excitation by a microstrip antenna". In: *Physical Review B* 77.21 (June 2008). DOI: 10.1103/physrevb.77.214411. URL: https://doi.org/10.1103/physrevb.77.214411.

[11] Daniel R. Birt, Kyongmo An, Maxim Tsoi, Shingo Tamaru, David Ricketts, Kin L. Wong, Pedram Khalili Amiri, Kang L. Wang, and Xiaoqin Li. "Deviation from exponential decay for spin waves excited with a coplanar waveguide antenna". In: *Applied Physics Letters* 101.25 (Dec. 2012), p. 252409. DOI: 10.1063/1.4772798. URL: https://doi.org/10.1063/1.4772798.

[12] Tobias Stückler, Chuanpu Liu, Haiming Yu, Florian Heimbach, Jilei Chen, Junfeng Hu, Sa Tu, Md.Shah Alam, Jianyu Zhang, Youguang Zhang, Ian L. Farrell, Chrissy Emeny, Simon Granville, Zhi-Min Liao, Dapeng Yu, and Weisheng Zhao. "Spin wave propagation detected over 100m in half-metallic Heusler alloy Co 2 MnSi". In: *Journal of Magnetism and Magnetic Materials* 450 (Mar. 2018), pp. 13–17. DOI: 10.1016/j.jmmm.2017.09.074. URL: https://doi.org/10.1016/j.jmmm.2017.09.074.

[13] S. Mansfeld, J. Topp, K. Martens, J. N. Toedt, W. Hansen, D. Heitmann, and S. Mendach. "Spin Wave Diffraction and Perfect Imaging of a Grating". In: *Physical Review Letters* 108.4 (Jan. 2012). DOI: 10.1103/physrevlett.108.047204. URL: https://doi.org/10.1103/physrevlett.108.047204.

[14] Ferran Macià, Andrew D Kent, and Frank C Hoppensteadt. "Spin-wave interference patterns created by spin-torque nano-oscillators for memory and computation". In: *Nanotechnology* 22.9 (Jan. 2011), p. 095301. DOI: 10.1088/0957-4484/22/9/095301. URL: https://doi.org/10.1088/0957-4484/22/9/095301.

[15] J. Stigloher, M. Decker, H. S. Körner, K. Tanabe, T. Moriyama, T. Taniguchi, H. Hata, M. Madami, G. Gubbiotti, K. Kobayashi, T. Ono, and C. H. Back. "Snell's Law for Spin Waves". In: *Physical Review Letters* 117.3 (July 2016). DOI: 10.1103/physrevlett.117.037204. URL: https://doi.org/10.1103/physrevlett.117.037204.

[16] S.O. Demokritov. *Spin Wave Confinement*. Pan Stanford, 2009. ISBN: 9789814241069. URL: https://books.google.com.br/books?id=T%5C_I36K0%5C_9c8C.

[17] Jin Lan, Weichao Yu, Ruqian Wu, and Jiang Xiao. "Spin-Wave Diode". In: *Physical Review X* 5.4 (Dec. 2015). DOI: 10.1103/physrevx.5.041049. URL: https://doi.org/10.1103/physrevx.5.041049.

[18] K. Vogt, F.Y. Fradin, J.E. Pearson, T. Sebastian, S.D. Bader, B. Hillebrands, A. Hoffmann, and H. Schultheiss. "Realization of a spin-wave multiplexer". In: *Nature Communications* 5 (Apr. 2014). DOI: 10.1038/ncomms4727. URL: https://doi.org/10.1038/ncomms4727.

[19] T. Schneider, A. A. Serga, B. Leven, B. Hillebrands, R. L. Stamps, and M. P. Kostylev. "Realization of spin-wave logic gates". In: *Applied Physics Letters* 92.2

(Jan. 2008), p. 022505. DOI: 10.1063/1.2834714. URL: https://doi.org/10.1063/1.2834714.

[20] V. S. Tkachenko, A. N. Kuchko, M. Dvornik, and V. V. Kruglyak. "Propagation and scattering of spin waves in curved magnonic waveguides". In: *Applied Physics Letters* 101.15 (Oct. 2012), p. 152402. DOI: 10.1063/1.4757994. URL: https://doi.org/10.1063/1.4757994.

[21] Bivas Rana and YoshiChika Otani. "Voltage-Controlled Reconfigurable Spin-Wave Nanochannels and Logic Devices". In: *Physical Review Applied* 9.1 (Jan. 2018). DOI: 10.1103/physrevapplied.9.014033. URL: https://doi.org/10.1103/physrevapplied.9.014033.

[22] K. Vogt, H. Schultheiss, S. Jain, J. E. Pearson, A. Hoffmann, S. D. Bader, and B. Hillebrands. "Spin waves turning a corner". In: *Applied Physics Letters* 101.4 (July 2012), p. 042410. DOI: 10.1063/1.4738887. URL: https://doi.org/10.1063/1.4738887.

[23] T. Brächer, P. Pirro, J. Westermann, T. Sebastian, B. Lägel, B. Van de Wiele, A. Vansteenkiste, and B. Hillebrands. "Generation of propagating backward volume spin waves by phase-sensitive mode conversion in two-dimensional microstructures". In: *Applied Physics Letters* 102.13 (Apr. 2013), p. 132411. DOI: 10.1063/1.4800005. URL: https://doi.org/10.1063/1.4800005.

[24] Vladislav E. Demidov, Sergej O. Demokritov, Karsten Rott, Patryk Krzysteczko, and Guenter Reiss. "Mode interference and periodic self-focusing of spin waves in permalloy microstripes". In: *Physical Review B* 77.6 (Feb. 2008). DOI: 10.1103/physrevb.77.064406. URL: https://doi.org/10.1103/physrevb.77.064406.

[25] T. Sebastian, Y. Ohdaira, T. Kubota, P. Pirro, T. Brächer, K. Vogt, A. A. Serga, H. Naganuma, M. Oogane, Y. Ando, and B. Hillebrands. "Low-damping spin-wave propagation in a micro-structured Co2Mn0.6Fe0.4Si Heusler waveguide". In: *Applied Physics Letters* 100.11 (Mar. 2012), p. 112402. DOI: 10.1063/1.3693391. URL: https://doi.org/10.1063/1.3693391.

[26] S. Urazhdin, V. E. Demidov, H. Ulrichs, T. Kendziorczyk, T. Kuhn, J. Leuthold, G. Wilde, and S. O. Demokritov. "Nanomagnonic devices based on the spin-transfer torque". In: *Nature Nanotechnology* 9.7 (May 2014), pp. 509–513. DOI: 10.1038/nnano.2014.88. URL: https://doi.org/10.1038/nnano.2014.88.

[27] Xiangjun Xing, Yongli Yu, Shuwei Li, and Xiaohong Huang. "How do spin waves pass through a bend?" In: *Scientific Reports* 3.1 (Oct. 2013). DOI: 10.1038/srep02958. URL: https://doi.org/10.1038/srep02958.

[28] G. Venkat, D. Venkateswarlu, R. S. Joshi, M. Franchin, H. Fangohr, P. S. Anil Kumar, and A. Prabhakar. "Enhanced spin wave propagation in magnonic rings by bias field modulation". In: *AIP Advances* 8.5 (May 2018), p. 056006. DOI: 10.1063/1.5006576. URL: https://doi.org/10.1063/1.5006576.

[29] Arabinda Haldar, Dheeraj Kumar, and Adekunle Olusola Adeyeye. "A reconfigurable waveguide for energy-efficient transmission and local manipulation

of information in a nanomagnetic device". In: *Nature Nanotechnology* 11.5 (Feb. 2016), pp. 437–443. DOI: 10.1038/nnano.2015.332. URL: https://doi.org/10.1038/nnano.2015.332.

[30] Felipe Garcia-Sanchez, Pablo Borys, Rémy Soucaille, Jean-Paul Adam, Robert L. Stamps, and Joo-Von Kim. "Narrow Magnonic Waveguides Based on Domain Walls". In: *Physical Review Letters* 114.24 (June 2015). DOI: 10.1103/physrevlett.114.247206. URL: https://doi.org/10.1103/physrevlett.114.247206.

[31] Antonio Lara, Javier Robledo Moreno, Konstantin Y. Guslienko, and Farkhad G. Aliev. "Information processing in patterned magnetic nanostructures with edge spin waves". In: *Scientific Reports* 7.1 (July 2017). DOI: 10.1038/s41598-017-05737-8. URL: https://doi.org/10.1038/s41598-017-05737-8.

[32] K. Wagner, A. Kákay, K. Schultheiss, A. Henschke, T. Sebastian, and H. Schultheiss. "Magnetic domain walls as reconfigurable spin-wave nanochannels". In: *Nature Nanotechnology* 11.5 (Feb. 2016), pp. 432–436. DOI: 10.1038/nnano.2015.339. URL: https://doi.org/10.1038/nnano.2015.339.

[33] Lukas Korber, Kai Wagner, Attila Kakay, and Helmut Schultheiss. "Spin-Wave Reciprocity in the Presence of Néel Walls". In: *IEEE Magnetics Letters* 8 (2017), pp. 1–4. DOI: 10.1109/lmag.2017.2762642. URL: https://doi.org/10.1109/lmag.2017.2762642.

[34] Liang-Juan Chang, Yen-Fu Liu, Ming-Yi Kao, Li-Zai Tsai, Jun-Zhi Liang, and Shang-Fan Lee. "Ferromagnetic domain walls as spin wave filters and the interplay between domain walls and spin waves". In: *Scientific Reports* 8.1 (Mar. 2018). DOI: 10.1038/s41598-018-22272-2. URL: https://doi.org/10.1038/s41598-018-22272-2.

[35] Arne Vansteenkiste, Jonathan Leliaert, Mykola Dvornik, Mathias Helsen, Felipe Garcia-Sanchez, and Bartel Van Waeyenberge. "The design and verification of MuMax3". In: *AIP Advances* 4.10 (2014), p. 107133. DOI: 10.1063/1.4899186.

[36] C. Kittel. *Introduction to Solid State Physics*. Wiley, 2004. ISBN: 9780471415268. URL: https://books.google.com.br/books?id=kym4QgAACAAJ.

[37] A.P. Guimarães. *Principles of Nanomagnetism*. NanoScience and Technology. Springer Berlin Heidelberg, 2009. ISBN: 9783642014826. URL: https://books.google.com.br/books?id=qhUpYKK5DcEC.

[38] B.D. Cullity and C.D. Graham. *Introduction to Magnetic Materials*. Wiley, 2011. ISBN: 9781118211496. URL: https://books.google.com.br/books?id=fh%5C_F0G9KuSgC.

[39] R.C. O'Handley. *Modern Magnetic Materials: Principles and Applications*. Wiley, 1999. ISBN: 9780471155669. URL: https://books.google.com.br/books?id=RKV1QgAACAAJ.

[40] A. Hubert and R. Schäfer. *Magnetic Domains: The Analysis of Magnetic Microstructures*. Springer, 1998. ISBN: 9783540641087. URL: https://books.google.com.br/books?id=pBE42lLYs-MC.

[41] W. Rave and A. Hubert. "Magnetic ground state of a thin-film element". In: *IEEE Transactions on Magnetics* 36.6 (2000), pp. 3886–3899. DOI: 10.1109/20.914337. URL: https://doi.org/10.1109/20.914337.

[42] D.D. Stancil and A. Prabhakar. *Spin Waves: Theory and Applications*. Springer US, 2009. ISBN: 9780387778655. URL: https://books.google.com.br/books?id=ehN6-ubvKwoC.

[43] Charles Kittel. "On the Theory of Ferromagnetic Resonance Absorption". In: *Physical Review* 73.2 (Jan. 1948), pp. 155–161. DOI: 10.1103/physrev.73.155. URL: https://doi.org/10.1103/physrev.73.155.

[44] R. W. Damon and J. R. Eshbach. "Magnetostatic Modes of a Ferromagnetic Slab". In: *Journal of Applied Physics* 31.5 (1960), S104–S105. DOI: 10.1063/1.1984622. URL: https://doi.org/10.1063/1.1984622.

[45] B A Kalinikos and A N Slavin. "Theory of dipole-exchange spin wave spectrum for ferromagnetic films with mixed exchange boundary conditions". In: *Journal of Physics C: Solid State Physics* 19.35 (1986), p. 7013. URL: http://stacks.iop.org/0022-3719/19/i=35/a=014.

[46] C. Eyrich, W. Huttema, M. Arora, E. Montoya, F. Rashidi, C. Burrowes, B. Kardasz, E. Girt, B. Heinrich, O. N. Mryasov, M. From, and O. Karis. "Exchange stiffness in thin film Co alloys". In: *Journal of Applied Physics* 111.7 (Apr. 2012), p. 07C919. DOI: 10.1063/1.3679433. URL: https://doi.org/10.1063/1.3679433.

[47] K. Kobayashi, N. Inaba, N. Fujita, Y. Sudo, T. Tanaka, M. Ohtake, M. Futamoto, and F. Kirino. "Damping Constants for Permalloy Single-Crystal Thin Films". In: *IEEE Transactions on Magnetics* 45.6 (June 2009), pp. 2541–2544. DOI: 10.1109/tmag.2009.2018862. URL: https://doi.org/10.1109/tmag.2009.2018862.

[48] Jeovani Brandão. "Dinâmica de paredes de domínio com vórtice em linhas de Permalloy com defeitos triangulares". PhD thesis. Centro Brasileiro de Pesquisas Físicas, Nov. 2014.

[49] *Magnetic Property Measurement System, SQUID VSM User's Manual*. 13th ed. Quantum Design. 6325 Lusk Boulevard San Diego, CA 92121 USA, Apr. 2010.

[50] P. Weinberger. "John Kerr and his effects found in 1877 and 1878". In: *Philosophical Magazine Letters* 88.12 (Dec. 2008), pp. 897–907. DOI: 10.1080/09500830802526604. URL: https://doi.org/10.1080/09500830802526604.

[51] Z. Q. Qiu and S. D. Bader. "Surface magneto-optic Kerr effect". In: *Review of Scientific Instruments* 71.3 (Mar. 2000), pp. 1243–1255. DOI: 10.1063/1.1150496. URL: https://doi.org/10.1063/1.1150496.

[52] Ki-Suk Lee and Sang-Koog Kim. "Conceptual design of spin wave logic gates based on a Mach–Zehnder-type spin wave interferometer for universal logic

functions". In: *Journal of Applied Physics* 104.5 (Sept. 2008), p. 053909. DOI: 10.1063/1.2975235. URL: https://doi.org/10.1063/1.2975235.

[53] R. P. Cowburn, D. K. Koltsov, A. O. Adeyeye, and M. E. Welland. "Lateral interface anisotropy in nanomagnets". In: *Journal of Applied Physics* 87.9 (2000), pp. 7067–7069. DOI: 10.1063/1.372933. eprint: https://doi.org/10.1063/1.372933. URL: https://doi.org/10.1063/1.372933.

[54] S. Hankemeier, R. Frömter, N. Mikuszeit, D. Stickler, H. Stillrich, S. Pütter, E. Y. Vedmedenko, and H. P. Oepen. "Magnetic Ground State of Single and Coupled Permalloy Rectangles". In: *Phys. Rev. Lett.* 103 (14 Oct. 2009), p. 147204. DOI: 10.1103/PhysRevLett.103.147204. URL: https://link.aps.org/doi/10.1103/PhysRevLett.103.147204.